Process Parameter Optimization for Crack Mitigation in CM247LC processed by Electron Beam Powder Bed Fusion

by

Sebastian Soo

A thesis

presented to the University of Waterloo

in fulfilment of the

thesis requirement for the degree of

Master of Applied Science

in

Mechanical & Mechatronics Engineering

Waterloo, Ontario, Canada, 2025

© Sebastian Soo 2025

Author's Declaration

I hereby declare that I am the sole author of this thesis. This is a true copy of the thesis, including any required final revisions, as accepted by my examiners.

I understand that my thesis may be made electronically available to the public.

Abstract

Powder bed fusion is a class of additive manufacturing (AM) technology capable of fabricating complex geometrical designs and empowering users with a variety of benefits. Two main examples are laser powder bed fusion (LPBF) and electron beam powder bed fusion (EB-PBF) known as electron beam melting (EBM). Both techniques follow a layer-by-layer fabrication manner whereby each layer is melted according to individual cross-sectional slices of a computer aided design model. Despite its escalating enticement and prominence in both research and industry, the application requires significant research to understand the interplay between process parameters and materials. An example of a group of alloys are nickel superalloys, which can be further classified as weldable and non-weldable nickel superalloys. CM247LC falls in the latter and is associated with a higher volume content of γ' precipitation strengthening phase. The greater γ' (gamma prime) content enhances the mechanical properties for high temperature applications, but also paradoxically contributes to its proclivity for cracking.

The processability of CM247LC via LPBF has been investigated by different researchers from academia and industry. A number of traditional and creative strategies were explored to minimize the crack susceptibility of CM247LC but this was at the cost of undesired compromises. Conversely, the differences in the deposition process and conditions primes the less explored EBM to be an appealing processing alternative. The current work explores the processability of CM247LC by EBM with the desired target of mitigation the material susceptibility towards cracking. The process optimization requires a fundamental understanding of process parameters and the solidification process of the deposited material. This study follows a systematic ground up approach to address the knowledge gap. This started with the basic deposition unit of a single-track and later progressed with multi-tracks.

An experimental single-track study, structured within a design of experiment (DoE) framework, was conducted to isolate the primary EBM process parameters and evaluate their effects on the track stability, microstructure, and cracking behavior. A process map was developed to identify parameter combinations that yielded coherent and uniform tracks. Relationships among EBM parameters, melt pool morphology, grain microstructure, and cracking tendencies were established, revealing specific track conditions and inherent characteristics that mitigate cracking.

The lack of an integrated characterization system within the build chamber complicates direct analysis of solidification conditions for these single-tracks. To address this, a simplified thermal model by finite element (FEM) method was developed to provide an alternate approach to study the solidification conditions. The thermal profiles for each experimental single-track were simulated, enabling extraction of key solidification parameters, such as thermal gradient, and cooling rate, and analysis of their spatial-

temporal evolution. Furthermore, the relationship between process parameters, thermal conditions, and cracking behavior were defined, identifying certain thermal profiles that reduce cracking severity.

Building on this foundation, the study progresses to single-layer deposition involving multiple tracks extending the single-track findings. Two distinct single-track process parameter recipes were selected to assess heat accumulation effects originating from the lateral stacking of tracks. The lateral arrangement was modulated using independent variables: line offset and track number. The impacts of these variables on deposited layer quality, multi-track microstructure, and cracking behavior were assessed. The different single-track parameter recipes indicated contrasting multi-track deposition nature as reflected by surface topography analysis and subsequent assessment of the multi-track cross section. Moreover, a distinct spatial pattern of defects was observed. While these established relationships and findings point toward optimal multi-track conditions, further refinement and follow-up strategies are necessary to fully optimize the process.

Acknowledgements

First and foremost, I would like to express my deepest appreciation to Professor Ehsan Toyserkani for granting me the opportunity to advance my education and gain invaluable experience in the field of additive manufacturing. In addition, I am especially grateful for his continuous guidance, persisting patience, and steady support throughout the entirety of the MASc program.

Second, I would like to also thank Dr. Reza Esmaeilizadeh, Dr. Farzad Liravi, Dr. Paria Karimi, and Dr. Esmaeil Sadeghi for the initial opportunity and collaboration at the Multi-Scale Additive Manufacturing (MSAM) lab. Without their initial belief and trust, I would not have had the chance to begin my journey as a Co-op student at MSAM, which has since allowed me to immerse myself in the field of additive manufacturing. I would like to further acknowledge Dr. Paria Karimi, and Dr. Esmaeil Sadeghi for the technical discussions as well as the initial single-track experimental plan that laid the foundation for this research endeavour.

Additionally, I would like to express my appreciation to the entire team at MSAM for the friendly and collaborative environment. I would like to thank Jerry Ratthapakdee and Shashi Kiran for their assistance with setup of the experimental EBM prints. Moreover, special thanks are given to Dr. Tatevik Minasyan, Dr. Pablo Enrique, Dr. Mahyar Hasanabadi, Dr. Shahriar Imani Shahabad, Mr. Mingzhang Yang, Ms. Nadia Azizi, Mr. Joseph Orakwe for their encouragement, support, and camaraderie throughout my studies.

Finally, I wish to convey my sincerest gratitude to my loving parents, brother, sister, and Eve Moua for the unwavering support and unconditional love. Your sacrifices do not go unrecognized, and your constant encouragements are always cherished. You are my bedrock that inspires and motivates my endeavours to pursue the best version of myself.

Table of Contents

AUTHOR'S DECLARATION ii

Abstract iii

Acknowledgements v

List of Figures ix

List of Tables xii

List of Abbreviations xiii

Chapter 1: Introduction 1

1.1 Problem Overview and Motivation 1

1.2 Thesis Objective 3

1.3 Thesis Outline 4

Chapter 2: Literature Review 5

2.1 Overview 5

2.2 Electron Beam Powder Bed Fusion 5

2.3 Material Information 7

2.3.1 Nickel Superalloy – General Information 7

2.3.2 Nickel Superalloy – CM247LC 9

2.4 Processability by LPBF 10

2.5 Alternative Strategy for CM247LC Processability – EBM Process Optimization 13

2.6 Process Optimization: Single-Track Deposition 14

2.7 Process Optimization: Numerical Thermal Simulation 16

2.8 Process Optimization: Multi-track Deposition 18

2.9 Summary 20

Chapter 3: Experimental Single-Track Study: The Effect of Fundamental Process Parameters 21

3.1 Introduction 21

3.2 Materials and Methods 22

3.2.1 Print Setup 22

3.2.2 Design of Experiment 23

3.2.3 Sample Preparation and Characterization 24

3.3 Results and Discussion 24

3.3.1 Assessment of Track Quality – Surface Topography 24

3.3.2 Microstructure of EBM processed CM247LC: Melt Pool Geometry 27

3.3.2.1 Geometric Comparison of Melt Pools 27
3.3.2.2 Statistical Analysis of Primary Process Parameter Effects 29
3.3.3 Defects 31
3.3.3.1 Identification of Defects in EBM processed CM247LC 32
3.3.3.2 Cracking Behavior of EBM processed CM247LC 34
3.2.4 Microstructure 37
3.2.4.1 Microstructure – Gamma Prime 37
3.2.4.2 Microstructure – Grain Structure 38
3.4 Summary 42
Chapter 4: Finite Element Modelling of EBM deposited Single-Tracks 43
4.1 Introduction 43
4.2 Model Setup 44
4.2.1 Governing Equations and Boundary Conditions 44
4.2.2 Heat Source Model 45
4.2.3 Material Properties 45
4.2.4 Mesh Description 48
4.3 Results and Discussion 50
4.3.1 Calibration of the Model 50
4.3.2 Temperature Distribution Within the Melt Pool 52
4.3.3 Evolution of Thermal Variables and the Effect of Process Parameters 53
4.3.4 The Effect of Melt Pool Morphology and Thermal Variables 56
4.3.5 Influence of Solidification Conditions on Cracking 57
4.4 Summary 59
Chapter 5. Multi-Tracks: Study of Line Offset and Thermal Accumulation on CM247LC 60
5.1 Introduction 60
5.2 Materials and Methods 61
5.2.1 Print Setup 61
5.2.2 Experimental Design 62
5.2.3 Sample Preparation and Characterization 65
5.3 Results and Discussion 65
5.3.1 Assessment of Layer Uniformity – Surface Topography 65
5.3.2 Microstructure: Melt pool geometry of EBM deposited CM247LC multi-tracks 68
5.3.3 Crack Behavior of EBM deposited CM247LC multi-tracks 71
5.3.4 Microstructure: Grain Structure 76

5.4 Summary 78
Chapter 6. Conclusions and Future Work 79
6.1 Conclusions 79
6.2 Future Works 81
Letter of Copyright Permission 83
References 87

List of Figures

Figure 2-1. General internal structure of EBM printer [27] 5
Figure 2-2. Weldability map of nickel superalloys based on Al and Ti weight percent content [21] 9
Figure 2-3. LPBF as-built CM247LC samples after solution treatment at a) 1205 ºC b) 1245 ºC [20] 10
Figure 2-4. LPBF fabricated CM247LC samples with HIP treatment after solution treatment at a) 1205 ºC, b) 1215 ºC, 1230 ºC, and 1245 ºC [20] 10
Figure 2-5: Optical microscopy image of unetched (a), (c) CM247LC and (b), (d) Hf-free CM247LC (e.g. CM247LC NHf) cross sections fabricated by two separate build conditions involving different LPBF printer and optimized process parameter set. Quantitative assessment of crack behavior of CM247LC and Hf-free CM247LC: (e) mean crack length density, and histogram distribution of crack lengths for (f) CM247LC, and (g) Hf-free CM247LC [18] 11
Figure 2-6. Process optimization process: the systematic ground up approach through the study of basic geometrical build units in EBM deposition 14
Figure 2-7 (a) Process parameter window for single-track stability where region A marks lack of fusion tracks, region B labels discontinuous tracks, region C covers continuous and unstable tracks, and region D indicates continuous and stable tracks. (b) Keyhole porosity associated with keyhole melt modes (c) edge cavity associated with melt pools deposited by high laser power and speed [55] 15
Figure 2-8. SEM and EBSD images of LPBF deposited tungsten single-tracks where power is constant at 350W and laser speed increases from 200-600 mm/s at a 100 mm/s interval [56] 16
Figure. 2-9 (a)-(d) Isolated timeframes of thermal simulation that highlights melt pool evolution over time for a beam power of 400 W, speed of 300 mm/s and preheat of 1025degC;(e)-(g) thermal simulation prediction results of the melt pool dimensions for EBM various process parameter combination [29] 18
Figure 2-10. (a)-(i) Laser confocal microscopy images and (j)-(o) SEM microscopy images of LPBF deposited SS316L/CuSn10 multi-track with varying hatch distance (indicated by T) but fixed layer thickness (H), laser power, and scan speed; (p) Graphical illustration of the identified crack mechanisms [67]. Note, the samples are in the etched condition after treatment by Keller's reagent. 19
Figure 3-1. (a) Schematical design of single-track deposition on substrate and (b) image of final single-track build 22
Figure 3-2. Surface topography overview of selected process parameter combinations for the assessment of build quality based on track coherency and stability 25
Figure 3-3 Track examples of defined track quality grades 26
Figure 3-4. An established process parameter window for acceptable track quality based on the criteria of continuity and uniformity 26

Figure 3-5. Scatterplot overview for a qualitative comparison of melt pool geometries corresponding to different beam current-speed combinations under the focus offset of (a) 10mA, (b) 20mA, (c) 30mA 28
Figure 3-6. Quantitative comparison of the effects of linear energy density on (a) melt pool width, (b) melt pool depth, (c) melt pool aspect ratio, and (d) the effect of focus offset on melt pool aspect ratio 29
Figure 3-7. SEM micrographs for the identification of defects such as (a) lack of fusion and gas porosity at 173x, and solidification cracks, liquation cracks, inter-dendritic porosity, and shrinkage pores at (b) 1.5kx in etched condition and (c)-(e) at 1.2 kx magnification in the pre-etch condition 32
Figure 3-8. SEM micrograph providing a macro- and micro- scale view of defects at (a) 182x, (b)-(c), 1.2kx 33
Figure 3-9. The effect of line energy density on (a) average max crack length, (b) average crack length, and the effect of focus offset on (c) average max crack length, and (d) average crack length.....34
Figure 3-10. Crack length density as a function of melt pool aspect ratio. Note, the purpose of the dashed lines is to serve as reference lines and not a line of best fit.....35
Figure 3-11. Melt pools in the (a) pre-etch and (b) etch condition for process parameter combination of focus offset = 10 mA, beam current = 5 mA, and beam speed = 1200mm/s 36
Figure 3-12. SEM micrographs reveal microstructural gradient from (a) the single-track body, (b) few layers below the top surface of substrate, (c) middle of substrate, and (d) bottom of the substrate.....37
Figure 3-13. EBSD grain mapping of EBM deposited CM247LC single-track.....38
Figure 3-14. EBSD IPF Y maps of EBM deposited CM247LC single-track.....39
Figure 4-1. Temperature dependency of the following material properties for CM247LC: (a) density, (b) heat capacity, (c) convective heat transfer coefficient, (d) thermal conductivity 46
Figure 4-2. Simulation details: (a) hybrid tetrahedral mesh scheme for the focus offset 10 and 20mA data subset and (b) uniform tetrahedral mesh scheme for focus offset of 30 mA; (c) simulation time for focus offset 10 and 20 mA data subset (d) simulation time for focus offset 30mA 49
Figure 4-3. Mesh Sensitivity analysis by (a) maximum surface temperature and (b) simulation time as done with uniform mesh sizes and parameter set of focus offset 30 mA, I = 8 mA, and v = 800 mm/s.....49
Figure 4-4. Comparison of the experimental and simulation results of melt pool depth and width for (a) focus offset 10 mA, (b) focus offset 20 mA, and (c) focus offset 30 mA 51
Figure 4-5. Graphical overview of 3D simulation results for select parameter combinations at fixed time 52
Figure 4-6. Temperature profiles of parameter combination 5 mA, 300 mm/s for focus offset of (a) 10mA, (b) 20 mA, (c) 30 mA as measured by d) the probe points illustrated in schematic diagram.....53
Figure. 4-7. Spatial variation of thermal (a) thermal gradient and (b) cooling rate along the central z-axis within a melt pool for the experimental group of 20 mA focus offset.....54

Figure 4-8. The cooling rate as a function of (a) speed for focus offset 20 mA and (b) LED 55
Figure 4-9. The thermal gradient as a function of (a) speed for focus offset of 20 mA and (b) LED 56
Figure 4-10. Correlation between melt pool aspect ratio and solidification parameters: (a) thermal gradient, and (c) cooling rate 56
Figure 4-11. The behavior of crack length density as a function of (a) max thermal gradient, and (c) max cooling rate 58
Figure 5-1. The workflow of the experimental multi track starting from the (a) build design, (b) to print completion, and (c) post recovery state 61
Figure 5-2. EBM CM247LC single-track cross section fabricated with a beam current, speed, and focus offset magnitudes of (a) 5 mA, 300 mm/s, 10mA and (b) 11 mA, 1200 mm/s, and 10mA respectively 62
Figure 5-3. Surface topography overview of Group A (I = 5 mA, v = 300 mm/s) for surface quality assessment of the multi-track central segment 66
Figure 5-4. Surface topography overview of Group B (I = 11 mA, v = 1200 mm/s) for surface quality assessment of the multi-track central segment 67
Figure 5-5. Melt pool morphology of CM247LC multi-track. (a) Etched multi-track melt pools without, and (b) with image enhancement for sample corresponding to Group A, track# = 25, line offset = 0.10 mm (c) overall multi-track appearance for Group B, Track#= 25, line offset 0.10 mm and (d) identification of individual overlapping melt pools in multitrack.....69
Figure 5-6. The influence of line offset and number of tracks on the melt pool (a) dimensions with regards to depth and width, and (b) aspect ratio.....70
Figure 5-7. Qualitative assessment of crack behavior of Group A samples: (a) Track# = 50, line offset = 0.04 mm, (b) last few deposited tracks and (c) middle body region of Track#=50, line offset = 0.16mm .72
Figure 5-8. Qualitative assessment of crack behavior of Group B sample of Track# = 50, and line offset = 0.10 mm: (a) region of last few deposited tracks, (b) middle body region, (c) overall multi-track span....73
Figure 5-9. Quantitative assessment of the effect of number of tracks and line offset through VED on the (a) average crack length density and (b) average areal defect density of EBM deposited CM247LC multi-tracks.....74
Figure 5-10. EBSD grain mapping of EBM deposited CM247LC multi-track samples at track# = 25 and with varying line offset.....77
Figure 5-11. EBSD analysis of IPF-Y grain orientation map for EBM deposited CM247LC multi-track samples at a track# = 25 and varying line offset.....77

List of Tables

Table 3-1. Chemical Composition of CM247LC powder....22
Table 3-2. Process Parameters Combinations of Fabricated Single-Tracks....23
Table 3-3. Definition of Track Quality Grade....26
Table 3-4. ANOVA summary for the effects of primary process parameters on the melt pool depth....30
Table 3-5 ANOVA summary for the effects of primary process parameters on the melt pool width....31
Table 4-1. Defined constants utilized in the thermal FEM simulation....48
Table 4-2. Calibration results: heat source model parameters and width and depth percentage error....51
Table 5-1. Comprehensive List of Process Parameter for the Multi-track Study....64
Table 5-2. Comparison of theoretical track overlap....75

List of Abbreviations

AM	Additive Manufacturing
CAD	Computer Aided Design
EBM	Electron Beam Melting
LPBF	Laser Powder Bed Fusion
HIP	Hot Isostatic Pressing
AB	As built
HT	Heat treatment
TET	Turbine entry temperature
BSE	Back scattered electrons
DoE	Design of Experiment
FEM	Finite element method
LED	Linear Energy Density
OM	Optical Microscopy
ANOVA	Analysis of Variance
PDAS	Primary Dendrite Arm Spacing
SEM	Scanning Electron Microscopy
EBSD	Electron Back Scattered Diffraction
dF	Degrees of Freedom
SS	Sum of Squares
MS	Mean Square
HAZ	Heat affected zone
HAGB	High angle grain boundaries
FCC	Face centered cubic
ROD	Rate of Deformation
ROS	Rate of Shrinkage by solidification
ROF	Rate of Feeding
VED	Volumetric Energy Density

Chapter 1. Introduction

1.1 Problem Overview and Motivation

Metal additive manufacturing (AM) leverages software integration into manufacturing engineering by utilizing slices of a computer aided design (CAD) model as blueprints for layer-by-layer material deposition to produce a coherent and tangible part [1], [2], [3], [4], [5]. This exploitation enables benefits such as the streamlining of a production process, product customizability, greater design freedom for more intricate geometries, and part consolidation for better mass-performance-cost efficiency [1], [2], [4], [5]. This contrasts with conventional fabrication methods such as machining and casting. These advantages along with multiple government initiatives by the United States, Germany, Singapore and China push forward the adoption of AM by various companies [1]. General Electric demonstrates this advancement with its GE9X engine, introduced into service on January 2020 [6]. The GE9X engine has been promoted as more powerful than other commercially available models with nearly 50% of its components composed of Ni-based superalloy composition [7]. It incorporates 304 parts that were additively manufactured via electron beam melting (EBM) or laser powder bed fusion (LPBF) technologies [6], [7]. The ingenuity of AM is exemplified by the consolidation of 163 individual components in its heat exchanger into a singular part to foster a 25% and 40% reduction in cost and mass respectively [6]. Evidently, metal AM has a high ceiling potential and is capable of shifting the past paradigms of industrial design and manufacturing practices.

EBM and LPBF are known as powder bed processes due to their shared part fabrication principle which relies on the application of a localized heat source to selectively melt and join successive layers of metal powder spread over a solid substrate [4], [8]. The identity chiefly defers by the heat source employed [3]. EBM was commercialized in 1997 by Arcam AB [4], [9]. The method converts the high kinetic energy of accelerated electrons into thermal energy for localized melting under high vacuum build conditions [4], [9]. Alternatively, LPBF was founded in the 1980s and employs a beam of photons from a laser medium for melting under an inert gas environment [4]. Regardless of the heat source, various process parameters such as the amount of power supplied, scanning speed, beam path separation, and the inter- and intra-layer scan pattern of the traversing beam control the ability of the beam to melt the metal powder into a molten liquid pool [8], [10]. Subsequently, the geometric shape of the melt pools and the material properties of the metal jointly dictate the solidification conditions [8], [9], [10]. Hence, a large emphasis is placed upon understanding the interdependent relationship between the process parameters, material of interest, and the resulting part microstructure as its processability ultimately dictates the quality and mechanical properties of the fabricated part and its suitability for certain applications [8], [9].

Nickel based superalloys are a case example. This class of high performing alloys are valued for their

corrosion resistance and mechanical properties under high temperature applications such as turbine components in the energy and aerospace sectors [3], [4], [9], [11]. The print parameters-microstructure-material properties of alloys such as Inconel 718, Inconel 625 and Hastelloy X have been greatly studied by both powder bed processes and an effective process parameter window that limits the crack occurrence has been defined [3], [12]. However, these weldable nickel superalloys are limited in their high temperature strength due to their lower content of γ'-Ni_3(Ti, Al), the intermetallic precipitation phase that strengthens the base γ nickel matrix [12], [13]. In response, interest has shifted towards non-weldable nickel superalloys such as CM247LC [1], [12]. As the defining non-weldability trait, its higher volume fraction of γ' precipitates, lends to its better high temperature properties such as an elevated creep resistance, yield stress, and thermal fatigue performance [11]-[13]. On this account, the larger γ' content also paradoxically limits the suitability of this subcategory for market applications, as it increases the crack susceptibility and potentially debilitates its mechanical properties [9], [12], [13].

In attempts to mitigate the inherent cracking problem, significant research has been focused on exploring the processability of CM247LC via LPBF and the identification of the reduced processing window [14], [15], [16], [17]. Alongside process optimization, other approaches such as alloy modification [18], [19], post processing treatments [20], and other novel strategies [21], [22], [23], have been explored to reduce cracking and achieve the desired mechanical properties [11], [24]. However, these strategies come at the cost of increased lead times and expenses, or undesired alteration of its mechanical properties. Moreover, the as-built (AB) samples by LPBF are required to undergo a subsequent heat treatment (HT) in order to facilitate growth of the γ' phase to the suitable size and morphology for the target application [14], [25].

As a more recent and less established technology, EBM is a limitedly explored processing route for non-weldable alloys such as CM247LC. In contrast to LPBF, the EBM process is carried out at comparatively higher build temperatures and possesses a preheat step that beneficially lowers the temperature gradients and cooling rates [7], [9], [26]. Consequently, the fabricated part experiences lower residual stress and crack sensitivity [7], [9], [26]. In addition, the EBM conditions of slow cooling and use of a high vacuum serves as an in-situ heat treatment in which would foster the growth of the γ' precipitates while possibly removing the need for post processing, facilitating shorter lead times [7]-[9]. As a result, the favourable synergy of the non-weldable nickel superalloy and EBM merits an assessment of its potential feasibility. An effective approach will be required to study the processability of CM247LC by EBM in a resource efficient manner. This is as opposed to the costly experimental trial and error alternative. A systematic strategy would beneficially maximize the knowledge grasp of the parameter-material-microstructure relationship and enable the identification of suitable process parameters for limiting the crack susceptibility linked with the chosen alloy.

1.2 Thesis Objective

The aim of this thesis is to develop a foundational understanding of the relationship between process parameters and the resulting microstructure in attempts to ultimately identify a suitable set of parameters that limits the degree of cracking in CM247LC samples fabricated via EBM. This overarching aim will be addressed through the following objectives:

- Study the effect of fundamental process parameters (such as beam current, beam scanning speed, and focus offset) on the geometrical dimensions and microstructure of solidified melt pools and to correlate these features to the degree of witnessed cracking. This will be achieved through an experimental single-track print and a design of experiment structure. A set of fundamental parameters will be identified for successive tasks.
- Develop a finite element thermal model to extract the thermal information such as the temperature history, temperature gradient, and cooling rate of the solidified single-track melt pool to better understand the relationship between process parameter and solidification conditions. Ultimately, this will be correlated and used to help better understand the observed cracking behavior by the material.
- Expand on single-track findings by the introduction of line offset parameter in a single layer multi-track study. The study of the different horizontal track arrangements will facilitate an understanding of the isolated heat accumulation effects on the geometrical dimensions, microstructure, and cracking tendencies of ensuing melt pools.

1.3 Thesis Outline

The thesis structure methodically addresses the stated objective by the following manner. Chapter 1 provided a short overview of the field of AM and EBM, with a given focus on the processability of non-weldable nickel superalloys. This helped to set up the problem overview and the motivation, objective, and outline for the current study. Chapter 2 is a literature review that gives further details on the EBM process, nonweldable CM247LC nickel superalloy, and a brief review on the processability of the alloy by AM. Additionally, a systematic approach is outlined for the efficient study of CM247LC processability via the EBM deposition route. The aim of this chapter is to equip readers with the necessary background knowledge for a better understanding of this thesis. Chapter 3 investigates the EBM primary process parameters of beam current, beam speed, and focus offset through the combination of experimental single-tracks and a full factorial design of experiments. The results of the basic build unit (single-track) will define the relationship between primary process parameters, track deposition quality, microstructure, and cracking behavior of EBM processed CM247LC. Chapter 4 addresses the knowledge gap of the experimental single-track solidification conditions. This chapter focuses on the development of a simple thermal model via finite element method in order to extract thermal information of the single-track deposition process. The simulation study of the temperature and its spatial-temporal evolution will help define the relationship between the primary process parameters, solidification conditions, and CM247LC cracking tendencies. Chapter 5 expands on the knowledge fostered in the single-track work done in Chapter 3 and 4, whereby the accumulation of heat from the lateral stacking of multiple single-tracks in a single layer is explored. The lateral arrangement of tracks focuses on the effect of line offset and the number of tracks on the deposition quality, microstructure, and CM247LC susceptibility towards cracking. Lastly, Chapter 6 provides a conclusion to this thesis whereby, key findings are consolidated in a summarized list and recommendations for future work are also provided.

Chapter 2. Literature Review

2.1 Overview

The focus of this literature review is to study the processability of the nickel superalloy, CM247LC by additive manufacturing (AM). An introduction to electron beam powder bed fusion and its process parameters will be discussed. This is followed by a review on relevant material information highlighting its background, strengths, and the inherent challenges associated with the alloy of focus. Significant efforts have been undertaken to successfully fabricate, and process crack free CM247LC parts by laser powder bed fusion. A few of these strategies are highlighted along with the associated trade-offs. Meanwhile, comparatively limited research has been devoted to studying the processability of the alloy by electron beam powder bed fusion. Hence, a systematic ground up approach is proposed to cultivate a foundational understanding between the deposition and solidification process. This would therefore better enable the optimization of EBM-processed CM247LC and the mitigation of its crack susceptibility.

2.2 Electron beam powder bed fusion

Electron beam powder bed fusion, or more commonly referred to as electron beam melting (EBM), was commercialised by Arcam AB in 1997 [9]. As a powder bed AM technology, the layer by layer nature of material deposition enables users to fabricate metallic parts of complex designs. The principal mechanism exploits the high kinetic energy from a beam of highly accelerated electrons and its conversion into thermal energy upon the collisional impact with the powder particles of the powder bed [4], [27]. This is in contrast to its more popular counterpart, laser powder bed fusion (LPBF), where light or photons from a laser source are absorbed by the powder and converted into thermal energy for melting [4]. A generalized internal structure of an EBM printer is displayed in Fig. 2-1.

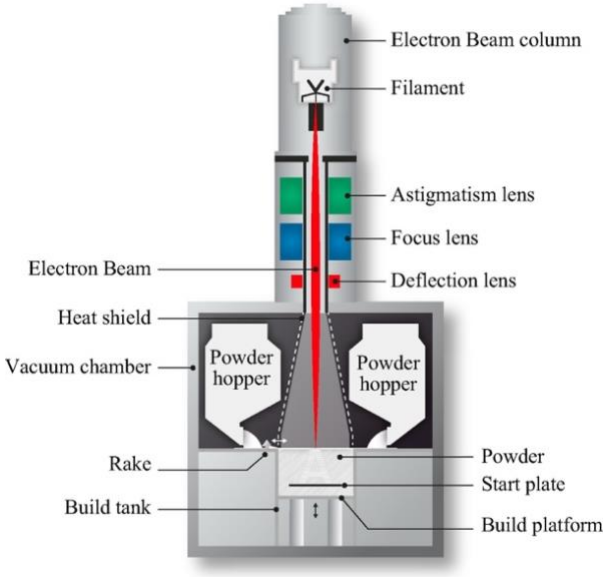


Figure 2-1. General internal structure of EBM printer [27]. Permitted for reproduction by Elsevier.

At the start of the EBM build process, a build processor is used to partition the user designed CAD model into cross sectional slices of a defined layer thickness. The processed CAD file is then transferred to the software of the EBM printer. Once the vacuum conditions are established, a defocused electron beam is used to rapidly scan and preheat the build plate to a specified temperature. The build plate is lowered by the defined layer thickness and a rake arm spreads a fresh powder layer across the plate. Another preheating cycle is applied to raise the temperature of the fresh powder layer and to partially sinter the metal powder of the powder bed. The partial sintering prevents any potential instabilities such as smoking where the electrostatic repulsion is instigated by the buildup of excess charge from the incident electron beam [9]. The melting stage is then performed. The electron beam melts the powder at locations specified by the generated cross-sectional slice using the user programmed process parameters. This leads to the formation of molten pools of material and bonding with previously solidified melt pools and print layer. The unmelted powder will either be part of the surrounding powder bed or embedded within the fabricated part. Both are removed via non-destructive depowdering techniques in the post processing stage. After the melt layer is finished, the build plate is lowered, and a new cycle begins. Multiple cycles of build plate lowering, powder spreading, preheating, and melting are repeated until the fabrication of the entire part is completed.

The success of a print to obtain a desired part quality and mechanical properties relies on the proper selection of process parameters. This controls the complex thermal history of melt pools undergoing rapid heating and cooling during melting and solidification [28], [29]. Several of the key process parameters are listed as follows along with their observed effect on resulting deposited parts:

- **Focus offset**: This controls the amount of current applied onto the electromagnetic field lens used to defocus the electron beam and manipulate its focal point [30]. Ghibaudo et al. [31] revealed a heighten focus offset limits the aluminum loss in EBM processed Ti-48Al-2Nb-2Cr alloy. However, this was also associated with a minor increase in porosity. Abdeen and Palmer [32] observed a greater focus offset values also resulted in density reduction and a worsened surface roughness.
- **Beam current**: The current parameter directly controls the supplied energy input. In a study on the impact of beam current on the mechanical properties and microstructure of Ti-47Al-2Cr-2Nb, Yue et al. [33] found a larger current increased the B2 phase which led to a greater microhardness, but also the secondary result of greater grain sizes and a following weaker compression strength.
- **Beam speed:** This variable governs the distance the beam translates across the print surface per unit time. In processing Ti-6Al-4V, Wang et al [34] had observed that the use of high beam speeds facilitated a finer grain microstructure, and used the Hall Petch relationship to explain the greater hardness and Young's modulus. Puebla et al. [35] also showed higher beam speeds led to an increase in porosity due to unmelted powder, resulting in reduced density, stiffness, and microhardness.

- **Line Offset:** The parameter refers to the offset distance that separates consecutively melted tracks, and thus also dictates the extent of track overlap. In LPBF, line offset is equivalent to the hatch spacing parameter. Ameen et al. [36] explored the role of process parameters in the fabrication of overhang structures with specific focus on the extent of warping deformation. The Ti-6Al-4V ELI overhang was found to experience a greater warping deformation with lower line offset values [36].
- **Layer thickness:** This value governs the vertical height of the fresh powder that is spread for the following new melt layer. Diaz et al [37] found a lower vertical progression of 50 μm instead of 100 μm can result in parts with higher microhardness, yield stress, and elongation.
- **Scan strategy:** The scan strategy is the defined pathing pattern followed by the electron beam during the melting of a given layer. A snake pattern where the electron beam traverses back and forth is a common scan strategy employed for deposition [38], [39], [40]. Helmer et al. [41] highlighted the ability of various scan strategies to foster different solidification conditions such as the altercation of the thermal gradient direction and the resulting grain structure.
- **Scan Rotation:** Each melt layer involves the electron beam to apply the scan strategy with a particular directional orientation. The given variable dictates the rotation of the directional orientation between each successive melt layers. For instance, with a 90º rotation, the melt layers will alternate between latitudinal and longitudinal scan directions. In the fabrication of IN625 trusses by EBM, Zhao et al. [42] highlighted specific rotations were associated with larger magnitudes of thermal gradients which consequently heightened the experienced accumulated strain, deformation and the amount of trusses that had been rupture.

While additional process parameters exist, these couple of parameters can significantly influence the solidification process during deposition. In a numerical investigation of powder bed fusion process by Machirori et al. [43], the inherent temperature gradient is seen to profoundly dictate the residual stress experienced by the fabricated part, with a higher thermal gradient resulting in a higher stress state that can cause defects such as crack. Silvestri et al. [39] also indicated that various combinations of EBM parameters and their interaction with one another can also lead to the same supplied energy density but differing microstructure and mechanical properties. The selection challenge of correct parameter and definition of a suitable process window can be made further complicated by the properties of the interested material.

2.3 Material information

2.3.1 Nickel Superalloy – General information

Nickel based superalloys are remarkable case studies of material engineering. These commonly operate under extreme environmental conditions due to their prized high temperature material properties [3], [4], [12]. Such attributes include excellent tensile strength, corrosion and oxidation resistance, fatigue

performance, and creep resistance [3], [4], [8], [9]. Consequently, nickel superalloys have found applications in the energy sector, automotive industry, maritime vessels, and aerospace sectors [3], [4], [9]

The required material properties and target applications are met by deliberate tailoring of its alloying elemental ratios and following microstructure. The base nickel matrix (γ) is ordered into a face centered cubic (FCC) structure [44]. Its key trait of a wide solubility range enables a plethora of substitutional alloying elements to be strategically included for an intended purpose [8], [44]. For instance, aluminum (Al) and chromium (Cr) addition enhances the resistance of a material towards oxidation and corrosion [12], [44]. Meanwhile, elements such as titanium (Ti), molybdenum (Mo), hafnium (Hf), tantalum (Ta), Cr and tungsten (W) assist in carbide formation that can help limit the grain size, restrict the sliding of grains at the boundaries, and thus provide better creep properties [12], [44]. However, the extent of additional alloying elements can also contribute to a wider solidification range, and consequently render the alloy material to be further vulnerable to cracking [18].

Al and Ti also serve as key constituent elements for one of two possible and important precipitation strengthening phase, $\gamma'$and γ'' [12], [44]. For this work and the alloy of interest, the γ' will be of sole focus. The γ' is an intermetallic FCC phase with a Ni_3(Ti, Al) composition that precipitates out of an undercooled supersaturated solid solution [45], [46]. The γ' phase has been attributed to be a defining trait of nickel superalloys as it enables its enhanced mechanical properties and thermal stability at high temperature conditions through the inhibition of dislocation migration [12], [44]. Despite the benefits of the γ' phase, it can also paradoxically serve as the reason for the shortcoming of the material with regards to processability.

Nickel superalloys can be classified as weldable or non-weldable based on the elemental content of Al and Ti as seen in Fig. 2-2 [7], [9], [21]. This is reflective of the amount of γ' phase. The severity of the non-weldability is correlated to the degree that the sum of the two elements exceed 4.5 wt% as demarcated by the red dashed line [7], [21]. In other words, a greater summation reflects a higher susceptibility for the given nickel superalloy to experience cracking. Weldable nickel superalloys such as IN718 have been extensively studied in AM research and applied in industry [12], [26], [29], [47]. However, in the efforts to innovate and redefine performance limits, endeavours are being explored with the processability of non-weldable nickel superalloys. A prospective application example is seen in gas turbines. The enhanced amount of γ' phase fosters better high temperature mechanical properties that would raise the temperature limit at which combustion gases are injected into the turbine section of the gas turbine engine [12]. This raised turbine entry temperature (TET) would therefore facilitate an upgraded thermodynamic efficiency and power output for mechanical work [12]. Hence, a competitive edge could be realised.

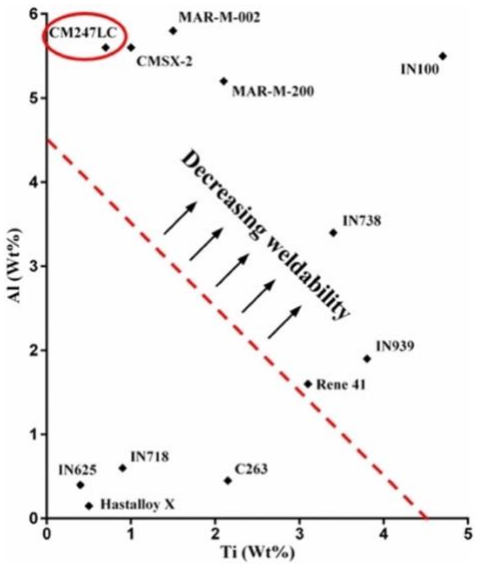


Figure 2-2. Weldability map of nickel superalloys based on Al and Ti weight percent content [21]. CC-BY

2.3.2 Nickel Superalloy – CM247LC

CM247LC is a case example of interested nickel superalloys with such opportunity. The alloy was derived in 1978 from its parent alloy of MAR M247, with the target objective specifically driven towards the production of directionally solidified blades [48]. Certain alloying elements were included such as Ta, Mo, W, Cr, and Co for solid solution strengthening, W and Mo for strengthened creep resistance, and Al and Cr for its oxidation/corrosion resistance [44]. CM247LC differs from its parent alloy of MAR M247 through chemical composition modifications which includes a minor reduction in the amount of W, a tighter control of sulfur (S) and silicon (Si), and a greater limitation of the zirconium (Zr) and Ti content [7], [48]. Consequently, the refined version exhibits a better ability to resist grain boundary cracking and a more favorable carbide stability and microstructure [48]. This translates to an upgraded material and mechanical properties such as a better oxidation resistance, creep strength, fatigue strength, thermal stability, ductility, and high temperature strength [11], [44], [46], [48]. The lower carbon (LC) content alloy can be resultingly applied in propulsion engines and turbine blades of vehicles within the aerospace sector.

As reflected in Fig. 2-2, CM247LC is a non-weldable nickel superalloy with its position well above the red dashed line. This is indicative of the superalloy to be possessive of a very high γ' phase content. In fact, Bassini et al. [20] found the alloy is capable of realising a γ' volume fraction within the range of 65%-73%. Furthermore, as mentioned, this secondary phase importantly contributes to its highly sought after enhanced mechanical and material properties.

However, CM247LC requires post deposition heat treatment processes for the further precipitation and development of the γ' phase in order to attain the desired properties [20], [49]. The characteristics of the γ' strengthening phase such as the degree of lattice misfit between the γ' phase and the γ base matrix, its size,

shape, and distribution are significantly influenced by various heat treatment parameters such as the heat treatment path, subjected cooling rate, treatment duration, and temperature [20], [49]. Two crucial heat treatment phases are the solutionizing and aging stage. The former phase occurs at a higher temperature for recrystallization and sets up the γ' precipitation occurring in the subsequent latter phase at a lower holding temperature [20]. Both Bassini et al. [20] and Muñoz-Moreno et al. [49] observed a higher volume fraction of γ' with an improving uniform distribution and finer morphology can be facilitated with a higher solution treatment temperatures such as that close to and above the γ'solvus temperature range (1230ºC-1245 ºC), followed by a fixed aging stage. Fig. 2-3 and Fig. 2-4 are backscattered electron (BSE) images of LPBF fabricated CM247LC samples that have undergone solution treatment for 2 hours and first aging treatment for 4 hours at 1080 ºC [20]. The first figure displays the direct as-built (AB) samples while the following figure correspond to AB samples that have also undergone hot isostatic pressing (HIP) process.

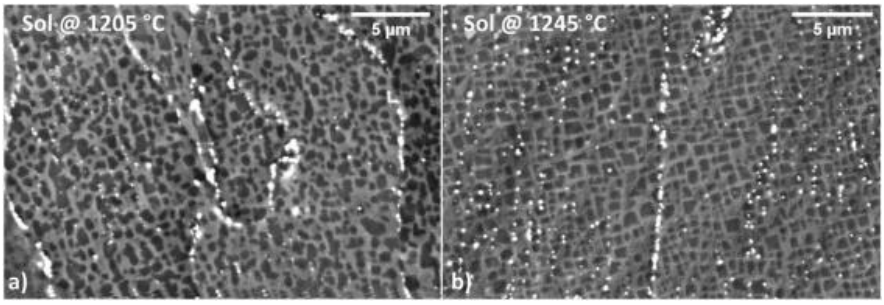


Figure 2-3. LPBF as-built CM247LC samples after solution treatment at a) 1205 ºC b) 1245 ºC [20]. CC-BY-NC-ND

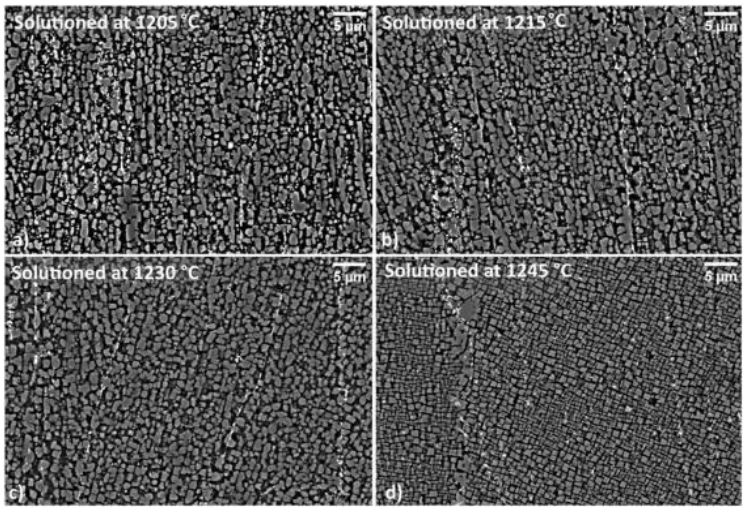


Figure 2-4. LPBF fabricated CM247LC samples with HIP treatment after solution treatment at a) 1205 ºC, b) 1215 ºC, 1230 ºC, and 1245 ºC [20]. CC-BY-NC-ND

2.4 Processability by LPBF

Conventional manufacturing techniques can be used to process CM247LC and fabricate complex designs. Nonetheless, the traditional approach suffers from various drawbacks in the form of substantial material waste, and monetary and time costs [3], [11], [20]. In the recent decade, the application of additive

manufacturing has garnered interests with a surge in studies focusing on the successful processability of CM247LC via LPBF. The processability specifically deals with the minimization of the crack susceptibility for the non-weldable nickel alloy. Several approaches with LPBF have been explored to foster the production of a crack free part.

An alloy chemistry modification approach has been studied to meet the mentioned objective. Griffiths et al. [18] characterized the defects and microstructure of AB samples from two separate build conditions consisting of different LPBF printers and process parameter sets. The micro-cracking mechanism and the contributing factors were identified. Most of the cracks were witnessed to be situated along the grain boundaries with significant degree of Hf enrichment. In response, the removal of Hf, a melting point depressant, was proposed to reduce the solidification range and counteract the cracking observed at grain boundaries. An overall significant reduction in cracking was observed (Fig. 2-5) as the crack length density was lowered from 1.27 and 0.88 mm/mm^2 to 0.12 and 0.03 mm/mm^2 for AB CM247LC and Hf-free CM247LC respectively (Fig. 2-5e) [18]. Markanday et al. [19] also conducted similar work but compensated for the Hf removal with a reduction in carbon content and the addition of Niobium (Nb) to provide mechanical strength. However, this led to a greater degree of cracking due to the reduced presence of carbides [19]. The approach to altering the alloy chemistry may not be attractive as this could also lead to undesired changes in microstructure as well as the mechanical properties and thermal stability of the alloy, designed specifically for high temperature applications.

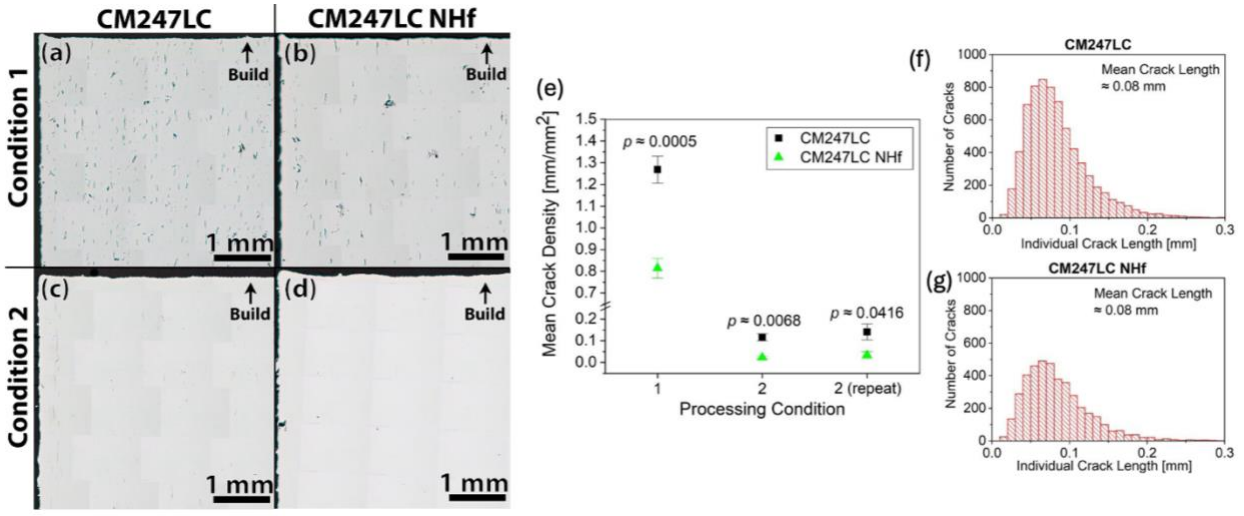


Figure 2-5: Optical microscopy image of unetched (a), (c) CM247LC and (b), (d) Hf-free CM247LC (e.g. CM247LC NHf) cross sections fabricated by two separate build conditions involving different LPBF printer and optimized process parameter set. Quantitative assessment of crack behavior of CM247LC and Hf-free CM247LC: (e) mean crack length density, and histogram distribution of crack lengths for (f) CM247LC, and (g) Hf-free CM247LC [18]. Permitted for reproduction by Elsevier.

The use of post deposition treatments has also been explored. The application of HIP on LPBF fabricated CM247LC samples was studied by Bassini et al. [20]. The HIP cycle was conducted at the γ' sub-solvus regime and it was seen to supplement the later heat treatment and stabilize the microstructure [20]. Specifically, it helped to limit the carbide coarsening and enhanced the controlled growth of finer γ' and volume fraction [20]. HIP was also importantly observed to effectively eliminate the crack and pore defects [20]. However, despite the success of a crack free part, the additional post deposition treatment would incur additional cost and extend the lead times of CM247LC.

Alternative novel approaches have also been pursued to mitigate cracks. Liu et al. [50] utilized a remelting strategy via a low laser energy density and a scan rotation of 90º to inhibit cracks. Lv et al. [23] utilized TiC nanoparticles to partially alleviate the local strain and to strengthen the grain boundaries. As a result, the TiC/CM247LC nanocomposite exhibited decreased sensitivity to cracking. Additionally, the ultimate tensile strength and yield strength was found to improve relative to the original chemistry. Nonetheless, the altered chemistry may also conversely compromise the material performance at high temperatures.

Several studies focused on the interaction between the process parameter and the original alloy material. Consequently, the efforts to better understand the relationship between process parameter and the resulting solidification process, microstructure and part quality, have led to the development of an optimized set of LPBF parameters to achieve a crack free part. Liu et al. [17] explored a widespread combination of process parameters such as laser power, beam speed, scan strategy, layer thickness, and hatch spacing through the substantial number of fabricated dog-bone shaped samples and cubic geometrical samples. While there was no formal statement of a systematic experimental design employed, a process map was established with a parameter combination regime identified to ensure a high-density part. A low laser power for a small depth to width melt pool ratio was observed to reduce the grain misorientation, while a low hatch spacing was found to inhibit the crack propagation and instead promoted partial crack healing via remelting [17]. Moreover, an optimized process parameter set that resulted in a crack free part exhibited heightened UTS and ductility performance in contrast to LPBF fabricated CM247LC from previous studies [17]. Parameter optimization of the LPBF process can successfully lead to a significant reduction of cracks and the capability to produce crack free parts. However, it must be highlighted that due to the rapid cooling associated with the LPBF process, the precipitation and growth of the γ' phase is suppressed in the AB condition [14], [17], [20], [49], [50], [51]. As a result, to promote the precipitation and growth of γ' and reach the desired mechanical properties, AB samples are necessarily subjected to heat treatment. The extra step further adds to the costs and extends the lead times of successful LPBF processing of CM247LC.

2.5 Alternative Strategy for CM247LC Processability– EBM Process Optimization

EBM is a promising alternative for the fabrication of CM247LC. The high building temperature conditions is supplemented and maintained by the combination of vacuum and high preheating temperatures. In return, the conditions within the build chamber during the deposition process serves as an in-situ heat treatment in which alleviates the thermal gradient and residual stress experienced by a part during printing [9], [51], [52]. This can potentially ease the sensitivity to cracking and promote the successful processing of non-weldable nickel superalloys. Moreover, unlike LPBF, the presence of γ' and carbides are inherent in the AB condition of EBM fabrication [7], [51]. This removes the need for post processing and expedites the lead times. Despite its potential merits, to the knowledge of the author, there exists little to no published work that focuses on the processability of CM247LC by EBM.

For this study, the process optimization approach will be taken to investigate the processability of CM247LC by EBM. The EBM technique is a complex deposition process. The interaction between the electron beam heat source and powder particles give rise to a number of dynamic physical phenomena [4], [29], [53], [54]. The manner the interaction evolves, and the solidification process of the material is greatly influenced by the EBM process parameters. Furthermore, as mentioned previously, given the various parameters that exist, the selection of process parameters is further complicated by the given alloy properties. Therefore, a systematic process is central to better comprehending the parameter-material relation and to correlate the relationship with the cracking tendencies of CM247LC.

A ground up understanding can be fostered through a scaling study of basic building block geometries. This step-by-step assessment includes single-tracks, single layer of multi tracks, and a multi-layer cube unit as seen in Fig. 2-6. Due to the time constraint of the research, this work only focuses on the first two listed building blocks. Their definition and significance are further elaborated in the proceeding sections. The use of statistical experimental designs can beneficially expedite the optimization process and the study of a given building block geometry. Similar to the process optimization by Liu et al. [17], Adegoke et al. [14] also conducted a process optimization for the processability of CM247LC by LPBF. The process parameter study employed a 3^3 full factorial design of experiment (DoE) where a reduced number of cubic samples were used to efficiently isolate the statistical significance and influence of the selected process parameters. In accordance, the interaction between power and hatch spacing was also found to be significant in the final crack density of fabricated part. Moreover, a process parameter window was established to limit the number of defects and specific energy density thresholds were found to mark the risk of void presence and the proclivity for cracking.

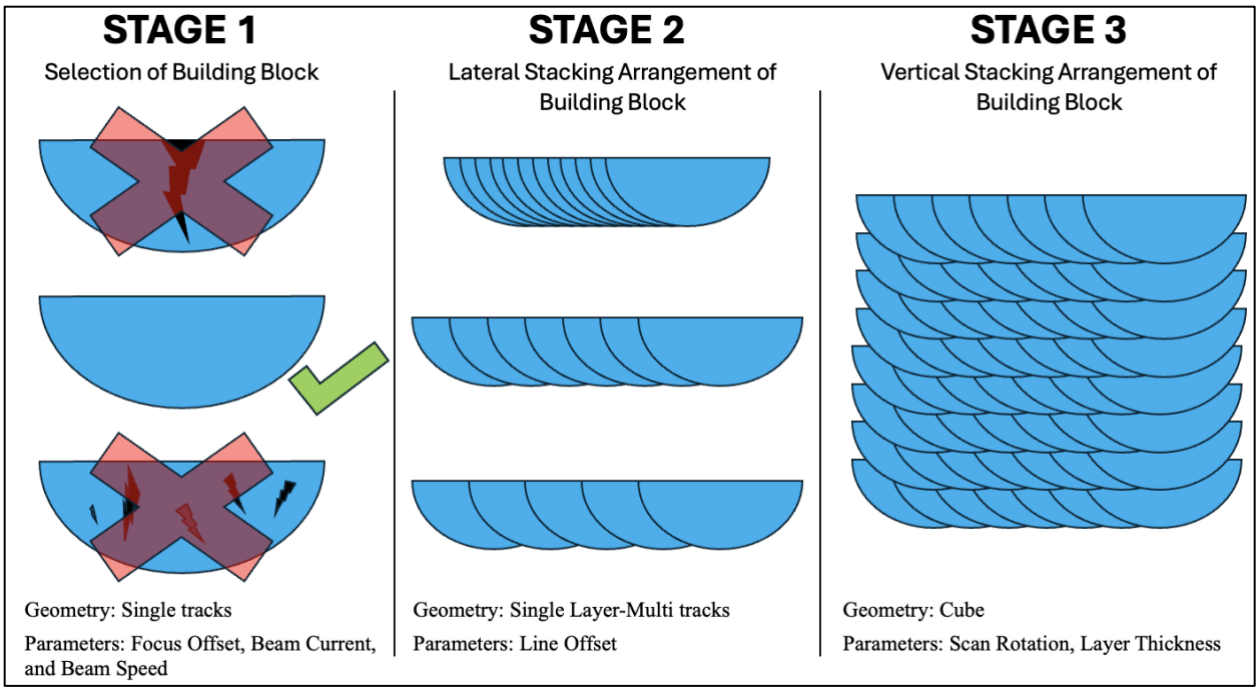


Figure 2-6. Process optimization process: the systematic ground up approach through the study of basic geometrical build units in EBM deposition

2.6 Process Optimization: Single-Track Deposition

The single-track can be considered as the most fundamental building block in the deposition process [8]. The cross section of the singular scan line enables an isolated view of the mesoscale product between the powder particle and electron beam heat source interaction. In other words, a simplified focus is provided on the generated volume of melted material. Several key details can be gleamed from the melt pool feature such as the fostered melt pool morphology, inherent microstructure, and the propensity for defects [8], [10].

In elaboration, the study of the single-track is advantageous because their geometry is chiefly controlled by the primary process parameters such as beam current, speed, and focus offset [54]. Hence, the isolated examination fosters the comprehension of the relationship shared between process parameter, material solidification behavior, microstructure, and resulting part properties, such as crack susceptibility [4], [8], [54]. By leveraging on such insights, unstable and poor quality tracks can be avoided. Thereby, the further propagation of defects through subsequent stacking of a compromised track is also prevented.

Hu et al. [55] deposited single-tracks with various beam power and speed combinations in an attempt to optimize the processability of SS316L deposition by LPBF. The endeavor led to the development of a process parameter window to help navigate through the different track states as seen in Fig. 2-7a. Moreover, the cross-sectional analysis revealed defect patterns linked with certain melt pool morphology. Porosity was commonly found to be associated with a deep melt pool (e.g. keyhole) (Fig. 2-7b) while an apparent edge cavity was connected with the use of high laser power and speed (Fig. 2-7c) [55].

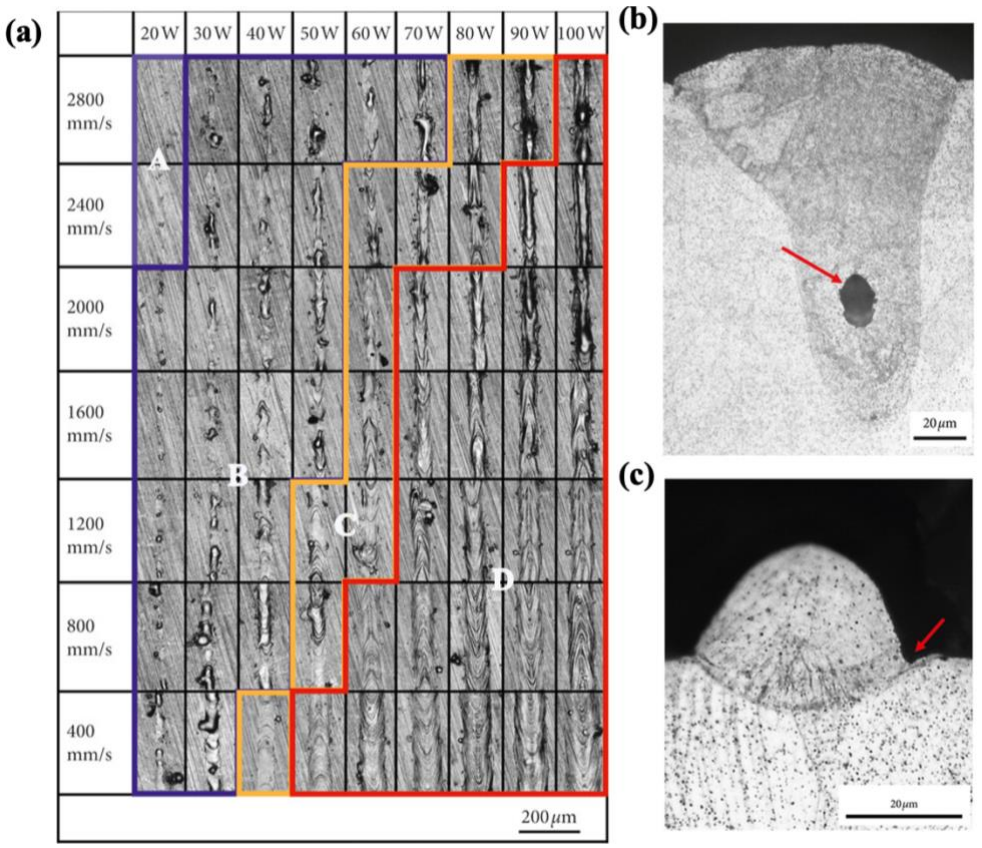


Figure 2-7 (a) Process parameter window for single-track stability where region A marks lack of fusion tracks, region B labels discontinuous tracks, region C covers continuous and unstable tracks, and region D indicates continuous and stable tracks. (b) Keyhole porosity associated with keyhole melt modes (c) edge cavity associated with melt pools deposited by high laser power and speed [55]. Note a slight modification was done in (a) for the sole purpose of improved clarity. CC-BY

In a separate single-track study, the correlation between process parameter, microstructure, and cracking were shown. Chen et al. [56] systematically studied the processability of tungsten in LPBF by scaling the build geometry, starting with single-track deposition. Fig. 2-8 depicts a side-by-side scanning electron microscopy (SEM) and electron backscattered diffraction (EBSD) image comparison of single-tracks with a constant beam power of 350W and decreasing beam speed [56]. As the speed is reduced, the melt pool size along with the proclivity for a crack to occur increased [56]. The crack extended across the top surface to the bottom boundary of the melt pool. The EBSD results also enabled a better understanding of the crack behavior where the location of the crack occurrence and propagation was found to coincide along the formed grain microstructure centerline within the deposited melt pool. Separately, the decrease in beam speed was also found to facilitate larger grain sizes within the central melt pool region.

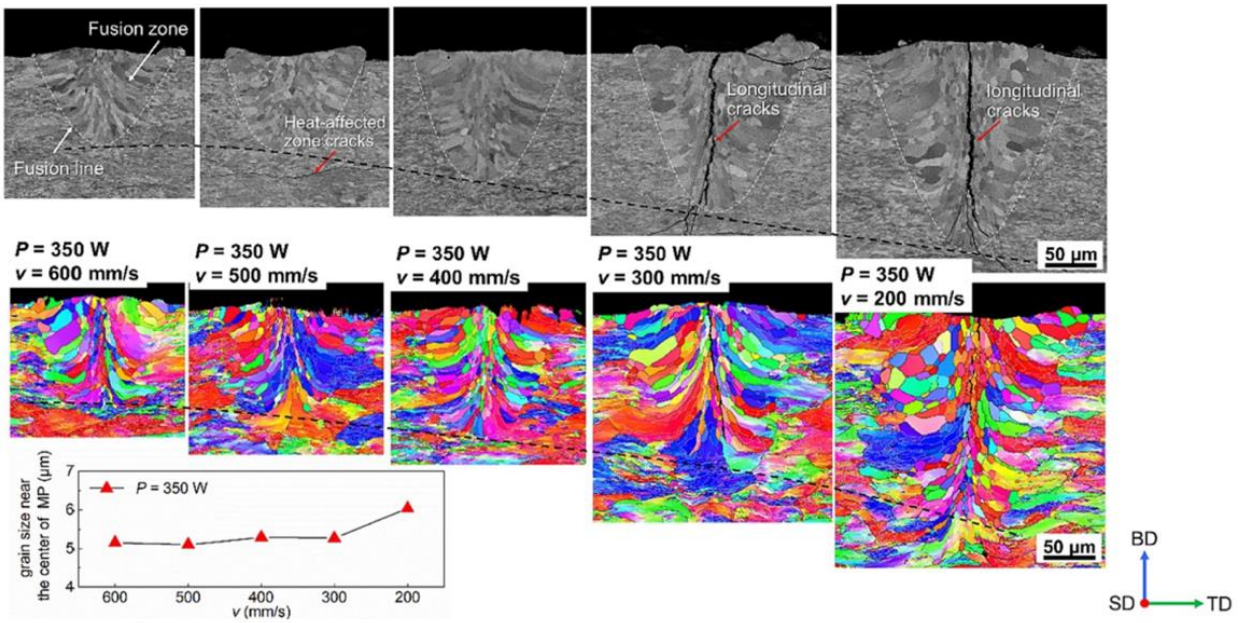


Figure 2-8. SEM and EBSD images of LPBF deposited tungsten single-tracks where power is constant at 350W and laser speed increases from 200-600 mm/s at a 100 mm/s interval [56]. CC-BY-NC-ND

2.7 Process Optimization: Numerical Thermal Simulation

The high temperatures of an EBM build chamber and sensitivity of an electron beam makes it difficult to include an in-situ characterization instrument. As a result, this poses a challenge to quantitatively characterize and follow the ongoing solidification process and the spatial-temporal thermal evolution of each scan track. An extensive number of studies have alternatively resorted to the use of numerical models. Several examples used to study the EBM solidification process include grain evolution models such as cellular automata method [57] or computational fluid flow models via Lattice Boltzmann method [41]. However, finite element method (FEM) is a less computationally intensive method that has been more widely used for the study of melt pools and their thermal history [27], [28]. Their implementation enables the extraction of thermal variables that describe the solidification process such as the solidification rate, thermal gradient, and the cooling rate. Consequently, modelling efforts can effectively serve in a supplementary role to help elucidate experimental findings from sample characterization as well as reduce the number of sample trials required. Beneficially, resources and waste are efficiently managed in contrast to an exhaustive trial and error experimental method [27], [28].

The foundation of thermal numerical models centrally employ Fourier's law of heat conduction and the conservation of energy to study the transfer of heat within the system [27], [28], [58]. The simulation has several key elements which includes the powder layer and solid substrate geometrical domains, a heat source model that represents the electron beam, and the modelling of material properties for the powder and solid bulk phase.

The analysis of heat transfer involves certain assumptions to be made in each involved element. On the application of Fourier's law of heat conduction, the role of fluid flow (e.g. Marangoni convection) is ignored and perfect wetting is also assumed [27], [59], [60]. [61]. Separately, in the consideration of heat lost, certain process mechanisms can be overlooked. Shen and Chou [59] and Cheng et al. [60] ignored the convective heat lost between the chamber environment and powder layer surface due to the high vacuum conditions of the build process.

For the geometrical domain, the powder particle layer is commonly treated as a single continuum as oppose to individualistic particles to simplify the required computational power and time [27], [28], [58]. In addition, different mesh schemes can be applied over the powder and bulk substrate geometrical domain. Riedlbauer et al. [58] utilized an adaptive mesh scheme where finer mesh sizes was applied for regions in closer proximity to the traversing heat source while a coarser mesh sizes was utilized for regions further away from the incident beam. Therefore, with a rougher approximation applied in non-interested regions, computational efforts can be conserved.

Analytical models are used to represent the applied heat source. The various heat source models make assumptions about the shape and the energy distribution character of the beam. Shen and Chou [59] employed a conical heat source with a Gaussian energy distribution that linearly decays with increasing penetration depth. An et al. [62] similarly used a conical heat source and incorporated a parabolic decay with increasing depth. A Goldak double ellipsoidal heat source model was also employed separately where the energy exponentially decays from the beam origin and the three dimensional heat distribution is controlled by the beam dimensional parameters of width, depth and the lengths of the front and rear section[62]. In contrast to volumetric heat source models, Ding et al. [29] employed a Gaussian heat source model that exponentially decays with increasing radial distance. Another category of heat source model derives its energy distribution based on Monte Carlo simulations that study the trajectory and kinetic energy levels of individual electrons from an electron beam after each collision with the power particles constituting the powder bed. This type of heat source model was seen in the work done by Le et al. [63], Yan et al [64], and Galati et al.[65].

Within the model, the material properties of the solid bulk phase and the solid powder bed phase must be distinguished from one another. The separately defined material properties are an integral part of dictating an accurate thermal response output of an evolving heat transfer study. Several simulation setup adopt the simplification of material properties such as thermal conductivity, specific heat, and density to be constant, and therefore assume a lack of temperature dependency [53], [61], [58]. In contrast, other studies have described the temperature dependent material properties through the tabulation of experimental results or

use of a model in attempts to better approximate the behavior of the material and more accurately study the heat transfer evolution [29], [59], [60], [66].

Ding et al. [29] set up a thermal simulation via finite element analysis to study the thermal response behavior and the solidification conditions of IN718 single-tracks by EBM deposition. Fig. 2-9a-d illustrates the spatial-temporal evolution of the temperature distribution for a given process parameter. Additionally, the model was used to simulate the melt pool dimensions as seen in Fig. 2-9e-g [29]. The melt pool boundaries are demarcated by temperature regions that exceed the liquidus temperature of 1336ºC [29]. The predicted width and depth were compared to the dimensions associated with the experimental single-track in order to assess the validity and accuracy of the thermal simulation prediction. Ultimately, the results helped to underline the influence of heat input by process parameters on the material behavior as described by the extracted melt pool morphology and solidification variables such as thermal gradient, solidification rate and cooling rate.

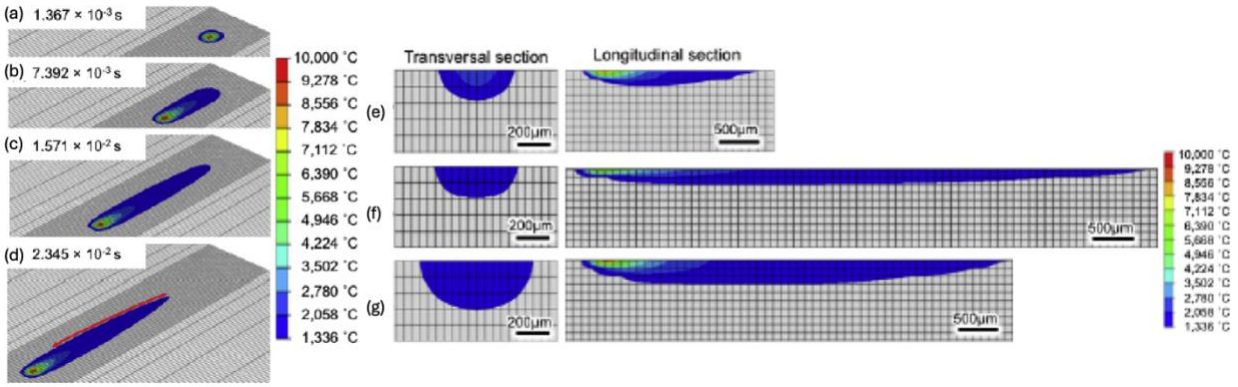


Figure. 2-9 (a)-(d) Isolated timeframes of thermal simulation that highlights melt pool evolution over time for a beam power of 400 W, speed of 300 mm/s and preheat of 1025degC;(e)-(g) thermal simulation prediction results of the melt pool dimensions for EBM various process parameter combination [29]. Permitted for reproduction by Elsevier.

2.8 Process Optimization: Multi-track Deposition

With the objective of a ground up optimization process, the next progression is the geometrical shift from a single-track to multiple tracks in a single layer. The multi-track build geometry focuses on the lateral arrangement of successively stacked single-tracks. As a given track is deposited and undergoes the solidification and cooling process, an adjacent neighbouring track can be simultaneously deposited. To properly facilitate fusion and a solid mechanical bond between tracks, a sufficient degree of overlap must be ensured [8], [47]. The track overlap implies the partial remelting and resolidification of previously solidified melt pools [8]. As a consequence, the local thermal conditions are disrupted, and its spatial-temporal evolution are further complicated [39]. In addition, the degree of track overlap and extent of repeated heating can impact the rate at which heat is accumulated and dissipated within a given unit volume [47].

In this work, the scan strategy and track scan length were kept constant. Accordingly, by using an optimized parameter set that facilitates a stable single-track with a mitigated crack susceptibility, the multi-track build geometry methodically introduces the line offset parameter that controls the extent of track overlap experienced within a single layer of multi-track [8], [40], [47]. By varying the line offset parameter, a closer analysis on the effects from a freshly deposited track and their interaction with previously deposited track can be fostered [53]. This facilitates a further expansion on knowledge of EBM process parameters significance. Specifically, the influence of line offset on the resulting single layer surface quality, microstructure, and crack behaviour can be better comprehended. In addition, the controlled scaling of the number of successive tracks can supplementary further the understanding on thermal evolution within the development of a single layer.

Chen et al. [67] studied the significance of process parameters on LPBF processability of SS316L and CuSn10 multi-material parts. Basic building geometries such as multi-tracks were used to study their impact on the deposited melt pool characteristics. Fig. 2-10a-o highlights the effect of hatch spacing on the varying degree of overlap percentage of successively scanned single-tracks in a single layer [67]. Consequently, the analysis of the line offset variation on the microstructure led to the conclusion of four different crack behaviours. These include the formation of crack isolated within a given melt pool, crack propagation across the meltpool track boundaries, crack propagation into the substrate where deposition occurs, and crack formation from copper penetration into iron regions (Fig. 2-10p) [67].

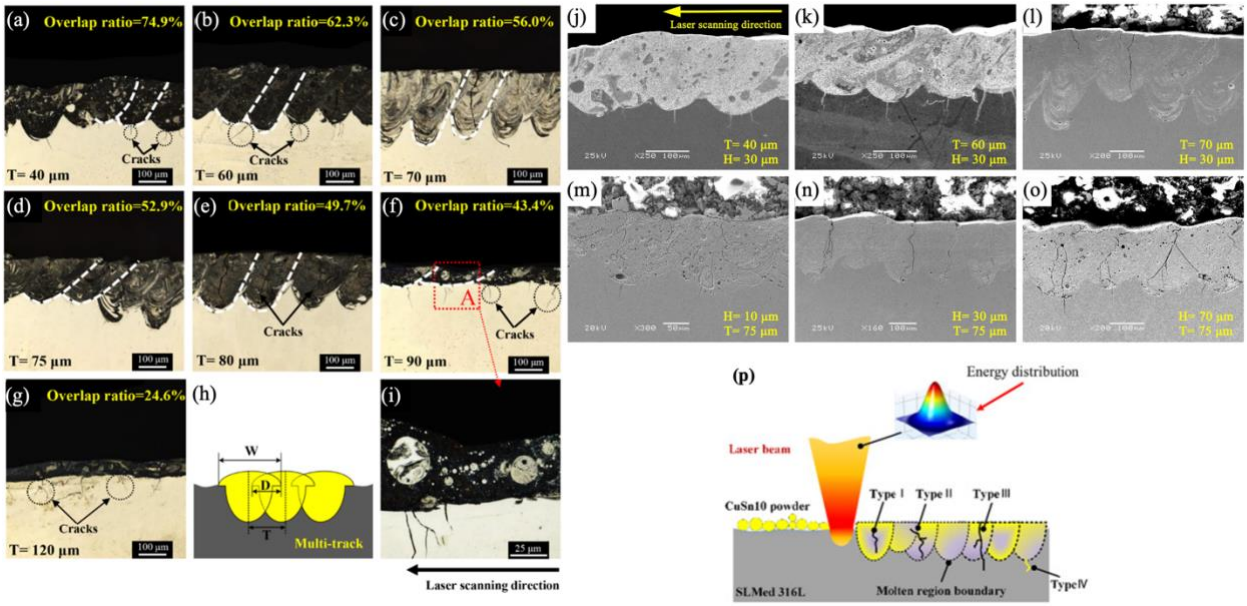


Figure 2-10. (a)-(i) Laser confocal microscopy images and (j)-(o) SEM microscopy images of LPBF deposited SS316L/CuSn10 multi-track with varying hatch distance (indicated by T) but fixed layer thickness (H), laser power, and scan speed; (p) Graphical illustration of the identified crack mechanisms [67]. Permitted for reproduction by Elsevier. Note, the samples are in the etched condition after treatment by Keller's reagent.

2.9 Summary

The CM247LC nickel superalloy poses significant challenges for part fabrication due to its proclivity towards cracking as a non-weldable material. Under the domain of laser powder bed fusion, its processability has been more widely explored where both creative and traditional approaches have been undertaken to address the cracking issue. Despite their attempts, the successes are associated with compromises made with regards to its original composition and material properties or extended lead times due to additional post processing. On the other hand, electron beam melting is an underexplored alternative. The differences in its deposition process provides several advantages and positions EBM as a prospective candidate to mitigate the crack susceptibility of CM247LC. To properly assess the processability of CM247LC by EBM, an understanding between the EBM process parameters and the solidification process is essential. The use of experimental single-tracks and multi-tracks can foster a ground-up understanding of the overall deposition process by providing a breakdown of the complex thermal cycles. In a supplementary role, when conjointly utilized with experimental work, modelling and a design of experiment format can beneficially optimize resources (e.g. material, time, and cost) and further detail certain conclusions. Ultimately, this structured study can foster a comprehension and better define the relationship between process parameters, deposition quality, microstructure, and cracking behavior of EBM processed CM247LC. To the own knowledge of the author, such a ground up and detailed investigation of CM247LC via EBM deposition has not been previously performed, yet it is a necessary study in order to ultimately achieve crack-free parts.

Chapter 3. Experimental Single-Track Study: On the Effect of Fundamental Process Parameters

3.1 Introduction

The EBM process involves a fleeting microscale interaction between metal powder particles and a focused beam of highly accelerated electrons. This interaction triggers a complex interplay of physical principles governing the solidification, including heat transfer, phase change, fluid dynamics, and metallurgical transformations [27], [53], [54]. The complexity escalates with the three dimensionality of the designed print: a single layer involves the lateral overlap of individual melt tracks, while the bottom-up fabrication includes the vertical stacking of melt layers. This further leads to iterative cycles of melting and cooling. With the use of high-energy process parameters, the cumulative effect can induce large thermal stresses within a part and give rise to potential cracking [24]. Conversely, insufficient energy may cause defects. Hence, it is necessary to breakdown the fabrication process and its complex thermal evolution in a systematic step to better understand the effects of process parameter on the solidification process and reach the desired part quality and properties.

The single-track is the basic building block in the powder bed process, whereby multiple units are overlapped to create a single layer. In this regard, the stability of the deposited single-tracks is vital as non-uniform and incoherent tracks can result in dimensional inaccuracies while tracks prone to defects (e.g. pores or cracks) may promote defect propagation in subsequent layers. Additionally, cross sectional analysis of a single-track can also reveal the morphology and size of an individual melt pool, which can be difficult to observe in a scaled-up parts due to the track overlap. These elements hint on the solidification conditions, and thereby the inherent cracking tendencies and initial microstructure formed [8], [10], [54], [29]. The corresponding stability and solidification conditions of a single-track is dictated by primary process parameters controlling the direct energy input. For the EBM process, this includes the beam current, beam scan speed, and the beam size [54]. The beam size is managed by the focus offset parameter whereby a user-defined current is applied to the electromagnetic lens to adjust the focal point of the beam [54]. By the use of single-tracks to isolate and study the effects of primary process parameters, the opportunity to develop a foundational understanding on the ground level of the multi-scale process can be established.

This chapter aims to investigate the effects of primary process parameters such as beam current, scanning speed, and focus offset on the melt pool size and geometry of EBM deposited CM247LC single-tracks. Subsequently, the study explores the correlation of the resulting initial microstructure and cracking tendencies associated with the basic building unit. The results will foster comprehensive insights into the interplay of process parameter, microstructure, and cracking relationship, enabling the identification of an optimal parameter set to minimize cracking in the nonweldable nickel superalloy.

3.2 Materials and Methods

3.2.1 Print Setup

This investigation utilizes argon gas atomized CM247LC powder as provided by Höganäs. The particle size distribution of the metal powder ranged from 45-150 μm. Table 3-1 lists the chemical composition of the powder. It should be noted that feedstock material is comprised of re-used powder.

Table 3-1. Chemical Composition of CM247LC powder

Element	Al	B	C	Co	Cr	Fe	Hf	Mo	Ta	Ti	W	Zr	Ni
Wt%	5.60	0.01	0.06	9.30	8.00	0.03	1.30	0.50	3.20	0.08	9.70	<0.01	Bal.

The design of the print file was prepared on Magics and the design file was printed by Arcam A2X EBM system. The printer uses the conventional tungsten filament for thermionic emission of electrons and subsequently an acceleration voltage of 60 kV was applied. The build conditions include the use of a 304 stainless steel build plate and a partially filled helium vacuum atmosphere of ~$2x10^{-3}$ mbar during fabrication. A preheating temperature of 1000°C and a layer thickness of 70 μm was used.

Substrates with the dimensions of 20×10×3 mm×mm×mm were fabricated with beam current, speed, focus offset, and line offset values of 13.5 mA, 1500 mm/s 20 mA and 0.12 mm, respectively. Subsequently, the single-tracks were printed on the substrates with a track length of 20 mm as seen in Fig. 3-1. The support and substrate component were included to ease post processing. The substrate also helped to avoid undesired dilution effects from the interaction between the build plate and deposited tracks.

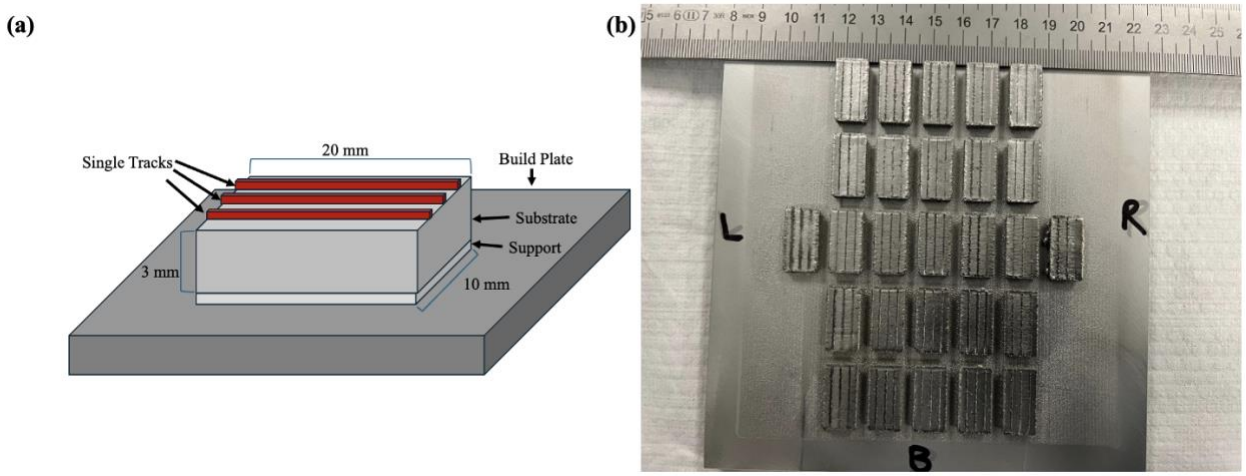


Figure 3-1. (a) Schematical design of single-track deposition on substrate and (b) image of final single-track build

3.2.2 Design of Experiment

Minitab Statistical Software was used to structure a design of experiment (DoE) in order to systematically study the isolated and interactive effects of the three primary process parameters. For each parameter, three levels were used to set up a 3^3 full factorial DoE. The first factor of current includes three magnitude levels of 5, 8, and 11 mA. The beam scanning speed included 300, 800, and 1200 mm/s, and the beam focus offset included 10, 20, and 30 mA. The parameter combinations are listed in Table 3-2. Each unique combination was utilized for three repetitions. The secondary process parameter, linear energy density (LED), is the ratio of beam current and scanning speed. This serves as a holistic measure of the direct energy density input for single-track context. However, a secondary process parameter like such in EBM is limited by the exclusion of the beam size (e.g. focus offset) as the direct relationship is guarded by proprietary confidentiality.

Table 3-2. Process Parameters Combinations of Fabricated Single-Tracks

Sample	Focus Offset [mA]	Beam Current [mA]	Beam Scanning Speed [mm/s]	Linear Energy Density [J/mm]
1	20	5	1200	0.25
2	30	5	800	0.38
3	30	11	300	2.20
4	10	8	300	1.60
5	10	11	800	0.83
6	20	8	800	0.60
7	30	5	1200	0.25
8	20	5	800	0.38
9	20	8	300	1.60
10	10	8	800	0.60
11	30	8	300	1.60
12	10	5	800	0.38
13	20	8	1200	0.40
14	10	11	300	2.20
15	30	8	800	0.60
16	10	5	1200	0.25
17	20	5	300	1.00
18	30	11	800	0.825
19	20	11	1200	0.55
20	10	5	300	1.0
21	20	11	300	2.20
22	30	8	1200	0.40
23	30	5	300	1.00
24	30	11	1200	0.55
25	10	8	1200	0.40
26	20	11	800	0.83
27	10	11	1200	0.55

3.2.3 Sample Preparation and Characterization

The fabricated parts were marked into three equidistant sections and segmented by a Struers 50A25 grade cut-off wheel blade equipped on Struers Labotom-5 abrasive cut-off saw. For each of the three track repetitions, the top and bottom cross sections were used for the statistical analysis of this study. The cross sections were hot mounted using a Stuers CitoPress-5 and Struers PolyFast hot mounting resin. Subsequently, the Labopol-20 was used to grind the mounted cross sections. The metallographic preparation proceeded by a systematic progression of silicon carbide grinding papers from FEPA P grit sizes of 80, 120, 320, 500, 800, 1200, 2400, and 4000. The mounts were polished using a Buehler VibroMet 2 Vibratory Polisher with a Buehler MasterPrep alumina polishing suspension media. The polishing process was carried out for a duration of four and a half hours. The samples were then etched with a Glyceregia mixture comprising of 5 mL of glycerol, 5 mL of nitric acid, and 25 mL of hydrochloric acid.

The surface topography of the middle cross section was evaluated by the Keyence VK-X250 Laser Profilometer to quantitatively assess the track stability. In addition, the Keyence VHX-7000 digital optical microscopy (OM) was also used to provide an overview of the single-tracks through stitch images of 40x magnification. The individualistic cross sections were also captured with a 300x magnification under two sample conditions. First, cross sectional images of the tracks in a pre-etch condition was taken to assess the extent of cracking within the melt pool. Second, cross sectional images of the tracks in the etch condition was taken for melt pool geometrical analysis and microstructure analysis. The measurement analysis was conducted using the ImageJ software. TESCAN Vega3 scanning electron microscopy (SEM) equipped with a Bruker eflash FS detector for electron backscattered diffraction (EBSD) analysis was used to investigate the microstructure of the EBM deposited CM247LC single-tracks.

3.3 Results and Discussion

3.3.1 Assessment of Track Quality - Surface Topography

The combination of 27 process parameter sets and 3 replications resulted in 81 EBM deposited single-tracks. To study the effects of process parameters and define a set of optimal process parameters, an evaluation is firstly made on the overall track quality. This is assessed through the criteria of track coherency and stability. The first criterion is defined based on the track continuity. The second criterion is based on the uniformity and the prominence of defect instabilities within the track body.

The middle segments of selected single-tracks were observed under a laser profilometer and the micrographs in Fig. 3-2 give a topographic overview of the track surface. In general, it is observed that a higher energy input by a higher LED or a more focused beam, fosters a continuous and uniform track body.

In contrast, as the supplied energy density is lowered by means of a defocused beam or LED, the coherency and quality of the track faces degradation. This is prominently shown in samples with a LED level of 0.400 J/mm and the sample parameter combination of 30 mA focus offset and 0.825 J/mm LED level. The listed samples exhibit non-uniformity through a fluctuating track width. Furthermore, instabilities in the form of balling are seen to exist in regions not only limited to the track edges but also in the center body causing elevated regions as highlighted by concentration of red zones. The increased presence of balling defects is attributed to the insufficient energy density supplied to melt the previous layer in order to lower the surface tension for spreading during the deposition process [53], [54]. Thus, the melted particles instead coalesce to minimize its surface area and its surface energy, leading to the shown balling defects [53], [54]. At the critical energy density input such as the process parameter combination of 0.400 J/mm LED level and 30 mA focus offset, the deposited track exhibits both balling defects and lack of fusion defects.

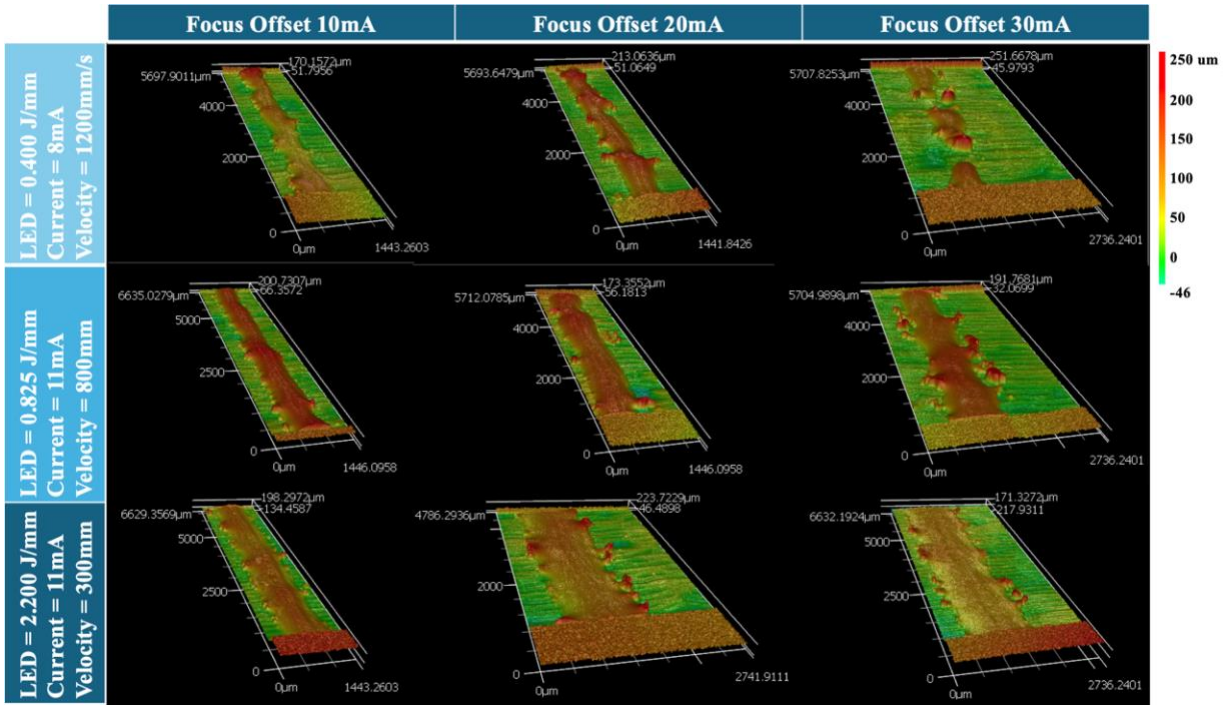


Figure 3-2. Surface topography overview of selected process parameter combinations for the assessment of build quality based on track coherency and stability.

As the overall build is dependent on the single-track quality, a suitable process parameter window is needed for the deposition of continuous and uniform tracks and to avoid a compromised track quality. A quality grade was assigned to each track replicate based on a qualitative evaluation of the stitched optical images encompassing the entire track span. The definition of the quality grade is based on the permutations of the two aforementioned criteria. This is listed in Table 3-3 and track examples are depicted in Figure 3-3.

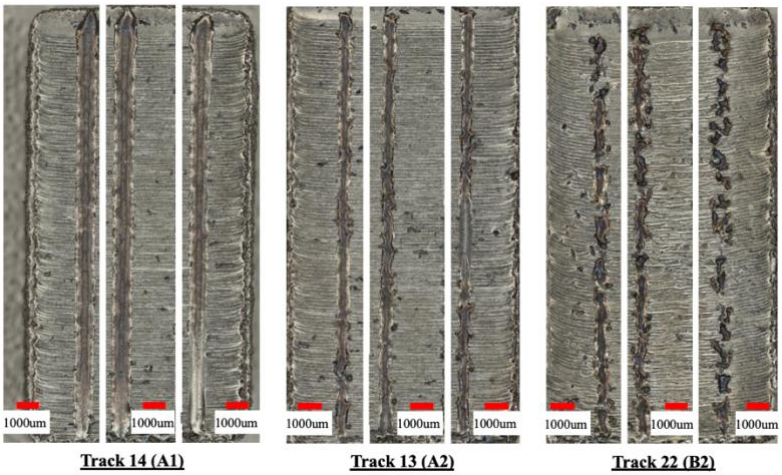


Figure 3-3 Track examples of defined track quality grades.

Table 3-3. Definition of Track Quality Grade

Grade	Definition
A1	Continuous + uniform
A2	Continuous + non-uniform
B1	Discontinuous + uniform
B2	Discontinuous + non- uniform

The established process parameter window is defined in Fig. 3-4. The more extensive qualitative assessment on the process parameter formula and track quality showed similar patterns that were highlighted by the laser profilometer. A high energy input such as a slow current and speed combinations fostered a coherent and uniform track. In addition, a low energy input and higher focus offset facilitated a discontinuous track due to insufficient energy for melting. Meanwhile, observed track irregularities in the form of fluctuating track widths and track necking lend to the non-uniformity within a continuous track. A high beam velocity was observed to be a shared factor in the tracks that classified as B2. The onset of these instabilities by high beam velocities is a consequence of Plateau-Rayleigh instability and asymmetric coalescence in the longitudinal and lateral direction within the melt flow [68], [69], [70], [71], [72].

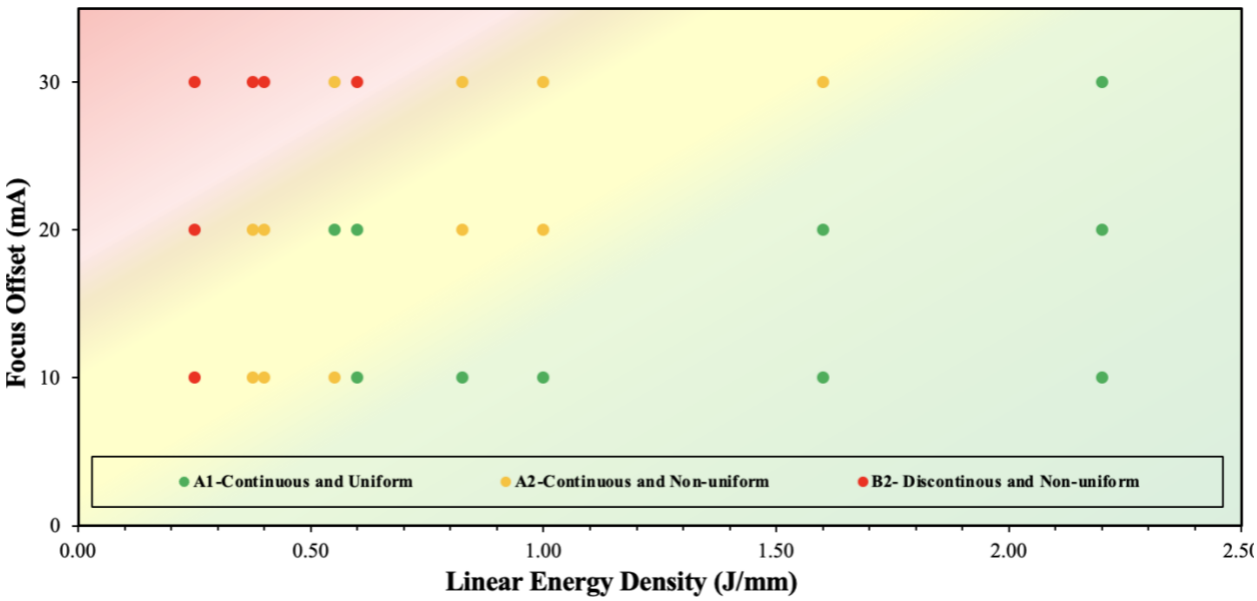


Figure 3-4. An established process parameter window for acceptable track quality based on the criteria of continuity and uniformity.

3.3.2 Microstructure of EBM Processed CM247LC: Melt Pool Geometry

3.3.2.1 Geometric Comparison of Melt Pools

The melt pool geometry is equally critical, as it governs the solidification conditions that facilitate grain microstructure development, the formation of inherent defects, and ultimately the overall performance and associated property of the fabricated part [10]. Fig. 3-5 presents multiple scatterplots of OM images corresponding to the cross section of individual single-tracks. This arrangement of chemically etched melt pools provides a visual comparison of their shape and size. The cross comparison simultaneously highlights the effects of different beam current-velocity-focus offset permutations. Likewise, Fig. 3-6 quantitively highlights the effect of LED and focus offset on the melt pool geometries in terms of width, depth, and aspect ratio as defined by the depth to width ratio. The optimal melt pool morphology will be discussed in later sections.

From Fig. 3-5 and Figs. 3-6a-b, at a constant focus offset, an increase in LED, e.g. by lowering beam speed or increasing current, leads to an increase in the width and depth. This is due to the greater heat flux available for melting. Conversely, an increase in the focus offset facilitates the melt pool to adopt shallower and wider dimensions. The dimensional shift is evidently emphasized by the qualitative comparison of Fig. 3-5, moving vertically downwards from Figs. 3-5a-c. The increase in focus offset leads to a greater amount of current supplied to the electromagnetic lenses in order to shift the focal point of the incident electron beam. This adjustment alters the beam from a finely concentrated spot size following a sharp gaussian energy distribution to a diffused spot size of a broadened energy curve character [30], [31]. In this respect, the observed melt pool morphologies of the focus offset 30mA subset reflect the reduced beam penetration ability and a larger areal spread of lower energy intensities [31]. For Figs. 3-6a-b, the defocusing of the beam translates into a curbed growth rate of melt pool depth and an elevated growth rate of melt pool width as LED is increased.

In Fig. 3-6c, the aspect ratio of the melt pools and LED confirms a positive correlation, whereby the melt pool aspect ratio increases with greater LED magnitudes. Since the increase in LED exhibits an increase in the melt pool width and depth from Fig. 3-6a-b, the increase in aspect ratio indicates that the growth rate of the melt pool depth is greater than the growth rate of its width with increasing LED. On the other hand, the growth rate of the aspect ratio is curbed with a more defocused beam. Consequently, the focus offset parameter can be considered as an effective tool for constricting and shifting the process window of the achievable melt pool aspect ratio to be deposited by beam current and speed combinations, as illustrated in Figs. 3-6d.

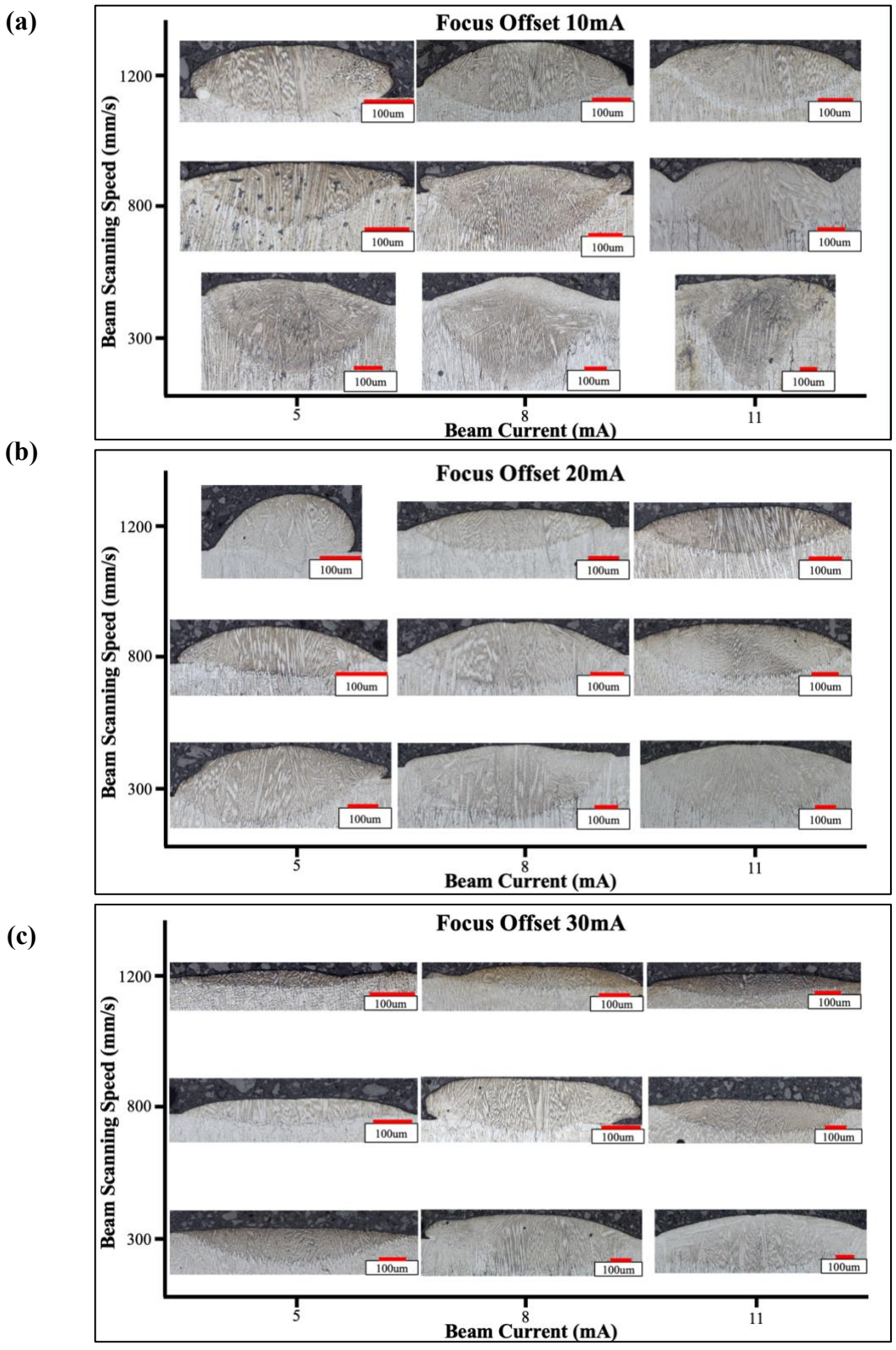


Figure 3-5. Scatterplot overview for a qualitative comparison of melt pool geometries corresponding to different beam current-speed combinations under the focus offset of (a) 10mA, (b) 20mA, (c) 30mA

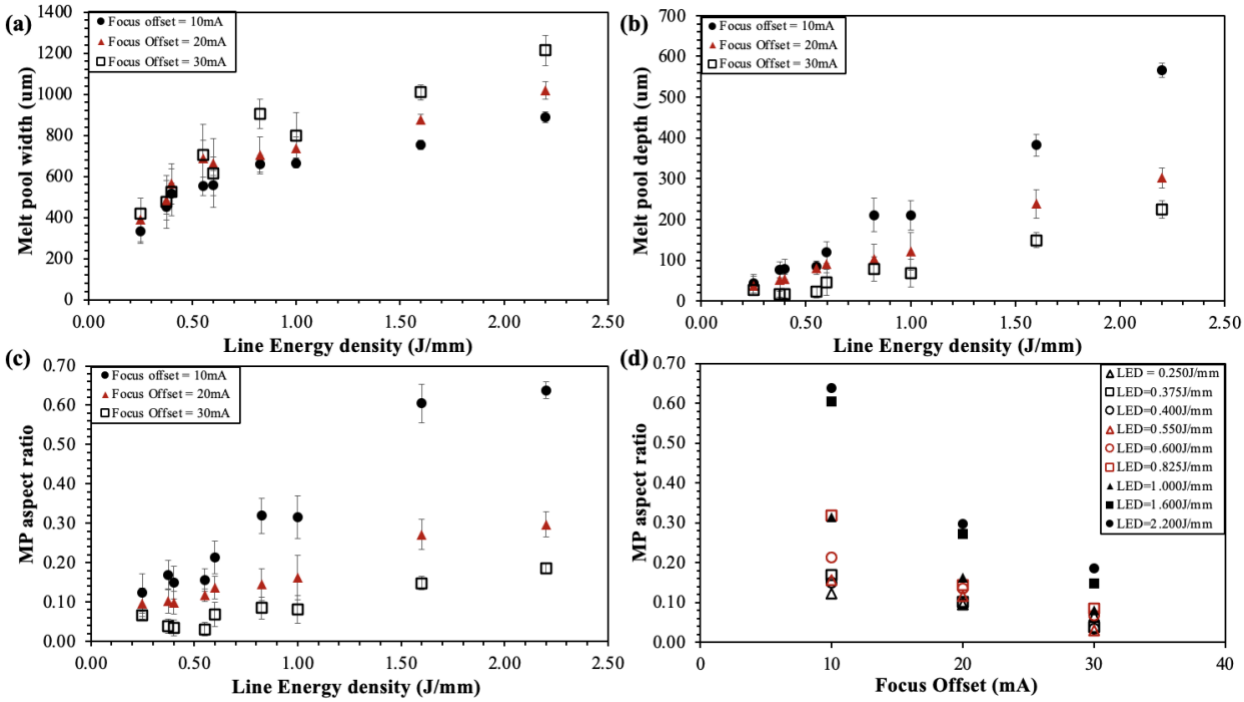


Figure 3-6. Quantitative comparison of the effects of linear energy density on (a) melt pool width, (b) melt pool depth, (c) melt pool aspect ratio, and (d) the effect of focus offset on melt pool aspect ratio

Based on the shallow semicircular shape displayed in Fig. 3-5, most melt pools exhibit a conduction melt mode, where the melting process is driven primarily by heat conduction between the incident beam and the surface layer due to a lower energy density [8], [73]. However, for process parameter combinations of 8 mA and 11 mA beam current, velocity of 300 mm/s, and focus offset of 10 mA, the melt pool geometry shifts towards a near-conical shape with a comparatively deeper depth. In contrast, at the other end of the melt mode spectrum, the keyhole mode occurs under high energy intensity, promoting metal vaporization and recoil pressure [73], [74]. This results in a narrow, significantly larger melt pool depth relative to its width [73], [74]. The keyhole and conduction melt modes can be distinguished by the aspect ratio when values greater than 0.5 indicate keyhole mode, and values less than 0.5 indicate conduction mode [74]. Accordingly, Fig. 3-6c shows that the previously identified melt pools corresponding to 8 mA and 11 mA follow a keyhole melt mode with an aspect ratio of 0.60 and 0.64, respectively.

3.3.2.2 Statistical Analysis of Primary Process Parameter Effects

With the DoE format, statistical analysis in the form of Analysis of Variance (ANOVA) highlights the individual and interactive effects of the primary process parameters on the melt pool depth and width. Table 3-4 and Table 3-5 display the ANOVA results with a confidence interval of 95%. The statistical metrics of the p-value and F-value relative to F_{crit} highlights the statistical significance for each source of variance. For p-value < 0.05, the source of variance is considered significant. For the F-tests, the significance condition relative to random error is when the F-value is greater than F_{crit}. The sum of squares (SS)

highlights the degree in which each source of variance influences the dependent result such as the melt pool width and depth. Therefore, by using the percentage of individual *SS* contribution relative to the total *SS*, the details on the significance of individual or interactive effects of the primary process parameters can be better grasped.

The regression model for Table 3-4 yields an adjusted R^2 value of 0.96, highlighting an excellent fit between the model and experimental data, effectively capturing changes in the dependent variable due to the sources of variance. The *p*-values and *F*-test results confirms that the individual and interactive effect of beam current, scanning speed, and focus offset are statistically significant for melt pool depth. However, the adjusted *SS* contribution of scanning speed (46.12%) reveals it has a greater influence on melt pool depth compared to focus offset (15.24%) and beam current (12.56%). The interactive effects, in contrast, show a lesser extent of influence.

Table 3-4. ANOVA summary for the effects of primary process parameters on the melt pool depth

Variance Sources		Degrees of Freedom (d*F*)	Adjusted Sum of Squares (*SS*)	Adjusted Mean Square (MS)	*F*-value	*P*-value	F_{crit}	Percentage Contribution by *SS* (%)
Individual Factor	Focus Offset	2	192047	96024	140.96	0.000	3.17	15.24
	Beam Speed	2	581065	290532	426.51	0.000	3.17	46.12
	Beam Current	2	158304	79152	116.2	0.000	3.17	12.56
Two-way interaction	Focus Offset * Beam Speed	4	96249	24062	35.32	0.000	2.54	7.64
	Focus Offset * Beam Current	4	27186	6796	9.98	0.000	2.54	2.16
	Beam Speed* Beam Current	4	91750	22937	33.67	0.000	2.54	7.28
Three-way interaction	Focus Offset* Beam speed* Beam current	8	17619	2202	3.23	0.005	2.12	1.40
Error		51	34741	681				
Total		77	1259903					

The model used to study the effects of the primary process parameters on the melt pool width showed an adjusted R^2 of 0.88. This shows a relatively weaker ability to capture the individual and interactive effects of the independent variables. The *p*-value and *F*-test values indicate that the two-way interaction of beam speed and beam current and the three-way interaction of focus offset, beam speed, and beam current was not statically significant in the width variation. The remaining individual and two-way interaction of the

independent variables were found significant. Similar to melt pool depth, the percentage contribution by adjusted *SS* reveals beam speed (48.82%) has a larger contribution in leading the variance of width. The contribution ranking is then followed by beam current (27.74%) and focus offset (6.60%). The lesser *SS* contribution by focus offset contrasts with the qualitative and quantitative observations. The normal probability plot and the residual versus fits plot can explain the disagreement as slight deviations at the tail ends from normality and observed minor heteroscedasticity in the form of a wide to narrow funnel shape was observed respectively. This could possibly be attributed to the width measurement outliers such as track samples fabricated with higher beam speeds that lead to an inconsistent track with lack of fusions. The employment of a weighted regression or removal of outliers can be done in the future to address this issue.

Table 3-5 ANOVA summary for the effects of primary process parameters on the melt pool width

Variance Sources		Degrees of Freedom (dF)	Adjusted Sum of Squares (SS)	Adjusted Mean Square (MS)	F-value	P-value	F_{crit}	Percentage Contribution by SS (%)
Individual Factor	Focus Offset	2	243067	121533	21.47	0.000	3.17	6.60
	Beam Speed	2	1797519	898760	158.77	0.000	3.17	48.82
	Beam Current	2	1021131	510566	90.2	0.000	3.17	27.74
Two-way interaction	Focus Offset * Beam Speed	4	63632	16158	2.85	0.033	2.54	1.73
	Focus Offset * Beam Current	4	73123	18281	3.23	0.019	2.54	1.99
	Beam Speed* Beam Current	4	5721	1430	0.25	0.907	2.54	0.16
Three-way interaction	Focus Offset* Beam speed* Beam current	8	34117	4265	0.75	0.645	2.12	0.93
Error		51	288694	5661				
Total		77	3681618					

3.3.3 Defects

The 27 different process parameter conditions created tracks with different forms and severity of defects. An emphasis is placed in selecting a process parameter combination that is not prone to defects as accumulative stacking of a defect prone track can compromise the part quality and debilitate the part performance. In this section, OM and SEM micrographs are used to identify the various defects and their locations within the deposited melt pool. A brief discussion of the mechanisms that give rise to the identified defects are discussed. Subsequently, the degree of cracking is also quantified.

3.3.3.1 Identification of Defects in EBM Processed CM247LC

The SEM micrographs in Fig. 3-7 identifies the defects observed in the EBM deposited single-tracks of CM247LC. In Fig. 3-7a, the first type of defect is characterized by its irregular shape and an incomplete bonding appearance. This is indicative of lack of fusion defects that occur due to inconsistent melting prompted by low energy densities [8], [13], [75], [76].

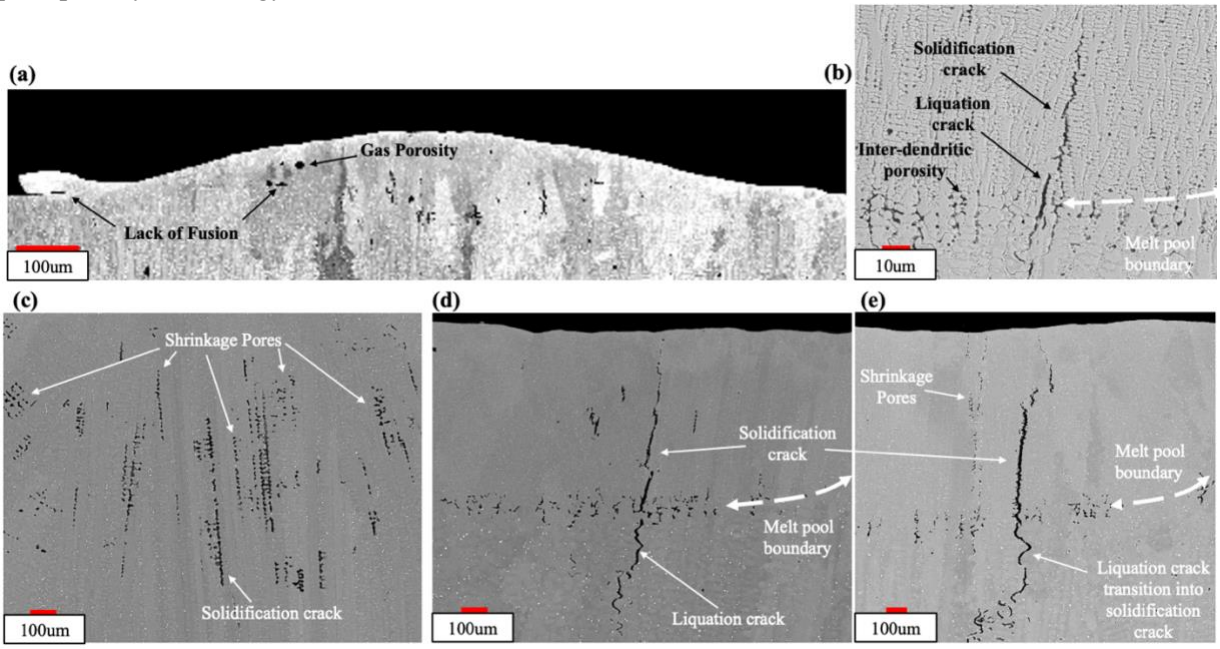


Figure 3-7. SEM micrographs for the identification of defects such as (a) lack of fusion and gas porosity at 173x, and solidification cracks, liquation cracks, inter-dendritic porosity, and shrinkage pores at (b) 1.5kx in etched condition and (c)-(e) at 1.2 kx magnification in the pre-etch condition.

The second category of defects consists of pores where further subdivisions can be made according to their location and shape. The first subdivision includes gas porosities. This can be identified in Fig. 3-7a by their spherical characteristic. This morphology may stem from the internal porosities in the initial powder particles as a result of the atomization technique used for powder production [13], [75]. These gas porosities have a tendency to be randomly distributed [13]. In addition, the process parameters fostering high solidification rates have been found to increase the presence of gas pores as it reduces the timeframe in which pores are able to coalesce and escape to the melt pool surface [75].

Another subclassification of porosity include a chain of pores aligned along the inter-dendritic zones (Figs. 3-7c, e and Figs. 3-8a, b). The formation mechanism of such shrinkage pores occurs during dendritic growth as primary dendrites grow parallel in the most favourable direction [77]. As solidification progress, secondary dendrites can also grow along the sides of primary dendrites, in a perpendicular manner to the growth of primary dendrites [77]. In the final solidification stages, the dendrites can coalesce with other dendrites and effectively shut off the metal liquid feeding into the inter-dendritic spaces [13], [77]. Within the isolated space, the remaining solidifying liquid will contract and shrink in volume [13], [77]. Due to the

insufficient liquid feeding to counterbalance the volume contraction, shrinkage pores are formed [13], [77]. This porosity has been claimed to be typical for high linear energy densities [77]. Nonetheless, there is a low concern as these shrinkage pores are commonly found in the top regions of the melt pool and can be remelted in future layers with an appropriate selection of layer thickness and melt pool.

The third subdivision include irregularly shaped pores that are restricted to along the melt pool boundary delineating the partially melted zone and fusion zone (Figs. 3-7b, d-e). These pores also occupy the inter-dendritic spaces but would not be able to be remelted in future layers. The root cause of this porosity type cannot be discerned between gas entrapment or shrinkage by volume contraction in the final phases of solidification [78]. However, this porosity is observed to be more common in wider and shallow melt pools, corresponding to higher focus offset and beam speeds.

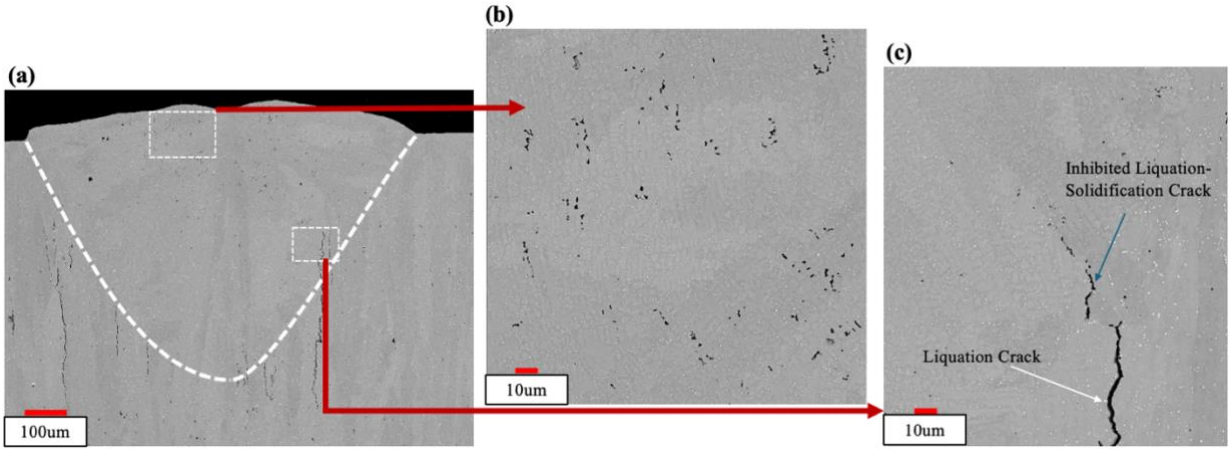


Figure 3-8. SEM micrograph providing a macro- and micro- scale view of defects at (a) 182x, (b)-(c), 1.2kx

Non-weldable nickel superalloys are prone to cracking. Consequently, this third category of defects was also observed in the cross section of the deposited tracks. The location and characteristic of the identified cracks in Figs. 3-7b-e and Figs. 3-8a,c highlights two dominant mechanisms, solidification cracking and liquation cracking. In general, both crack types involve an isolated liquid film where the source of liquid feeding is absent and excessive localized strains are experienced [79]. The former occurs in the fusion zone during the final phases of solidification [13], [50], [75], [80]. Similar to shrinkage pores, residual liquid can spread continuously along the grain boundary or inter-dendritic areas [13], [50], [75], [80]. The transition process of the liquid film into solid leads to a volumetric contraction, resulting in shrinkage strains being applied across the solidifying boundaries [13], [50], [75], [80]. Liquid feeding into the solidifying zone can compensate for the solidification strain [79]. However, the transport of liquid can be obstructed by the growing network of solidifying dendrites, potentially leading to the reduced ability or an effective shutoff of the liquid feeding benefits [79]. With solidification shrinkage compounded by the restraint associated with the mechanical properties of the surrounding bulk material, the growing rate and amount of strain sustained can lead to the tearing of the liquid film and result in a solidification crack [13], [50], [75], [80].

In contrast, liquation cracks occurs in the heat affected zone (HAZ) of the melt pool [50], [80]. A proposed mechanism follows solute or alloying elements to be concentrated along the grain boundaries within the HAZ, leading to localized area where the melting point is depressed [50], [80]. As the temperature is sufficiently elevated, the grain boundaries can partially remelt and result in the formation of a liquid film [50], [80]. Similar to solidification cracks, the liquation cracks ensue due to the experienced strain and mechanical restraint as the liquid undergoes volume contraction [50], [80]. Separately, the third porosity subclassification may also be an extension of liquation micro-cracking. It is worth highlighting that in certain cases, liquation cracks within the HAZ are seen to propagate into the fusion zone of the melt pool and transition into solidification cracks (Fig. 3-7e). However, in other cases, the propagation of liquation cracks into the fusion zone is inhibited (Fig. 3-8c). This phenomenon will be revisited in a later section.

3.3.3.2 Cracking behavior of EBM processed CM247LC

The severity of cracking was assessed through the average max crack length, average crack length and crack length density. Figs. 3-9a-b exhibit a general positive relationship between LED and the first two crack quantification outputs. The use of higher LED values generates melt pools with a greater volume and higher aspect ratio. This could imply a higher cooling and solidification rates causing a higher degree of mechanical restraint and imposed strain onto the volumetrically contracting melt pool during solidification [80]. Thus, this could lead to an increased intensity of cracking. On the other hand, a lower LED can also limit the span of the HAZ [80]. In limiting the region where liquation cracking is most susceptible to occur, the liquation cracking can be reduced [80]. These reasons could possibly help explain the lower severity of cracking are associated with lower LED values.

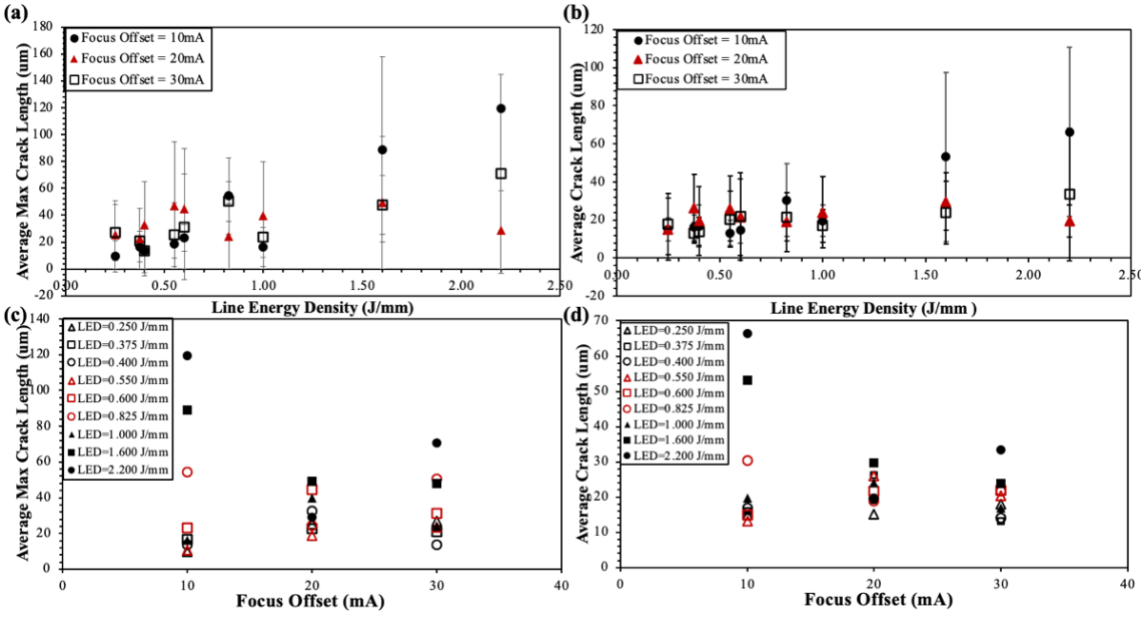


Figure 3-9. The effect of line energy density on (a) average max crack length, (b) average crack length, and the effect of focus offset on (c) average max crack length, and (d) average crack length.

As focus offset has been previously demonstrated to be an effective tool in curbing the increase in aspect ratio, Fig. 3-9c-d also highlights the ability of focus offset to minimize the window of observed crack lengths. However, Fig. 3-9c-d also displays an expansion in the crack length window at the 30 mA focus offset value relative to the 20 mA focus offset. This can possibly be attributed to the larger widths facilitated by a 30mA focus offset. As oppose to a greater volume along the depth axis by a more focused beam, a defocus beam translates greater volume to be melted along the width axis and thereby still facilitates a similar increase in the restraint experienced [81].

Fig. 3-10 studies the influence of the melt pool morphology on the severity of cracking through crack length density. The melt pools exhibiting a keyhole melt mode are isolated on the right side of the graphical plot. In the subsequent comparison, the two datapoints are excluded and sole focus is placed on the remaining melt pools achieved by a conduction melt mode. The dashed reference lines illustrate a weak negative correlation between aspect ratio and the resulting crack length density for the sample set of focus offset 20 mA and 30 mA. A slight offset distance separates the two data groups from one another. The weak trend of both sample sets seemingly indicates an optimal melt pool aspect ratio for the given beam defocus and gaussian energy profile.

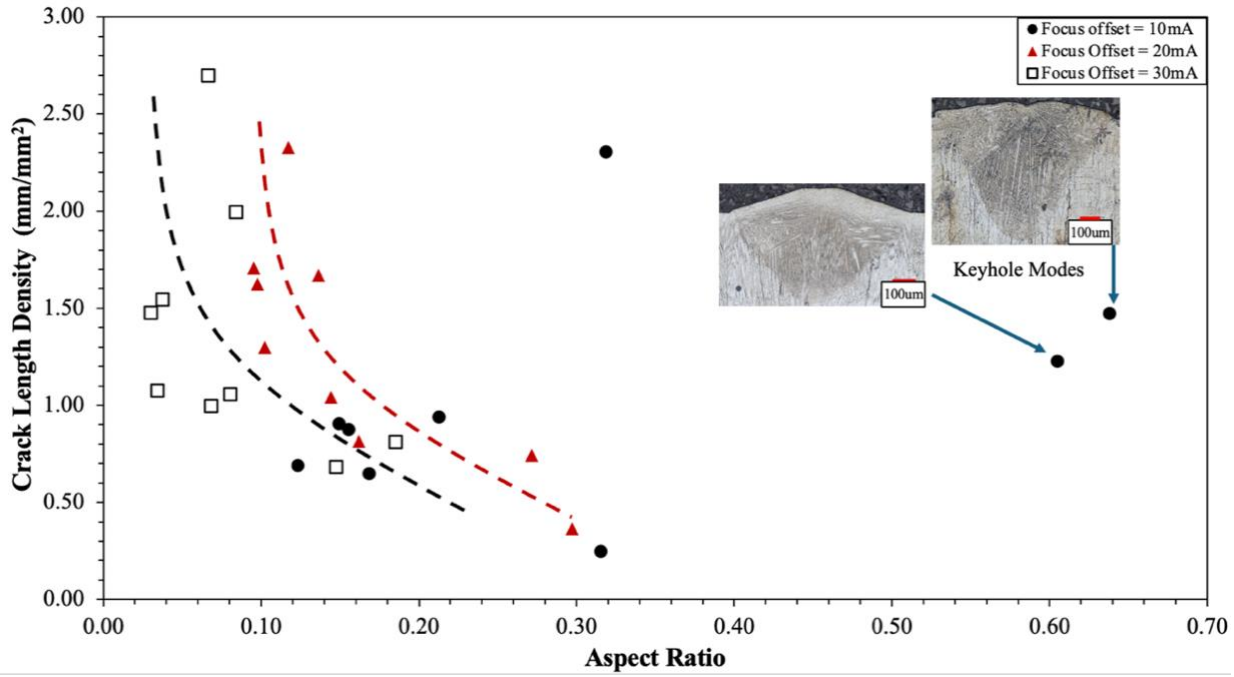


Figure 3-10. Crack length density as a function of melt pool aspect ratio. Note, the purpose of the dashed lines is to serve as reference lines and not a line of best fit.

Two process parameter combination exhibited a significantly lower susceptibility towards cracking as reflected by the minimized crack length density. The first parameter combination corresponds to a focus offset, beam current and beam speed values of 10 mA, 5 mA, and 300 mm/s while the second parameter combination possessed values of 20 mA, 11 mA, and 300 mm/s in the same order. The associated crack length densities are 0.25 mm/mm^2 and 0.36 mm/mm^2 respectively. In addition, both combinations had a resulting melt pool aspect ratio within the vicinity of ~0.3. This indicates it is desirable to have a reasonably wide melt pool with a moderately shallow penetration melt depth. Fig. 3-11 depicts the cross section in the pre-etch and etch condition for the former process parameter combination that had shown the lowest cracking severity.

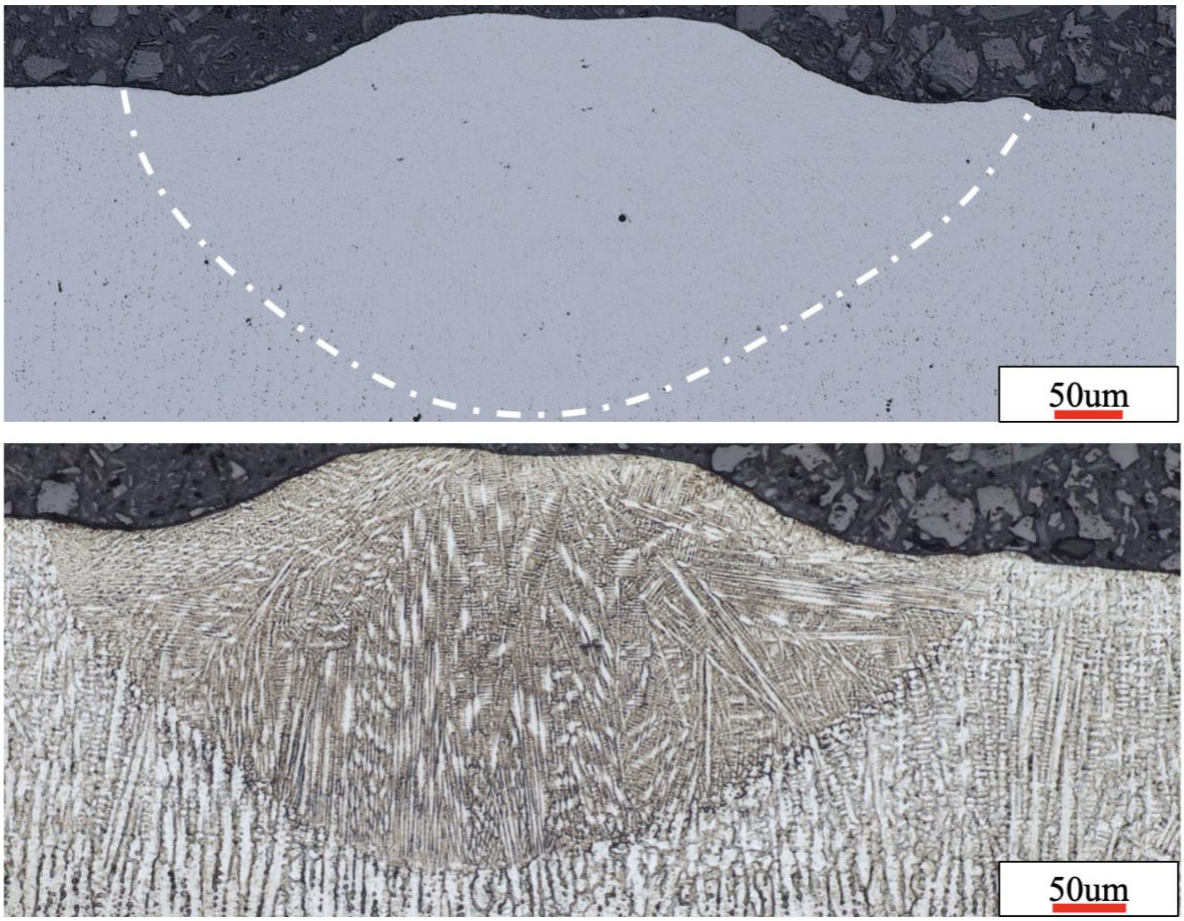


Figure 3-11. Melt pools in the (a) pre-etch and (b) etch condition for process parameter combination of focus offset = 10 mA, beam current = 5 mA, and beam speed = 1200mm/s

3.3.4 Microstructure

3.3.4.1 Microstructure - Gamma Prime

The γ' precipitate is a key microstructural feature of non-weldable nickel superalloys that merits discussion. The SEM micrographs in Fig. 3-12 visually depicts the microstructural evolution of the fabricated part ranging from the single-track body (a) and the top (b), middle (c) and bottom section (d) of the substrate. Based on this qualitative comparison, an observed microstructural gradient in relation to the γ' is evident. In the single-track body, no γ' precipitate is evident. However, in the top section of the substrate, several sporadic clusters of very fine γ' precipitates are visible. At the middle and bottom section of the substrate, sub-micron spherical γ' precipitates with a uniform distribution are observed to predominantly cover the majority of the image area, with the bottom section displaying an increase in γ' precipitate size.

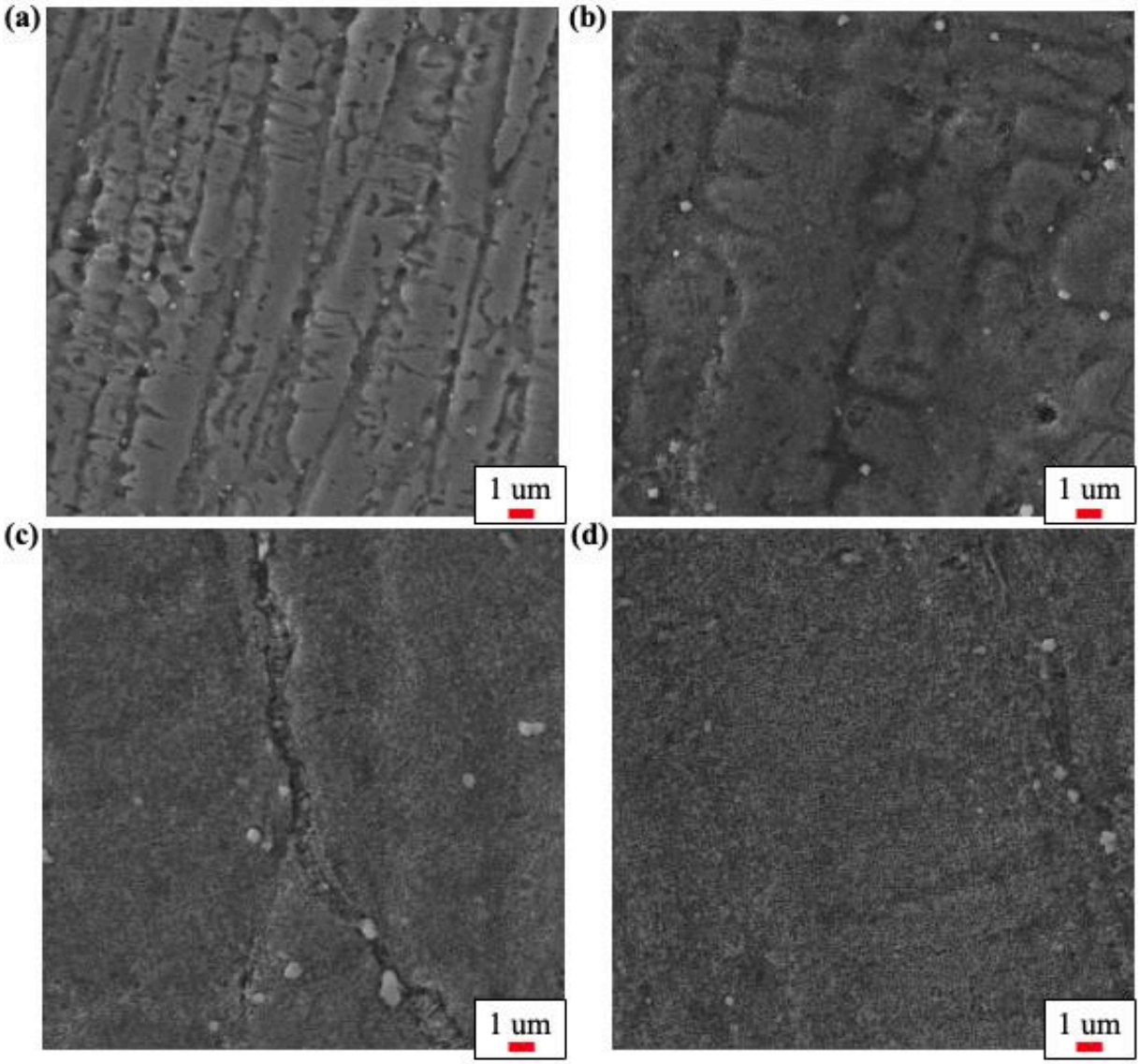


Figure 3-12. SEM micrographs reveal microstructural gradient from (a) the single-track body, (b) few layers below the top surface of substrate, (c) middle of substrate, and (d) bottom of the substrate.

The precipitation and development of the γ' microstructure requires a temperature range lower than the γ' solvus temperature and a sufficiently low cooling rate since a high cooling rate leads to the kinetic suppression of the γ' precipitation [52], [82]. As the final melt layer, the solidification of the single-track body would have too high of a cooling rate to foster the precipitation of γ' [52], [82]. Hence, Fig. 3-12a concurs with the expectation of a lack of γ' found in this region [52], [82]. For the earlier deposited layers, these layers would have undergone an in-situ heat treatment stemming from the high temperature powder bed by a high temperature preheat and vacuum conditions [52], [82]. Moreover, with each subsequent layer, the in-situ heat treatment temperature is higher and treatment time decreases [52], [82]. This explains the smaller and more sporadically distributed γ' near the top of the substrate (Fig. 3-12b) while the middle (Fig. 3-12c) and the bottom (Fig. 3-12d) of the substrate showed an increasing γ' size and homogenous distribution at a lower layer level [52], [82]. This microstructure gradient highlights the build height driven variations in layer thermal history, and thus its role in the precipitation and growth behavior of γ' [52], [48]. Due to the lack of γ' in the single-track, no further characterization was done.

3.3.4.2 Microstructure – Grain Structure

The melt pool morphology can have an impact on the solidification conditions within the melt pool and in turn can influence the resulting grain microstructure and crystallographic texture [10], [83], [84] , [85]. Fig. 3-13 displays a comparison of EBSD grain maps while Fig. 3-14 displays a comparison of IPF map along the y axis, parallel to the build direction. A critical misorientation angle (θ) was defined to be 15°. For the low LED level, instead of the single-track with a LED level of 0.400 J/mm, the single-track associated with 0.550 J/mm was used for the 30 mA focus offset group since tracks of lower LED levels were not suitable for comparison due to their discontinuity and poor stability stemming from a lack of fusion.

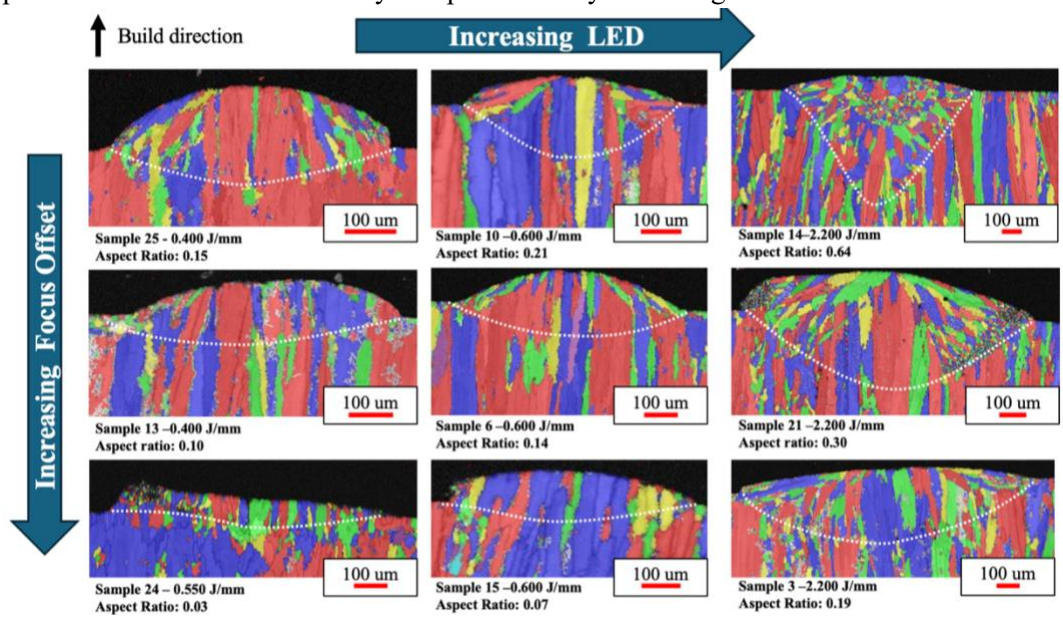


Figure 3-13. EBSD grain mapping of EBM deposited CM247LC single-track

Within the melt pool, EBSD grain maps (Fig. 3-13) and IPF Y maps (Fig. 3-14) reveal grain development predominantly proceeds via epitaxial growth. From theoretical welding knowledge, this mechanism occurs when molten liquid, derived from the melting of powder particles, completely spreads along the substrate marked by the melt pool boundary [84]. This process reduces the energy barrier for the nucleation and enables the continual growth of the same grain and crystallographic orientation found in the preceding layers at the melt pool boundary [84], [85]. Fig. 3-13 demonstrates most of the grains follow a columnar grain morphology. This morphological type is reflective of a directional solidification driven by heat flux in a single direction, proceeding from a region of high temperature to a lower temperature region [83]. In the higher LED samples, the peripheral sides of the inner melt pool boundary are observed to possess a mix of fine columnar grains and equiaxial grains. Equiaxial grains can also be found in two separate occasions. The first can be seen in top left side of the melt pool in samples 21 and 24 where spatter is found to fuse with the melt pool. This was confirmed with OM images of the melt pool in the etched condition. On the other hand, sample 14 exhibits a cluster of equiaxed grains located in top center region of the melt pool. Homogenous nucleation could be used to elucidate its occurrence [86]. However, the most probable explanation is the onset of dynamic nucleation via dendrite/grain fragmentation mechanism where the convective flow of the transient melt pool facilitates the detachment of grains or dendrites. The surfaces of these detached grains or dendrites can serve as nucleation sites for the equiaxed grains [83], [84], [86]. Separately, in the case of low aspect ratio where the melt pool possesses a large width but shallow depth, the grain growth is physically restricted as indicated by the minimized elongation of the columnar grains.

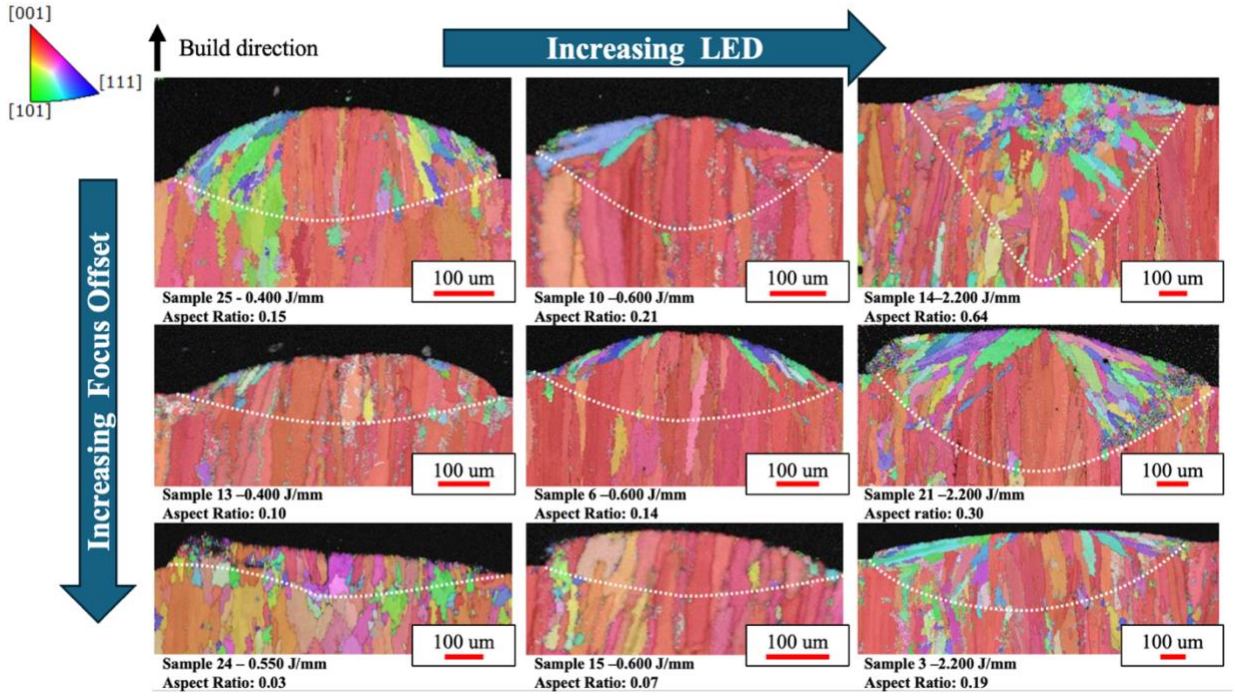


Figure 3-14. EBSD IPF Y maps of EBM deposited CM247LC single-track

Proceeding after nucleation, the grain growth stage is significant in the development of crystallographic texture. The orientation of the columnar grain growth has the tendency to proceed perpendicularly from the melt pool boundary in order to align itself with the vector of the maximum temperature gradient [84], [85]. However, grain growth is also dictated by its preferred crystallographic orientation where for the case of face centered cubic (FCC) metals such as nickel superalloys, the "easy growth" direction is in the <100> orientation, parallel to the build direction [80], [84]. These two stated conditions can be observed in Fig. 3-14, with the preferential <100> orientation indicated by the red color. In the case of low aspect ratios, the near flat melt pool boundary enables the perpendicular direction of the melt pool boundary to be vertically aligned with the build direction. Therefore, a low misorientation between the thermal gradient vector and the easy growth direction is fostered. This agreement of the two conditions results in Samples 6, 13, and 15 to display melt pools with a predominantly <100> texture. For the case of higher aspect ratios, the proportion of the center melt pool boundary, where the perpendicular direction of the boundary aligns to the vertical build direction, becomes progressively small. As a result, the fraction of grains with <100> orientation is effectively reduced. Alongside, as the aspect ratio of the melt pool evolves, the peripheral walls of the melt pool boundary become more steeply angled, resulting in a large misorientation between the vector of the maximum thermal gradient and the <100> easy growth direction. Thereby, the two conditions act in opposition with one another at the peripheral side walls and give rise to competitive grain growth, facilitating a higher amount of finer grain structures that nucleate and grow with varying preferred growth orientations along the melt pool boundary as seen in Sample 3, 14, and 21 [54], [87].

The focus offset correlates to the resulting beam sharpness and energy distribution. Its influence on the crystallographic texture of a deposited melt pool can be observed. This trend is best observed as one keeps LED constant and move vertically upward along a EBSD map column in Fig. 3-14. A high focus offset has been previously seen to exhibit a less intense electron beam where the gaussian energy curve is more broadly and uniformly distributed [30]. The resultant low thermal gradient thereby restricts grain competition and enables a weaker <100> texture as most prominently shown by samples 15 and 24. As focus offset decreases, implying the intensity of the beam increases and the electron energy distribution become much steeper, a larger thermal gradient is fostered. This results in a greater proportion of columnar grains to grow and orient along the <100> direction. The stronger <100> texture is seen in the melt pools of samples 13, 6, and 10. However, in the extreme of a highly intense and focused beam, the combination of a strong thermal gradient and greater melt pool boundary curvature from a higher aspect ratio facilitates the growth condition of grain alignment towards the thermal gradient to become more dominant. As such, the increase presence of misoriented grains and a weaken <100> texture is evident (Sample 25).

On the other hand, at constant focus offset or a fixed focal point, as one moves laterally from the left to the right of Fig. 3-14, it might be argued that the influence of LED follows a similar trend on crystallographic texture. Where the increase of LED, by example of current increase, facilitates a greater central concentration of energy within the electron beam, and results in a stronger thermal gradient and eventually a greater misorientation. However, the influence of LED on crystallographic texture is more complicated to decipher as the secondary process parameter of LED is the ratio of primary process parameters involving beam current and beam speed. For instance, a high thermal gradient could also be fostered by the use of high beam speeds that leads to a melt pool of low depth and width [4]. Therefore, further investigation such as through modelling would be needed in order to provide a better insight on the heat input by the beam and extraction towards surrounding solid volume in order to entangle the influence of print process parameters on solidification parameters of thermal gradient, and in turn the crystallographic texture.

The grain structure can also be correlated to the previously discussed cracking behavior. For instance, in sample 24, solidification crack occurs at a high angle grain boundary (HAGB) (e.g. $\theta > 15°$) along the centerline of the melt pool. In addition, a similar HAGB case is observed for the location of liquation cracking in sample 14. HAGBs are associated with high grain boundary energy that can preserve the liquid film and its stability at lower temperatures [17]. Thereby, HAGBs are considered susceptible sites for crack initiation and propagation [17]. With this in mind, to minimize the susceptibility of cracking, it would be desirable to limit the amount of HAGBs. This implies avoiding the use of melt pools with a significantly high aspect ratio. This was as previously seen by steep peripheral boundaries fostering greater competitive growth of misoriented grains due to competing orientation growth factors.

A degree of propagation has been observed where liquation tracks in the HAZ are able to transition into solidification cracks in the fusion zone. However, in some cases such as the high LED samples of 3, 14 (Fig. 3-8c), and 21, the propagation of liquation cracks is observed to be inhibited. As seen by samples of higher LED in Fig. 3-13, this inhibition can be credited to the finer grain structures aligned along the peripheral sides of the melt pool boundary. The grains, with a lower aspect ratio in the crack vicinity, allows for the strain to be better distributed along a larger number of grain interface and boundaries, and thereby reduces the localized stress [17]. This mechanism can serve as another effective manner to lower the degree of cracking.

3.4 Summary

A single-track experiment, designed using a 3^3 full factorial DoE format was performed to study the relationship among primary print parameters, melt pool morphology, and cracking behavior of EBM-processed CM247LC. The primary print parameters studied were the beam current, beam scanning speed, and focus offset. In addition, the track quality and microstructure were concurrently investigated to determine the dependability of the deposited track and provide further insights on the cracking behavior. From the analysis conducted, a summary of the findings is listed as follows:

- A process parameter window was established for track quality. Higher LED parameters created a continuous and uniform tracks whereas the track stability was compromised with higher beam speeds.
- LED exhibited a positive correlation with the melt pool width, depth, and aspect ratio. Statistical analysis revealed that individual primary process parameters were the major sources of variance for melt pool width and depth, with beam speed exerting having the largest contribution.
- Solidification and liquation cracking were identified as the primary crack mechanisms in single-track deposition.
- Crack length density revealed a weak correlation between cracking and melt pool aspect ratio. A moderately wide and shallow melt pool was preferred for minimal cracking. With the lowest crack length density of 0.25 mm/mm^2, observed at an aspect ratio of 0.32, and achieved with a focus offset, beam current, and beam scan speed values of 10mA, 5mA, and 300mm/s, respectively.
- Cracks dominantly formed at high angle grain boundaries. Minimizing misoriented grains, by the avoidance of high-aspect ratio melt pools, or low energy input process parameters that induce a weak thermal gradient, is desirable. Additionally, liquation crack propagation across the melt pool boundary was inhibited by with finer aspect ratio grains at the boundary.

Chapter 4. Finite Element Modelling of EBM deposited Single Tracks

4.1 Introduction

Electron Beam Melting (EBM) is a complex additive manufacturing technology where the localized solidification process at the micro-scale involves the inter-play of several physical phenomenon such as but not limited to heat transfer, changes in material phase, and fluid dynamics [27], [53], [54]. With the various user-defined process parameters incorporated within the software system of the technology, a trial-and-error approach to reach a desired part and objective may be achieved at the expense of significant resources and time [65]. In spite of the possible success, there still persists the lack of direct understanding of the spatial-temporal evolution of thermal energy during the solidification process. The most straightforward solution would be the utilization of an in-situ monitoring system. However, the limited maturity of the technology due to its recent and controlled emergence on the market and the design and internal conditions of the build chamber, such as the high temperature conditions and shielding to prevent metallization and x-ray leaks, complicates the incorporation of such an in-situ monitoring system [88].

As an alternative solution, the use of numerical models can be beneficial for the comprehension of the local solidification conditions. In EBM, the finite element method (FEM) is one of the more studied numerical approaches due to its dependability and efficiency [27], [62], [89]. Zäh and Lutzmann [90] used a combination of FEM and a defined laser powder bed fusion condition of a 2:1 melt pool length to width ratio to reduce the chance of Plateau Rayleigh instability and balling. Thus, a process window was defined to identify suitable process parameter combinations that maintains the stability of the melt pool [90]. The applicability of the model was verified with the successful production of parts devoid of balling [90]. Ding et al. [29] employed a heat transfer model with a Gaussian surface heat source to simulate single-track experiments and extracted the corresponding thermal variables of thermal gradient (G), cooling rate (G*R), and solidification rate (R) to predict the microstructure via a solidification/cooling map (G and R plot).

This chapter focuses on the development of a thermal model by FEM to gain insights on the local solidification and cooling conditions of the deposited single-tracks discussed in Chapter 3. The desired thermal information includes the thermal history, temperature gradient, and cooling rate of the solidifying melt pool. The extracted thermal variables are correlated to the beam current, beam speed, and focus offset to better understand the effect of process parameters on heat transfer during printing. In addition, the model is used to explore the link between local thermal conditions, melt pool morphology and the inherent cracking tendencies. The thermal model will be calibrated with the experimental melt pool width and depths of the single-tracks to assess the reliability of the developed model.

4.2 Model Setup

The 3D thermal simulation of the EBM deposited CM247LC single-tracks studied in Chapter 3 was performed on COMSOL 6.1 Multiphysics® to extract the corresponding thermal profiles and desired thermal variables. The powder layer is treated as a continuum instead of individualistic particles. The geometrical domain of the model consists of two stacked rectangular prisms, representing the powder layer and bulk substrate domain. The top powder layer was of the dimensions 2000 × 2000 × 70 µm while the bottom bulk substrate domain had the dimensions of 2000 × 2000 × 2000 µm. The simulation powder layer matches with the user defined layer thickness of 70 µm. However, the effective layer thickness may be larger due to potential powder consolidation occurring during the spreading within the actual deposition [58]. On a separate note, the employed geometrical domain should be sufficiently large in comparison to the melt pool sizes such that the boundary conditions should not influence the simulated results. The FEM simulation was performed on an AMD Ryzen 5 3600X 6-core Processor.

4.2.1 Governing Equations and Boundary Conditions

The three dimensional phenomenon is governed by the Fourier's law of heat conduction (Eq. 4-1):

$$\rho C_p \frac{\partial T}{\partial t} - \left[\frac{\partial}{\partial x}\left(k_x \frac{\partial T}{\partial x}\right) + \frac{\partial}{\partial y}\left(k_y \frac{\partial T}{\partial y}\right) + \frac{\partial}{\partial z}\left(k_z \frac{\partial T}{\partial z}\right)\right] = Q(x, y, z, t) \tag{4-1}$$

where ρ is the density of the given material $\left[\frac{kg}{m^3}\right]$, C_p is the specific heat capacity $\left[\frac{J}{kg \cdot K}\right]$, t is the time $[s]$, $k_{x,y,z}$ is the thermal conductivity along the x, y, and z directional axis $\left[\frac{J}{kg \cdot K}\right]$, T is the temperature $[K]$, and Q is the applied volumetric heat source within the simulation representing the electron beam $\left[\frac{W}{m^3}\right]$.

Following the preheating stage of the powder layer during the EBM fabrication process, the initial temperature condition of the entire geometrical domain was set at 1000°C. The boundary conditions applied describes the radiative and convective heat lost during the deposition process. The radiative heat lost, q_r is applied on the top surface boundary of the powder layer and is described by (Eqn. 4-2):

$$q_r = \epsilon\sigma(T_a^4 - T^4) \tag{4-2}$$

where ϵ is the emissivity of the material, σ is the Stefan Boltzmann constant $\left[\frac{W}{m^2 \cdot K^4}\right]$, and T_a denotes the ambient temperature that is taken to be 293.15 K. The convective heat lost, q_c is applied to the powder layer and is described by (Eqn. 4-3):

$$q_c = -h_c(T_a^4 - T^4) \tag{4-3}$$

where h_c denotes the convective heat transfer coefficient $\left[\frac{W}{m^2 \cdot K}\right]$. It should be highlighted that due to high vacuum conditions, the convective heat lost contribution is often treated as negligible in EBM [28]. For such reason, the current simulation excludes this mechanism of heat lost in the heat transfer analysis.

Two other boundary conditions were also concurrently employed during the simulation setup. First, a temperature boundary condition was applied where the bottom surface boundary of the bulk substrate domain was held at the constant preheat temperature. The second boundary condition involved the adiabatic or thermal insulation condition applied across the vertical boundary surfaces of the geometrical domain. The near zero heat flux condition across the vertical boundary surfaces is a reasonable assumption since the surrounding powder bed has a characteristically low thermal conductance given the limited contact surface amongst powder particles [91].

4.2.2 Heat source model

The energy supplied by the electron beam can be represented by the Goldak double ellipsoidal heat source model [92]. The selection of this volumetric heat source model is based on its wide acceptance and common employment in the numerical modelling of the EBM process [62], [28], [93]. The heat source follows a Gaussian energy distribution, and its volume is sectioned into a front and rear segment as described by the following expression (Eqn. 4-4) with the y-axis as the scanning direction of the beam [92]:

$$Q(x,y,z,t) = \begin{cases} \frac{6\sqrt{3}f_f\eta IU}{a\cdot b\cdot c_f\pi\sqrt{\pi}} \exp\left[-3\left(\frac{x^2}{a^2}+\frac{(y-vt)^2}{c_f^2}+\frac{z^2}{b^2}\right)\right], & y \geq 0 \\ \frac{6\sqrt{3}f_r\eta IU}{a\cdot b\cdot c_r\pi\sqrt{\pi}} \exp\left[-3\left(\frac{x^2}{a^2}+\frac{(y-vt)^2}{c_r^2}+\frac{z^2}{b^2}\right)\right], & y < 0 \end{cases} \quad (4\text{-}4)$$

where I is the beam current [A], U is the accelerating voltage [V], η is the energy absorption efficiency of the electron beam, and v is the electron beam scanning speed [m/s]. The variables of a, b, and $c_{f,r}$ are the semi-axes for the given volumetric ellipsoid and can be considered as the geometrical dimensions of the heat source defined along the local coordinate axis of x, z, and y respectively. The subscripts f and r are descriptors denoting the definition for the front and rear segments of the heat source respectively. The f_f and f_r parameters are the fractional factors defining the proportion of the thermal energy assigned to the front and rear segments. In order to ensure continuity between the front and rear segments, f_f, f_r, c_f, and c_r must satisfy the three conditions listed below (Eqn. 4-5, 4-6, 4-7) [94]:

$$f_f = \frac{2*c_f}{c_f+c_r} \quad (4\text{-}5)$$

$$f_r = \frac{2*c_r}{c_f+c_r} \quad (4\text{-}6)$$

$$f_f + f_r = 2 \quad (4\text{-}7)$$

4.2.3 Material Properties

With CM247LC as the focus of the study, the powder phase and bulk substrate phase were assigned two separate material properties when they are first below the melting temperature. Most of the material properties were extracted from published literature regarding CM247LC. Certain incorporated material

properties involved a temperature dependency and are exhibited in Fig. 4-1. The temperature dependent properties are hereafter discussed.

The solid bulk density (ρ_{solid}) was found from preceding initial characterization work to be equivalent to 8460 kg/m^3. The powder density (ρ_{powder}) $\left[\frac{kg}{m^3}\right]$ can be expressed by the following expression (Eqn. 4-8):

$$\rho_{powder} = (1 - \varphi)\rho_{solid} \tag{4-8}$$

where φ is the porosity and the bracket term can be considered as the packing density of the powder. Assuming that the powder particles are spherical in morphology and follows a BCC packing configuration, the porosity can be taken to be 0.32 and the packing density to be 68% [65]. This assumption is valid as previous powder characterization work found the final bulk density to be 5530 kg/m^3. This is equivalent to a packing density of 65%. The simplification is adopted to help determine a separate material property discussed later. The temperature dependent density of the material during the mushy and liquid phase were calculated from the following two expressions derived from least square regression (Eqn. 4-9) [95], [96]:

$$\rho(T) = \begin{cases} 1000 * [7.54 - (1.9 \times 10^{-3})(T - 1612)], & 1612\ \text{K} < T < 1647\ \text{K (mushy phase)} \\ 1000 * [7.47 - (1.6 \times 10^{-3})(T - 1647)], & 1647\ \text{K} < T < 1823\ \text{K (liquid phase)} \end{cases} \tag{4-9}$$

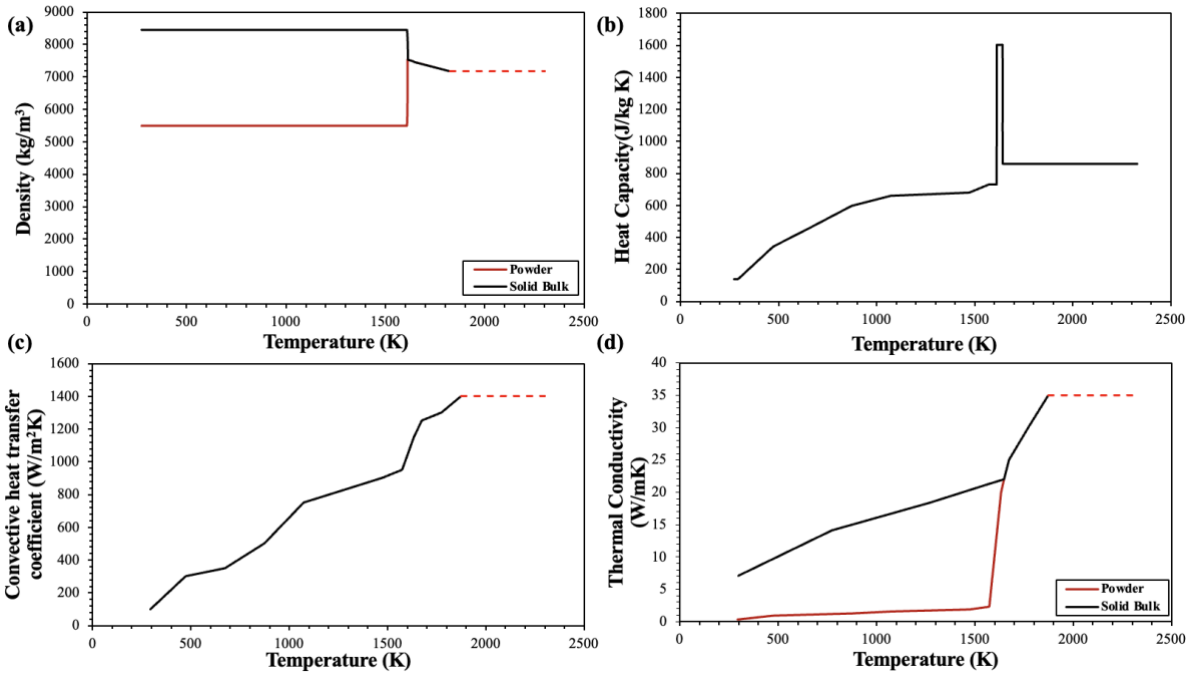


Figure 4-1. Temperature dependency of the following material properties for CM247LC: (a) density, (b) heat capacity, (c) convective heat transfer coefficient, (d) thermal conductivity

The heat capacity of the solid bulk substrate and powder are assumed to be the same. The thermal data regarding heat capacity and the convective heat transfer coefficient were extracted from Wang et al [15]. Within the solidus and liquidus temperature domain, the apparent heat capacity method is employed to

account for the phase change through the inclusion of the latent heat of fusion [97], [98] [99]. Above the liquidus temperature, the thermal variable assumes a constant value corresponding to the specific heat of CM247LC in the liquid phase. The following expressions for specific heat capacity associated with the solid [15], phase change [97], [99], and liquid temperature range [100] are listed as follows (Eqn. 4-10):

$$C_p(T) = \begin{cases} C_{P,sensible} & , T < T_S \\ C_{p,modified} = C_{p,sensible} + \frac{L_{fus}}{T_L - T_s} & , T_s < T \leq T_L \\ C_p, sensible & , T > T_L \end{cases} \quad \text{(Eqn 4-10)}$$

where L_{fus} is the latent heat of fusion $\left[\frac{kJ}{kg}\right]$, and T_L and T_S are the liquidus and solidus temperature.

The simulation model uses thermal conductivity values from Wang et al. [15] where the data for the powder phase was derived through Sih and Barlow model [101] for temperatures below the solidus temperature, and a derived experimental formula by Shen et al. [102] for temperatures between the solidus and liquidus temperature respectively. For temperatures above the liquidus temperature, a constant value associated with the thermal conductivity of liquid was assumed [15], [100]. The thermal conductivity of the solid bulk was found by preceding work using NETZSCH flash method.

The approximation of the emissivity of powder (ε_{powder}) was derived by using the bulk material emissivity (ε_{bulk}) [103] and an extension of Sih and Barlow model [104] as conducted by Galati et al. [65]. In the original model, the powder bed emissivity is dependent on the emissivity of the powder particles, emissivity of the holes ε_H, and the packing arrangement of the powder bed. Galati et al. [65] specified the model for a BCC packing arrangement and was able to determine the appropriate radius of a BCC hole (r_{BCC}), proportion of surface area occupied by BCC holes (A_H), and the proportion of the total cavity surface sectioned away by the radiating hole (f) [104]. The further details on the formulation can be found in Galati et al. [65] and the two main expressions directly relating to emissivity are listed as follows (Eqn. 4-11, 4-12):

$$\varepsilon_{powder} = A_H \varepsilon_H + (1 - A_H)\varepsilon_{bulk} \quad (4\text{-}11)$$

$$\varepsilon_{hole} = \frac{\varepsilon_{bulk}}{\varepsilon_{bulk} + f(1 - \varepsilon_{bulk})} \quad (4\text{-}12)$$

where A_H was found to be 0.53 while f was equal to 0.25. The remaining material properties and model variables assuming a constant value are listed in Table 4-1. The solidus, melting and liquidus temperature were found by previous differential scanning calorimetry work done in the separate initial characterization of the alloy material.

Table 4-1. Defined constants utilized in the thermal FEM simulation

Model Variable	Symbol	Value
Solidus Temperature [K]	T_S	1613
Melting Temperature[K]	T_M	1628
Liquidus temperature [K]	T_L	1643
Vaporization Temperature [K] [100]	T_V	3300
Latent Heat of Fusion [kJ/kg]	L_{fus}	264
Emissivity of bulk substrate [103]	ε_{bulk}	0.16
Emissivity of powder	ε_{powder}	0.30
Coefficient of thermal expansion [K^{-1}] [48]	h_c	1.82 x 10^{-5}
Electron beam energy absorption efficiency	η	0.90
Accelerating Voltage [V]	U	60000

In the definition of material properties, the COMSOL variable function type of state variables were utilized to specify the powder phase and the solid bulk substrate with a temperature dependency. In elaboration of state variable function, elements in the powder phase domain are initially assigned the powder material properties. However, after exposure to the traversing heat source and upon reaching the melting temperature condition where the powder phase undergoes a phase change into a liquid ($T > T_m$), the state variable triggers the permanent switch from the powder material properties to the adoption of material properties corresponding to the solid bulk. As cooling occurs, the material properties of the solid bulk dictate the future simulation efforts of the heat transfer study. The state variable is updated before each simulation step.

4.2.4. Mesh Description

Two different tetrahedral mesh schemes were used for the geometrical model domain. These are displayed in Fig. 4-2. For the focus offset of 10mA and 20mA data subset (Fig. 4-2a), a hybrid mesh size was applied. The bulk domain layer employed a coarser mesh size of 0.2 mm while the top powder layer utilized a mesh size of 0.1 mm. Additionally, mesh refinement was employed for regions where z > 1.4 mm. This resulted in a total of 351720 domain elements, 14190 boundary elements, and 444 edge elements. For the focus offset of 30mA, a uniform mesh scheme of 0.10 mm with a single mesh refinement step was applied for both the powder and bulk domain. The completed mesh comprised of 1100768 domain elements, 27472 boundary elements, and 648 edge elements. The finer mesh size would allow for a more accurate result.

The simulation time for each simulation to reach completion was defined as the time in which the center region of the deposited track (e.g. y = 1mm) undergoes complete solidification such that the temperature falls below the melting temperature of CM247LC. The times for each simulation trial to reach completion

in real time are displayed in Fig. 4-2c and d. For a given LED level, although the real time completion was shorter for the case of 10 and 20 mA focus offset simulation trials in contrast to focus offset 30mA due to the different mesh schemes, the simulation time of the deposition process was longer for the former. This was attributed to the dimensional parameters of the heat source that will be discussed in the next section.

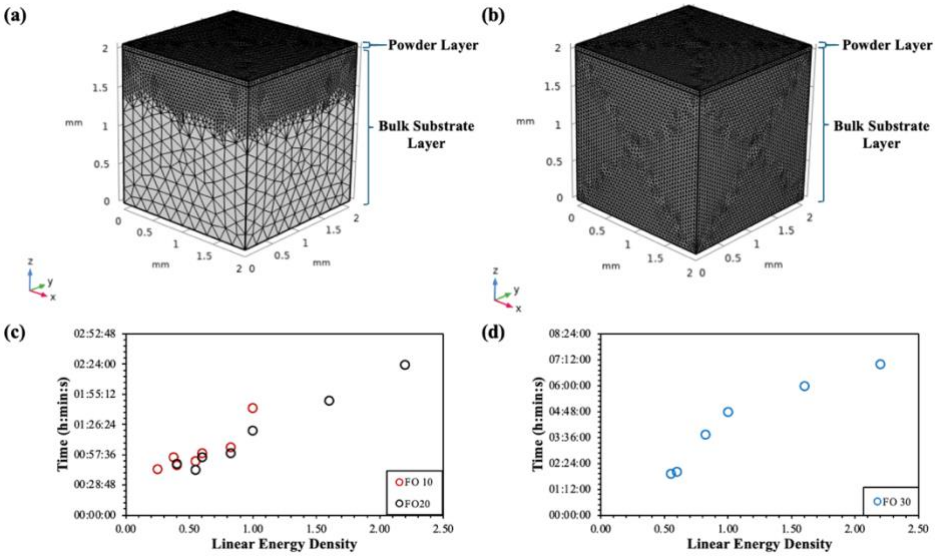


Figure 4-2. Simulation details: (a) hybrid tetrahedral mesh scheme for the focus offset 10 and 20 mA data subset and (b) uniform tetrahedral mesh scheme for focus offset of 30 mA; (c) simulation time for focus offset 10 and 20 mA data subset, (d) simulation time for focus offset 30 mA

A mesh sensitivity study was separately done to assess the dependability of the results. Additionally, the analysis helped to balance the resulting accuracy with the computational efforts and the required time for the simulation to reach completion. This assessment was done with uniform mesh sizes and the focus offset 30 mA data subset. A mesh size of 0.15 mm, 0.10 mm, and 0.085 mm was utilized in conjunction with a consecutively applied single mesh refinement step. This involved 329888, 1100768, and 1800592 domain elements respectively. Fig. 4-3 displays the mesh sensitivity analysis efforts through (a) maximum surface temperature measurements and (b) the required simulation time as a function of mesh size. Evidently, the mesh size of 0.10 mm shows a reasonable accuracy can be attained with an appropriate simulation time.

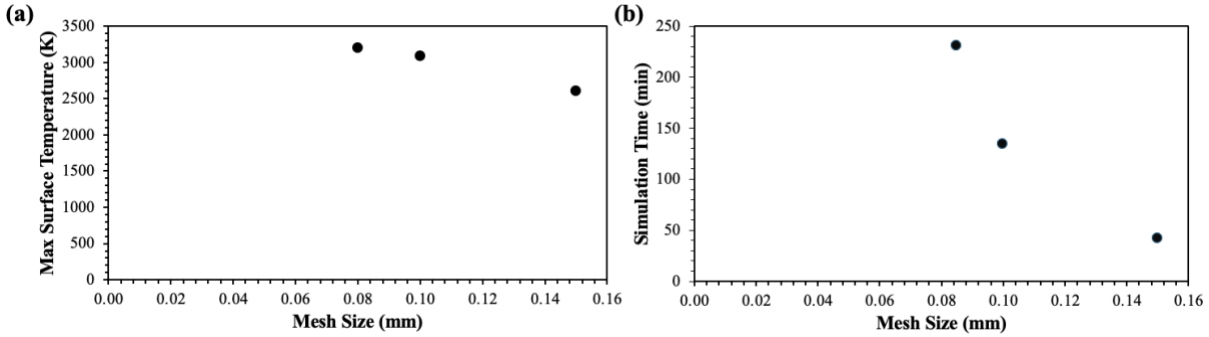


Figure 4-3. Mesh sensitivity analysis by (a) maximum surface temperature and (b) simulation time as done with uniform mesh sizes and parameter set of focus offset 30 mA, I = 8 mA, and v = 800 mm/s

4.3 Results and Discussion

4.3.1 Calibration of the Model

The experimental data was subdivided based on the level of beam focus. The thermal FEM model was calibrated for each group by the minimization of percentage error between the simulation and experimental melt pool width and depth dimensions. The experimental single-track melt pools are in reference to the work done in Chapter 3. Certain parameter combinations were excluded in the calibration and simulation for one of two reasons. The first reason is if the melt pool follows a keyhole melt mode (e.g. Focus offset 10 mA: 11 mA and 300 mm/s, and 8 mA and 300 mm/s) where heat conduction is not the main mechanism during the melt process [73], [74]. The second reason is if a low LED parameter combination yielded a track quality with a significant degree of lack of fusion. This is because experimental results with a high possible deviation can erroneously skew the percentage error of the model and make it difficult for calibration. The simulated melt pool dimensions were demarcated based on the condition if the temperature exceeds the melting temperature of CM247LC. It is worth mentioning that the powder layer was not considered in the melt pool measurements.

The calibration involved the manual adjustment of the parameters used to define the Goldak double ellipsoid heat source model. The final values are listed for each focus offset group in Table 4-2. The latter also lists the average width and depth percentage error for each focus offset group which were all found to be below 16 %. For the overall model, the average error was ~10%. The error can stem from the lack of consideration for the ongoing fluid dynamic phenomena within the melt pool. Regardless, the model has an acceptable percentage error given the broad morphological variety of the experimental melt pool. The dimensional parameters reveal with an increase in focus offset, i.e. more defocused beam, the beam width and depth are increased. Moreover, the proportion of energy allocated to the front and rear segment becomes more symmetrical with a greater focus offset. The larger beam length segments in focus offset 10mA and 20mA extends the melt pool lifetime and the required simulation run time.

Fig. 4-4 illustrates the performance of the thermal FEM model through a comparison of the experimental and simulation results for melt pool depth and width. The process parameter combination without an associated simulated result can be observed by the lack of red square label vertically aligned with a black circle label denoting an experimental data point. Both experimental and simulation results show an agreement in the positive trend between linear energy density and both measured dimensions of the melt pool. As linear energy density increases, the melt pool width and depth are correspondingly increased.

Table 4-2. Calibration results: heat source model parameters and simulation error

Variable	Focus Offset 10 mA	Focus Offset 20 mA	Focus Offset 30 mA
Beam Width [um], a	400.0	600.0	900.0
Beam Depth [um], b	110.0	130.0	170.0
Beam Length of Front Segment [um], c_f	600.0	500.0	120.0
Beam Length of Rear Segment [um], c_r	200.0	350.0	100.0
Energy proportion of front segment, f_f	1.5	1.2	1.1
Energy proportion of rear segment, f_r	0.5	0.8	0.9
Width Error (%)	4.5	4.7	8.2
Depth Error (%)	13.7	15.2	15.2

The model exhibits a greater tendency to underestimate the melt pool depth and a slight bias to overestimate the melt pool width. Moreover, with a more defocus beam, the error of the model is observed to increase. The model could possibly be better calibrated through further adjustment of the heat source model parameters or the employment of anisotropic thermal conductivity enhancement factor in order to account for the fluid convection. Nonetheless, the model is shown to be able to predict the melt pool morphology of the EBM deposited CM247LC single-tracks with a good degree of success.

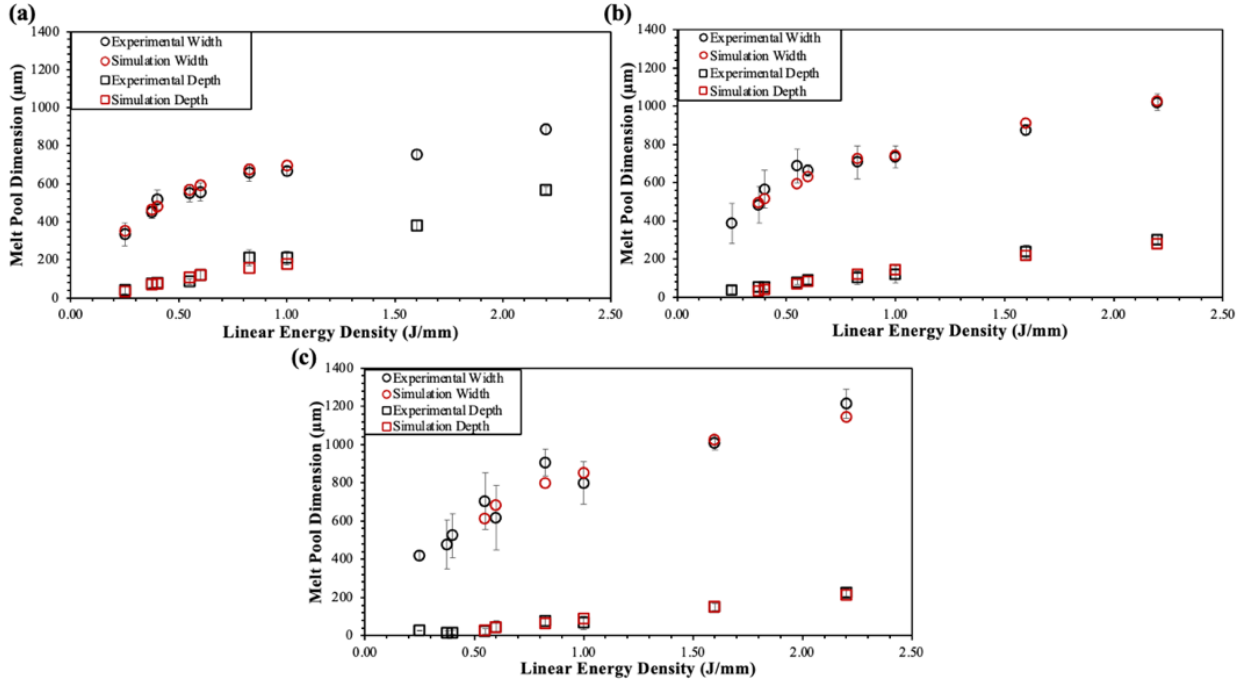


Figure 4-4. Comparison of the experimental and simulation results of melt pool depth and width for (a) focus offset 10 mA, (b) focus offset 20 mA, and (c) focus offset 30 mA

4.3.2 Temperature Distribution Within the Melt Pool

The various process parameter combinations can result in deposited melt pools with dissimilar temperature profiles. Fig. 4-5 is a scatterplot of snapshots capturing the translation of the heat source across the surface of the geometrical domain and at the same timestamp. The 3D simulation shows the heat source being situated at different points along the propagation direction. Additionally, it qualitatively emphasizes the effect of different process parameter combinations on the incident beam with respect to its shape, intensity, and concentration of heat input.

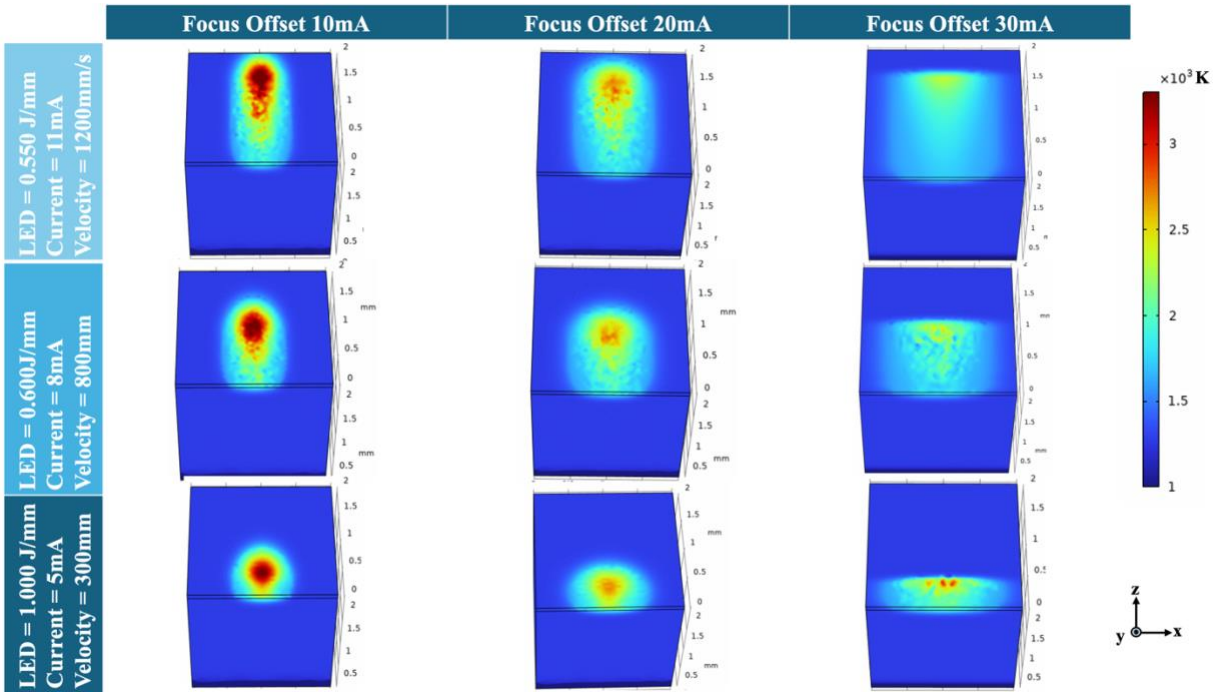


Figure 4-5. Graphical overview of 3D simulation results for select parameter combinations at fixed time

The qualitative overview of the bottom row in Fig. 4-5 can be interpreted quantitatively. A series of point probes distributed along the z-axis at the center of the track length (y =1.0 mm) were used to measure the temperature profiles and the thermal gradient magnitude (G) for each parameter combination. From the top surface, the probes were separated by an interval distance of 20 µm until the melt pool base (Fig. 4-6d). Fig. 4-6 displays the temperature distribution profiles of the melt pools corresponding to parameter combination of 5mA beam current, 300 mm/s scan speed, and a focus offset value of (a) 10, (b) 20, and (c) 30 mA.

For a given profile, the temperature peaked at the probe point situated closest to the surface (10 µm). Meanwhile, probes extending towards the melt pool base experience a decrease in temperature peaks. In comparing the three different temperature profiles, the defocusing of the beam and reduced energy concentration leads to lower global maximum of peak temperature from 2565.1 K to 2205.4 K, and 1932.0 K. It also reduces the distance along the z-axis that experiences temperature conditions exceeding the

melting temperature and thereby results in a shallower melt pool. The beam focus also has the effect of extending the duration that temperature conditions persist above the melting point. In the case of 10 mA focus offset, at y = 1 mm, temperatures completely cool below the melting temperature only after ~20 ms.

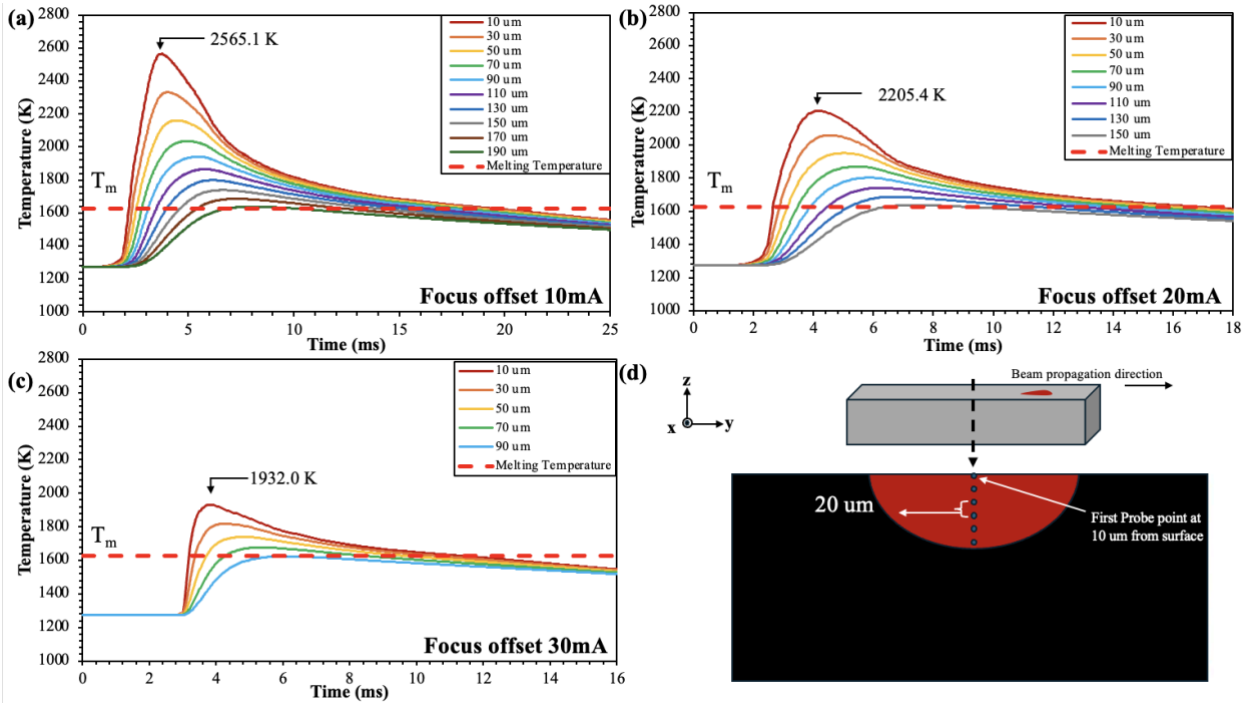


Figure 4-6. Temperature profiles of parameter combination 5 mA, 300 mm/s for focus offset of (a) 10 mA, (b) 20 mA, (c) 30 mA as measured by d) the probe points illustrated in schematic diagram

4.3.3 Evolution of Thermal Variables and the Effect of Process Parameters

For each process parameter combination, the temperature profiles were used to calculate the cooling rate (G*R) at each probe point by taking the slope of the tangent line at the initial point of solidification, e.g. the time in which the material cools below T_m. Meanwhile, the thermal gradient (G) magnitude was also directly measured by the probe points. The solidification parameters of cooling rate and thermal gradient are significant in describing and understanding of the local solidification conditions in a melt pool.

Fig. 4-7 explores the spatial evolution of the two solidification parameters within the melt pool for the 20 mA focus offset data group. For better clarity of the relationships between variables, the labelling of different linear energy densities was arranged through a color and shape order in such that increasing LED was identified by the following manner: blue < black < red and triangle < square < circle. The use of focus offset 20 mA experimental group was selected as it had the most data points for better analysis. The 10 mA and 30 mA focus offset groups showed similar relationships for the spatial evolution of thermal variables.

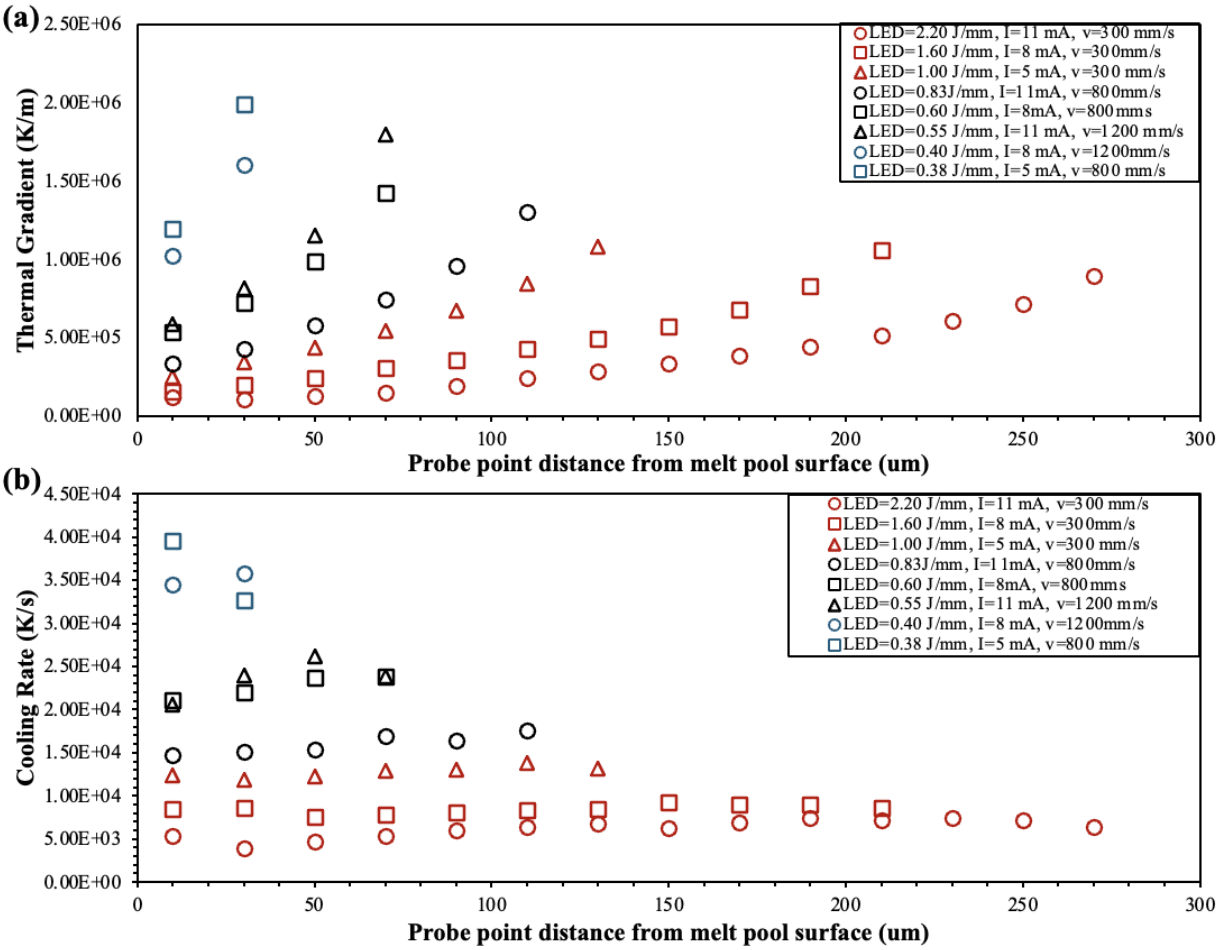


Figure 4-7. Spatial variation of (a) thermal gradient, and (b) cooling rate along the central z-axis within a melt pool for the experimental group of 20mA focus offset

For a given parameter combination, Fig. 4-7a displays the general trend of increasing thermal gradient with increasing probe point distance. Hence, the maximum thermal gradient is found to occur at the bottom of the melt pool boundary. In comparing across each data trend for a unique parameter combination, the reduction in LED levels from 2.200 J/mm to 0.375 J/mm fosters to a larger thermal gradient magnitude for a given probe distance. Furthermore, the data trend slopes reflect lower LED levels foster a steeper change in thermal gradient along the vertical center of the melt pool, indicating a greater temperature variation over a smaller distance.

Fig. 4-7b. exhibits the spatial evolution of cooling rate for the 20 mA focus offset group. For a given process parameter combination, the maximum cooling rates are inherent towards the melt pool base. The cooling rate progressively decreases towards the melt pool surface and the incident heat source. In some cases, a slight cooling rate reduction towards the melt pool base and the negative trend seen with LED level of 0.38 J/mm can be attributed to the mesh size. A finer mesh size determined through a mesh sensitivity analysis can resolve such errors. In comparing parameter combinations, as LED is increased, the magnitude of the

cooling rate is lowered. Moreover, the slope comparison reveals the degree of cooling rate fluctuation over a given distance is limited with higher LED levels, e.g. more spatially uniform cooling rates are fostered.

Further analysis can be conducted through the breakdown of the secondary parameter LED into its primary parameter constituents and studying their effects on the solidification parameters. This is done through a comparison of the maximum cooling rate and thermal gradient during the initial point of solidification (e.g. towards the bottom of the melt pool boundary). Fig. 4-8 assesses the effect of beam current and speed (a), and LED and focus offset (b) process parameters on the experienced maximum cooling rate. For the former, as focus offset is kept constant, the variation in speed is represented by the x-axis while the variation in beam current is distinguished by shape. An increase in current is indicated by the following shape order: triangle < square < circle. For the latter, color is used to identify the focus offset groups, with decreasing focus offset and a more focused beam is reflected by the color order: blue < black < red. This classification is applied in future figures.

In Fig. 4-8a, moving across the horizontal axis with the same beam current (e.g. same shape label), the increase in beam speed from 300 mm/s to 1200 mm/s results in a higher cooling rate experienced. On the other hand, for a fixed speed, increasing the current from 5 mA to 11 mA leads to a decrease in cooling rate. In some cases, the magnitude of the cooling rate reduction by the beam current is comparable to the cooling rate enhancement associated with a faster beam speed. However, the degree of reduction in cooling rate caused by beam current is observed to be less significant with a slower speed. Fig. 4-8b displays a clear exponential decrease in cooling rate when LED is scaled from 0.250 J/mm to 2.200 J/mm. For the case of 20 and 30 mA focus offset, the cooling rate order of magnitude can be reduced from 10^4 K/s to 10^3K/s. At the same linear energy density, a higher focus offset is generally found to facilitate a higher cooling rate.

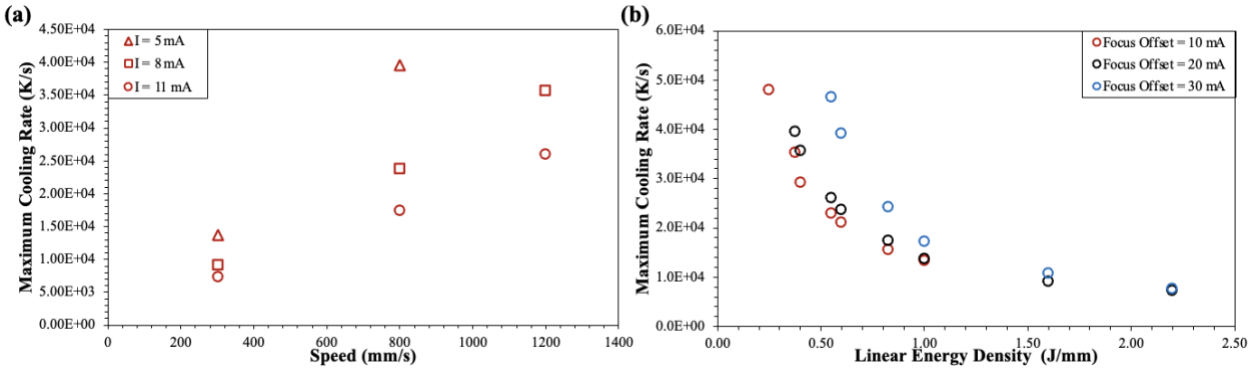


Figure 4-8. The cooling rate as a function of (a) speed for focus offset 20 mA and (b) LED

Fig. 4-9 exhibits the influence of process parameters on the maximum thermal gradient. Within the three focus offset subgroups, it is for the most part observed that an increase in beam speed results in a general increase in thermal gradient. Moreover, a weak negative correlation is generally evident between LED and

the experienced thermal gradient. With regards to the effect of beam current and focus offset on the thermal gradient, no clear trend was evidenced. This could be due to certain interactive effects of some process parameters which may have a stronger role under specific beam states. For instance, while the focus offset influences the fixed focal point and energy distribution [31], [38], the beam current affects the amount of energy supplied, and beam speed affects the rate an applied heat source is withdrawn and supplied heat is dissipated [105]. Additionally, the resulting shape and volume of the deposited melt pool could also play a role in the spatial distribution of temperature.

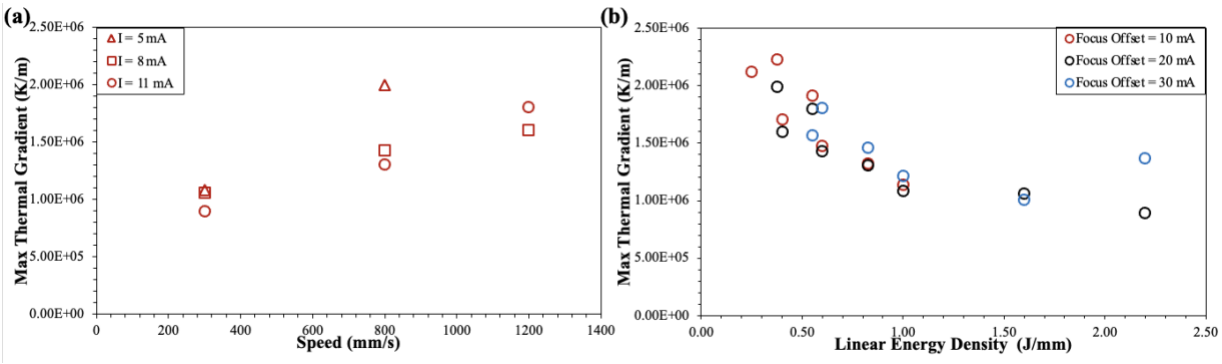


Figure 4-9. The thermal gradient as a function of (a) speed for focus offset of 20 mA and (b) LED

4.3.4 The Effect of Melt Pool Morphology and Thermal Variables

As demonstrated in Chapter 3, the print parameters are key in controlling the morphology of the deposited melt pool. The resulting melt pool shape and volume can also have a contributing role in the manner the thermal energy evolves and is spatially distributed. The influence on the thermal gradient, and cooling rate can consequently affect the final properties and quality of the print through its microstructure and susceptibility to cracking [10], [106]. Fig. 4-10 explores the relationship of thermal variables as a function of the melt pool aspect ratio (Depth/Width). These were previously measured in Chapter 3.

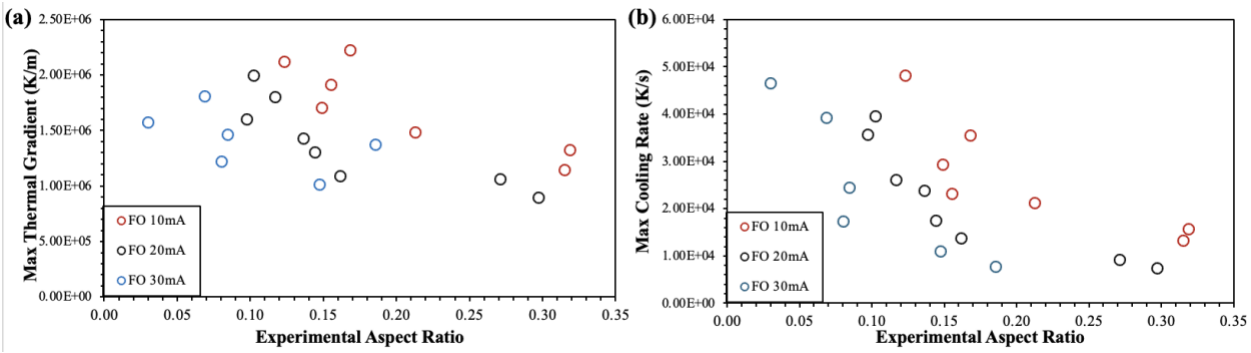


Figure 4-10. Correlation between melt pool aspect ratio and solidification parameters (a) thermal gradient, and (b) cooling rate

For the overall dataset and for each focus offset subgroup, Fig. 4-10a broadly exhibits a weak negative correlation between thermal gradient and the aspect ratio of a melt pool. This translates in a melt pool with an increasingly comparable depth relative to its width to exhibit a lower thermal gradient than a wide melt pool with a limited depth. In a similar manner, Fig. 4-10b also shows the inherent maximum cooling rate is negatively correlated to the melt pool aspect ratio. As the aspect ratio of a melt pool is increased, the associated cooling rate is reduced. On a separate note, a reduced focus offset enables the process parameter combinations to deposit a melt pool with a larger aspect ratio. As such, the focus offset parameter is observed to be able to translate the trend of the two solidification parameters to be associated with a different aspect ratio range. For instance, with a higher focus offset, the weakly negative solidification parameter trend is shifted to a range of lower aspect ratios involving wider and shallower melt pools.

4.3.5 Influence of Solidification Conditions on Cracking

The solidification conditions can influence the amount of internal stress the deposited material can experience. In severe cases, it results in cracks that debilitate the mechanical properties and the part performance of a printed material. This section importantly explores the effect of the thermal response of the material on the assessed crack severity in order to determine the suitable solidification conditions for a minimized crack susceptibility.

Fig. 4-11 correlates the thermal conditions at the bottom of the melt pool during solidification and the measured degree of cracking for each process parameter combination. The crack length density metric was used to assess the crack severity. This was previously determined through the characterization work done in Chapter 3. Fig. 4-11a broadly illustrates a crack length density can be limited by fostering a melt pool with a lower maximum thermal gradient. This general weak relationship is more prominent for the 20 mA and 30 mA focus offset case. For the data subset of 10 mA focus offset, no clear trend was visible. Within this data subset, an outlying data point corresponded to the second most severe cracking case of 2.30 mm/mm^2. This was fostered by a beam current, speed and focus offset of 11mA, 800mm/s and 10 mA respectively. On the other hand, the lowest crack severity case was also found to have a comparatively low thermal gradient magnitude.

Fig. 4-11b explores the relationship between maximum cooling rate and the witnessed cracking severity. The increase in cooling rate exacerbates the severity of cracking experienced in a melt pool for the focus offset of 20 mA and 30 mA groups. For the case of focus offset of 10 mA, the weak positive correlation between crack length density and cooling rate as seen with 20 mA and 30 mA focus offset group was absent and no other visible trend was apparent. However, the focus offset 10 mA data group shared a similar message. The simulation results indicated that the process parameter combination previously associated with the lowest crack length density in Chapter 3 was on the lower magnitude spectrum of simulated cooling

rates. Furthermore, this data point was the lowest cooling rate for the focus offset of 10 mA subgroup. The parameter combination comprised of a 5 mA beam current, 300 mm/s beam speed and resulted in an aspect ratio of 0.32.

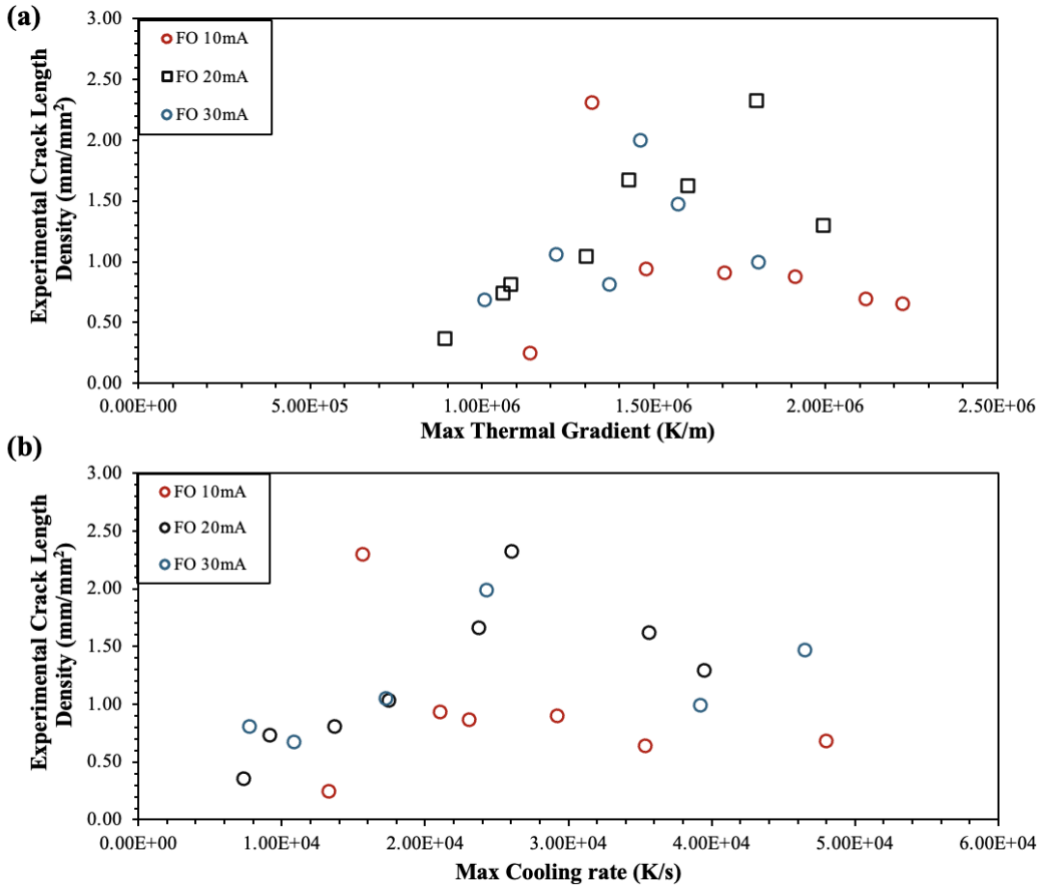


Figure 4-11. The behavior of crack length density as a function of (a) max thermal gradient and (b) max cooling rate

The correlated simulation results agree with previous works regarding solidification conditions and cracking where a steep temperature gradient, as facilitated by high beam velocities, has been previously observed to facilitate greater internal thermal stresses within a fabricated part [107], [108], [109]. As seen in Fig. 4-7a, the steeper thermal gradients were observed with lower LED values facilitated by high beam velocities. A prominent example is the parameter set with a beam current of 11 mA, beam speed of 1200mm/s and focus offset of 20 mA, showing one of the steepest thermal gradients in the z direction along the melt pool center. This consequently corresponded to the crack length density of 2.33 mm/mm^2 and was the most severe case of cracking across all process parameter combinations. Separately, the correlation of a low maximum cooling rate and thermal gradient to a reduced degree of crack occurrence has also been similarly witnessed by Barr et al [110], Chauvet et al [111], and Chen et al [109] for other metal alloys and is attributed the lower thermal stress experienced.

4.4 Summary

For this study, a simple thermal model was constructed to simulate the temperature profiles of CM247LC single-track as deposited by different EBM process parameter combinations. A quantitative assessment was conducted on the single-track solidification conditions as described by the thermal variables of thermal gradient, and cooling rate. Consequently, the evolution of these solidification parameters was explored. Furthermore, the effect of beam current, beam speed, focus offset, and linear energy density on the thermal variables were studied. The thermal variables at the melt pool base during initial solidification were also correlated to the melt pool aspect ratio and crack length density. From the analysis conducted, a summary of key findings are as follows:

- Comparison between simulated to the experimental results showed that the average width and depth error for each focus offset group were under 16%. Across the overall model, the average error was ~10%.
- Peak temperatures decreased with increasing distance away from the melt pool surface and higher focus offset further reduced the global max temperatures.
- With decreasing LED, thermal gradients steeply varied along the vertical (z-axis) distance, Similarly, with increasing LED, cooling rate observed a more gradual change over increasing depth.
- Cooling rate increased with higher beam speed and focus offset, and lower beam current. Thermal gradient generally increased with increasing beam speed. Higher LED values resulted in a decrease in the two solidification parameters.
- An increase in aspect ratio was negatively correlated with thermal gradient and cooling rate. Additionally, a lower thermal gradient and cooling rate was found conducive to foster a reduced crack length density, and thereby mitigate the tendency of the material towards cracking

Chapter 5. Multi-tracks: Study of Line Offset and Thermal Accumulation

5.1 Introduction

EBM is a bottom-up fabrication process starting from the deposition of a single-track [8]. This is followed by the fusion and linkage of multiple single-tracks to create a single layer of multi-tracks [54]. The stacking and linkage of multiple individual layers of multi-tracks cumulatively results in a coherent part. From this perspective, it is evident that the quality of the track and the bond between multiple tracks and layers are significant as they will ultimately determine the final quality, mechanical properties and performance of the fabricated part in their target applications [8], [54]. Hence, efforts have been devoted to optimize the energy supplied and studying the effects of print parameters that define the track and bond quality.

Line offset, also referred to as hatch spacing in LPBF, is a critical process parameter that governs the bond quality between adjacent tracks [39]. The parameter controls the separation distance between two successive tracks, and consequently directs the degree of track overlap [47], [41]. The manner of lateral track arrangement can impact the thermal cycle history and the part quality and properties. Yue et al. [112] investigated the microstructure and mechanical properties of EBM processed Ti-47Al-2Cr-2Nb at three different line offset levels of 85 um, 100 um, and 115 um. They had found that a high line offset resulted in a lower aluminum content lost by evaporation and a lower volume fraction of high angle grain boundaries [112]. The middle line offset level exhibited better mechanical performance in terms of ultimate tensile strength and elongation at room temperature, and at elevated temperatures of 700ºC and 750ºC [112]. Silvestri et al. [39] explored the effect of beam current, speed, and line offset for a fixed volumetric energy density (VED) of 40 J/mm^3. While no clear relationship was evident between line offset and hardness, an increase in line offset was found to be associated with a higher surface roughness for the top surface of an EBM fabricated Ti-6Al-4V part [39]. Gong et al. [113] found that the porosity of EBM processed Ti-6Al-4V and line offset shared a positive correlation. Hu et al. [114] studied the cracking behavior of Al-Cu alloys processed by LPBF and observed that a lower hatch spacing fostered crack free parts.

In the previous work, the influence of primary EBM process parameters on the melt pool morphology of EBM deposited CM247LC single-tracks was explored. Whereby, for this basic build unit, the relationship between process parameter, microstructure, thermal history, and cracking tendencies was explored. This current study expands on preceding work and focuses on the next deposition outcome, the single layer formation of multi-tracks. The objective of this work is to investigate the influence of line offset and the number of successive tracks on the processability of CM247LC via EBM. From the track-by-track nature, the heat accumulation effect on surface quality, melt pool morphology and microstructure are investigated and subsequently correlated to the cracking behavior. The results will provide a better grasp on the manner deposited tracks are laterally arranged in a single layer to mitigate the crack susceptibility of CM247LC.

5.2 Materials and Method

5.2.1 Print Setup

The CM247LC powder was produced via argon gas atomization technique and supplied by Höganäs. The powder particle size distribution ranged from 45-150 um. It is important to note that the powder used for this study is not in virgin state and recycled powder is utilized instead.

The Arcam A2X equipped with the EBM control 5.0 software system was used for the multi-track deposition. The multi-tracks were deposited on a 304 stainless steel build plate under chamber conditions comprised of a high vacuum pressure on the scale order of 10^{-3} mbar with a small injection of helium gas. A user-defined layer thickness of 70 µm was employed along with a preheat temperature of 1000 ºC.

The multi-track build design was prepared on Materialise Magics 27.03 software and is displayed in Fig. 5-1a. The part fabrication on the build plate followed the deposition sequence of supports, substrate, and the multi-track component. The supports and substrate enabled an easier sample preparation. The use of substrate prevented undesired dilution effects stemming between the 304 stainless steel build plate and the CM247LC multi-track. For the substrate, the parameter combination follows a beam current of 13.5 mA, beam speed of 1750 mm/s, and focus offset of 20mA. The substrate dimensions are 20 mm x 10 mm x 3 mm (Fig. 5-1a). The multi-tracks had a track length of 20 mm and were deposited with a snake scan strategy.

Fig 5-1b. illustrates the print and the internal chamber of the printer immediately after build completion. The build plate and fabricated parts are covered by a powder bed comprised of loose powder particles and a sintered powder cake. A vacuum is used to remove most of the surrounding powder. The build plate is recovered from the Arcam A2X chamber and final cleaning was done with the Arcam powder recovery system. Fig. 5-1c displays the recovered build plate and the overall final quality of the deposited parts.

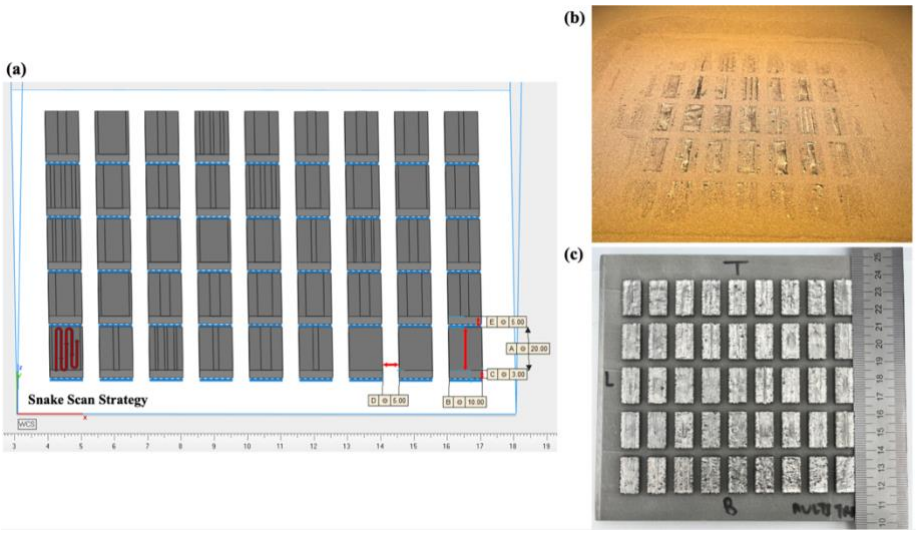


Figure 5-1. The workflow of the experimental multi track starting from the (a) build design, (b) to print completion, and (c) post recovery state

5.2.2 Experimental Design

The multi-track study investigates the heat accumulation effect from the successive deposition of single-tracks with varying line offset, and thus track overlap. For this investigation, the selection of the process parameters that governs the linear energy density input of the basic building block is important. The previous work done with single-tracks (Fig 5-2) guides the selection to avoid parameter combinations that would foster a compromised track quality.

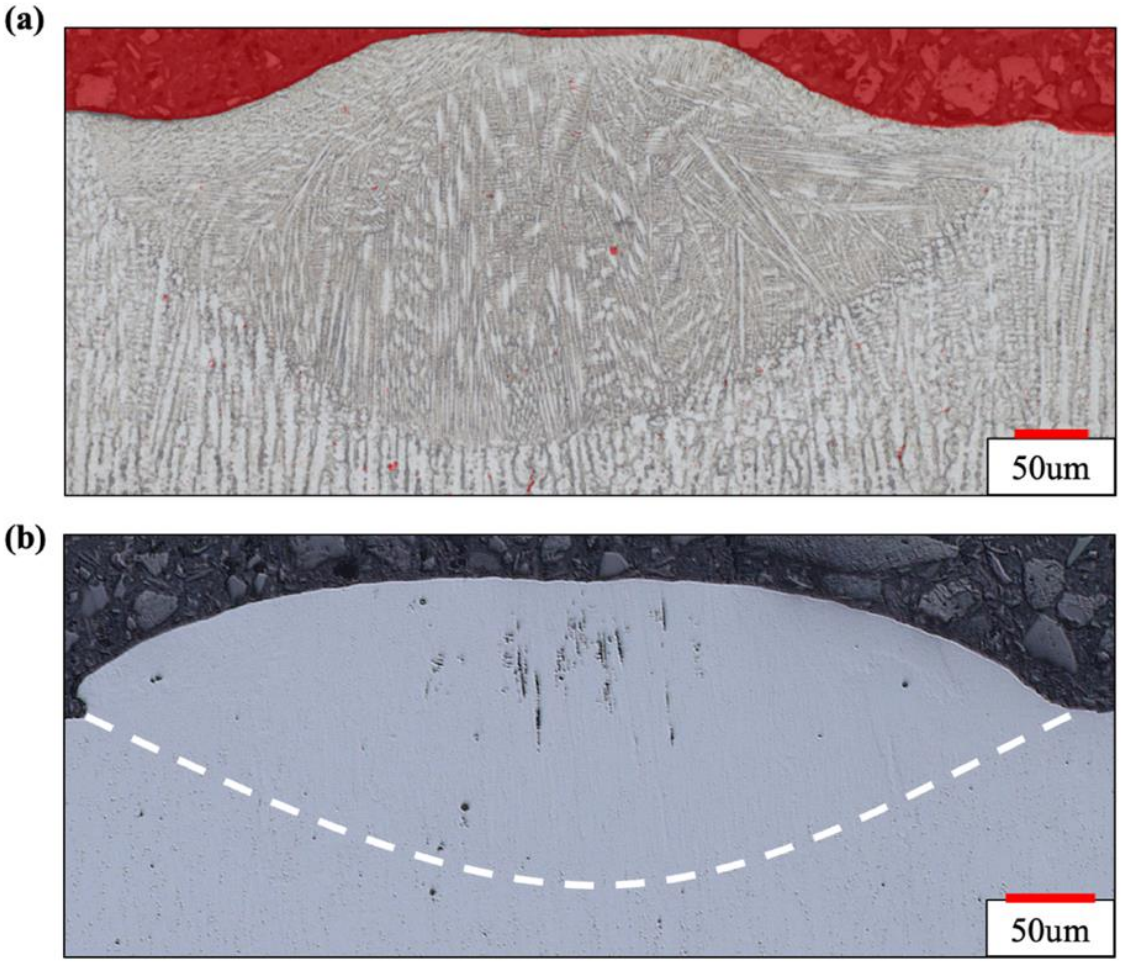


Figure 5-2. EBM CM247LC single-track cross section fabricated with a beam current, speed, and focus offset magnitudes of (a) 5 mA, 300 mm/s, 10mA and (b) 11 mA, 1200 mm/s, and 10mA respectively

An optimal beam current, speed and focus offset was determined in which displayed a limited case of cracking. This corresponded to a magnitude of 5 mA, 300 mm/s and 10 mA respectively and an average crack length density of 0.25 mm/mm^2 (Fig. 5-2a). Along with the low current and speed combination, a secondary parameter set comprising of a high beam current (11 mA) and speed (1200 mm/s) under a 10mA focus offset was also used for the individual track (Fig. 5-2b). While the secondary parameter set did not demonstrate the second lowest degree of cracking, with a crack length density of 0.87 mm/mm^2, it was selected because it was on the other extreme end of process parameter values. Additionally, it demonstrated

very little to no defects along the melt pool boundary (e.g. shrinkage pores or liquation cracks). Instead, most of the existing defects are predominantly consolidated in the top central region of the melt pool. This would be capable of being remelted in future overlaying melt layers. The first parameter set of a low current and low speed extreme will be referenced to as Group A while the second parameter set of a high current and high speed extreme will be referred to as Group B.

The single layer multi-track focuses on the quality of the inter-track bond linkage and heat accumulation effects of consecutively deposited single-tracks. This is studied through the controlled variation of line offset and the number of successively deposited tracks using both single-track process parameter extremes (e.g. low current and speed and high current and speed combination). The line offset or the extent of track overlap will have three separation distance levels of 40 µm, 100 µm, and 160 µm. Meanwhile, the number of tracks that are successively deposited will increase in the following order of 5, 25 and 50 tracks. Table 5-1 provides a randomized and detailed list of the parameter combinations employed. Each parameter set had a total of three replicates. The volumetric energy density (VED) is a secondary parameter that represents the amount of energy supplied per unit volume and its expression is listed as follows (Eqn. 5-1)

$$VED = \frac{V*I}{l_{\text{offset}}*v*t} \tag{5-1}$$

where V is the acceleration voltage [V], I is the beam current [A], l_{offset} is the line offset [mm], v is the beam speed [mm/s], and t is the layer thickness [mm].

Table 5-1. Comprehensive List of Process Parameter for the Multi-track Study

Sample #	Beam Current, I [mA]	Beam Speed, v [mm/s]	Line offset, L.O. [mm]	Volumetric Energy Density, VED [J/mm^3]	# of Track
1	5	300	0.04	357.14	50
2	11	1200	0.16	49.11	50
3	11	1200	0.04	196.43	50
4	5	300	0.10	142.86	5
5	11	1200	0.16	49.11	25
6	5	300	0.04	357.14	50
7	5	300	0.10	142.86	25
8	11	1200	0.16	49.11	25
9	11	1200	0.04	196.43	25
10	11	1200	0.16	49.11	5
11	5	300	0.10	142.86	50
12	11	1200	0.04	196.43	50
13	11	1200	0.04	196.43	25
14	5	300	0.16	89.29	5
15	5	300	0.16	89.29	25
16	11	1200	0.10	78.57	50
17	11	1200	0.16	49.11	50
18	11	1200	0.16	49.11	25
19	11	1200	0.10	78.57	5
20	11	1200	0.10	78.57	50
21	11	1200	0.16	49.11	50
22	5	300	0.16	89.29	50
23	5	300	0.10	142.86	50
24	11	1200	0.04	196.43	25
25	11	1200	0.04	196.43	5
26	5	300	0.04	357.14	50
27	11	1200	0.10	78.57	25
28	5	300	0.10	142.86	50
29	5	300	0.16	89.29	50
30	11	1200	0.10	78.57	25
31	5	300	0.10	142.86	25
32	5	300	0.16	89.29	25
33	11	1200	0.10	78.57	50
34	11	1200	0.10	78.57	25
35	5	300	0.16	89.29	25
36	11	1200	0.04	196.43	50
37	5	300	0.16	89.29	50
38	5	300	0.04	357.14	25
39	5	300	0.04	357.14	5
40	5	300	0.04	357.14	25
41	5	300	0.10	142.86	25
42	5	300	0.04	357.14	25

5.2.3 Sample Preparation and Characterization

After the EBM deposition process, the CM247LC multi-track specimens were sectioned into three equidistant lengths using a Struers Labotom-5 abrasive cut-off saw and a Struers 50A26 cut-off blade. Struers PolyFast hot mount resin media was used to encapsulate the top and bottom sample segments, and the hot mounting process was done by a Struers CitoPress-5. The exposed sample surface of x-z cross sectional planes were systematically grinded with silicon carbide grinding papers of increasing FEPA P grit sizes as follows: 80, 120, 320, 500, 800, 1200, 2400 and 4000. The mounted samples were subsequently polished with Buehler MasterPrep alumina polishing suspension media by means of a Buehler VibroMet 2 Vibratory Polisher. The final surface finish was achieved after the duration of four and a half hours. The samples were etched with a Glyceregia mixture to reveal the microstructure. The chemical composition of the mixture was 25mL of hydrochloric acid, 5 mL of glycerol, and 5 mL of nitric acid.

The Keyence VK-X250 Laser Profilometer was used to evaluate the surface topography of the deposited CM247LC multi-tracks. The assessment was done for the middle section of the sample top surface prior to any metallurgical preparation. The x-z cross sections of the multi-tracks were observed with a Keyence VHX-7000 digital optical microscopy (OM). The region of interest was documented by stitch images of 200x magnification in the pre-etch and etch condition. The ImageJ software was used to perform quantitative analysis of the deposited multi-tracks. The pre-etch images were overlayed with etch images in order to perform crack analysis within the multi-track cross section. In the etch condition, the geometrical dimensions of the last melt pool were quantitatively measured. The microstructure of the multi-tracks was also analyzed by TESCAN Vega3 scanning electron microscopy (SEM) where the Bruker eflash FS detector accessory allowed electron backscattered diffraction (EBSD) measurements to be performed.

5.3 Results and Discussion

5.3.1 Assessment of Layer uniformity – Surface Topography

A relatively uniform and flat single layer of multi-tracks is significant in the consideration of achieving an overall highly dense part. Surface inhomogeneity caused by defects and instabilities may lead to complications with uniformly spreading the desired layer thickness of powder or possible rake damage from collisions with acute surface protrusions. Therefore, an assessment on the surface layer quality is performed for the deposited CM247LC multi-tracks.

In Fig. 5-3, the surface topographies of Group A multi-tracks are compared as the line offset and the number of consecutive tracks are increased. Based on the qualitative color distribution, the central region of the deposited multi-tracks exhibits a relatively uniform surface and is absent of any sharp protrusions or drastic difference in height level. The average S_a evaluation for each Group A experimental condition ranged from

37-46 µm with an increase track number mostly leading to a very minor increase in S_a. The quantitative and qualitative assessments of the multi-track surface quality are in agreement. However, a minor detail of a small macro-scale height difference is observed, where one lateral side of the multi-track region is elevated in contrast to the other. This is slightly more evident with a lower line offset.

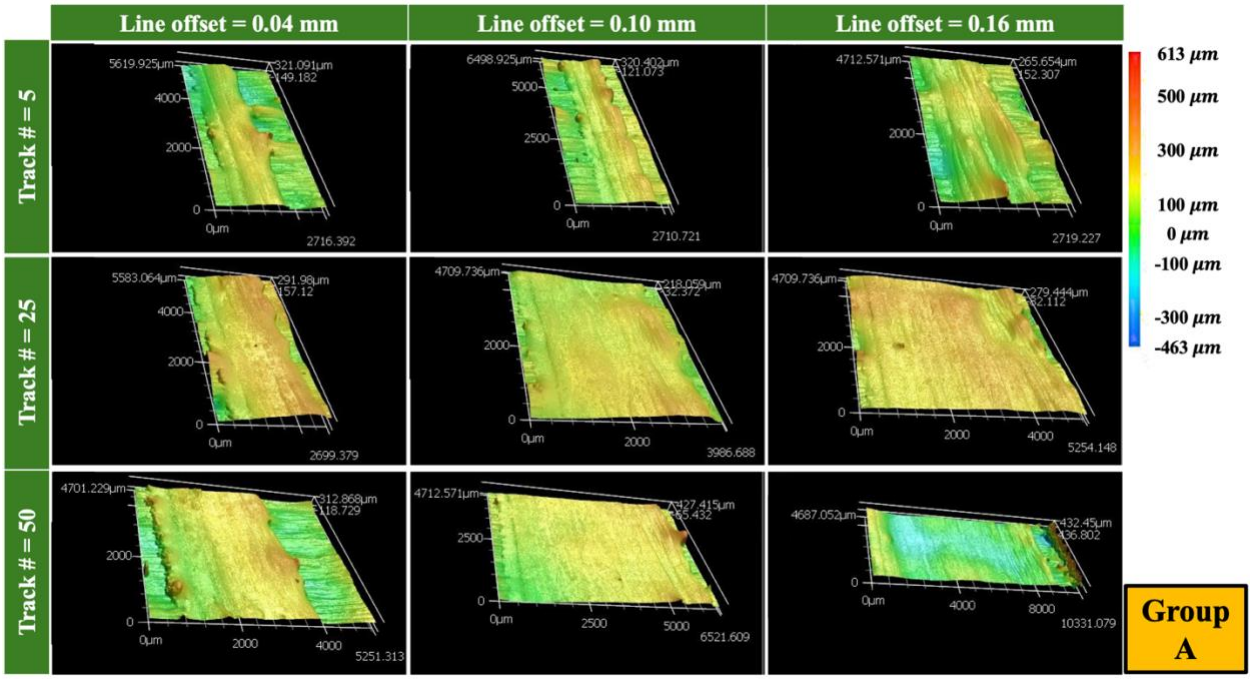


Figure 5-3. Surface topography overview of Group A (I = 5 mA, v = 300 mm/s) for surface quality assessment of the multi-track central segment

Fig. 5-4 compares the surface topography of Group B with increasing line offset and track number. The multi-track surfaces of Group B vary to a larger extent in contrast to Group A. In addition, the previous detail of height elevation is more pronounced in Group B. For the case of 0.04 mm, this was evident with Track# = 5 and exaggerated further with Track# = 25 where a clear valley and peak surface profile is evident. The latter case could pose a challenge for subsequent layer deposition. However, under the same line offset, Track# = 50 does not display an evident height difference but instead displays an overall coherent bulge spanning the width of the multi-track region. For the line offset case of 0.10 mm, an evident bulge is situated before the last deposited tracks which exhibits a lower elevation level in comparison. The S_z metric can evaluate the macroscopic height profile difference across the multi-track surface. This summation of peak height and valley depth reveals the height profile difference was most prominent for a line offset of 0.10 mm with a track number of 25 and 50 in comparison to other tested variable conditions. This corresponded to values of 646.06 µm and 753.35 µm. On a separate note, for the line offset case of 0.16mm in Group B, a more ripple textured surface is apparent.

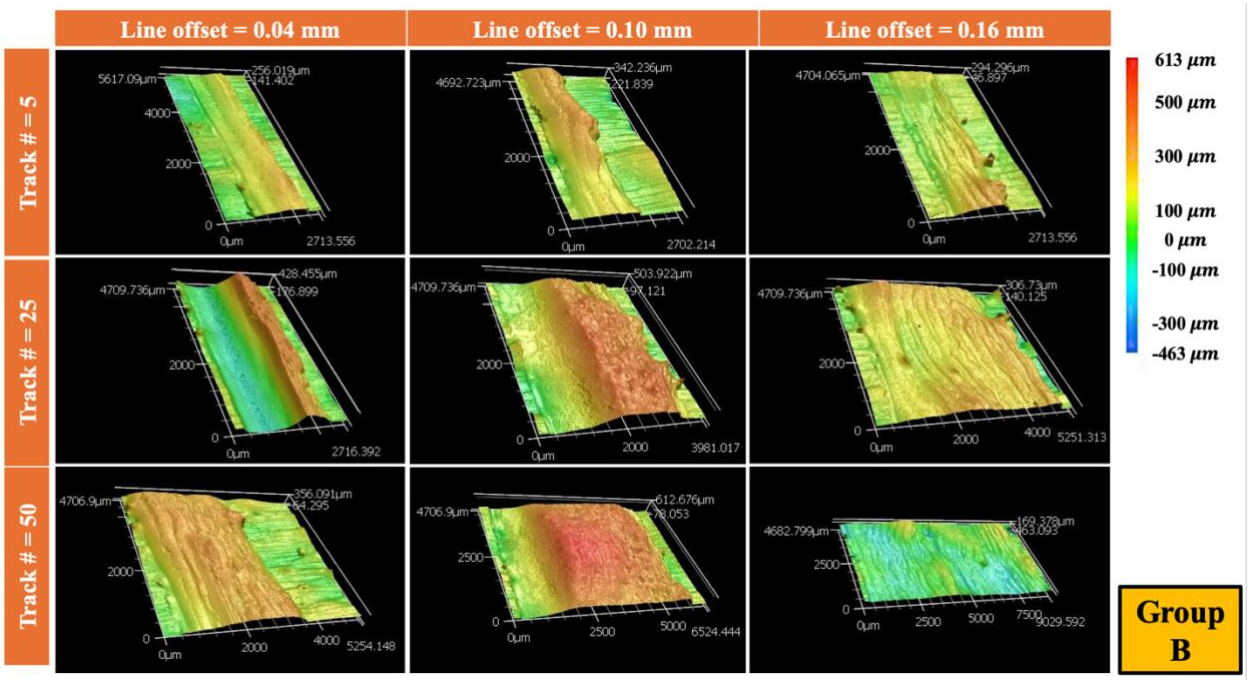


Figure 5-4. Surface topography overview of Group B (I = 11 mA, v = 1200 mm/s) for surface quality assessment of the multi-track central segment

Through finite volume method modelling of Inconel 718 by LPBF, Xia et al [115] attributes the height difference due to the nature of the melt flow. During deposition, a temperature gradient is facilitated in the inherent melt pool which correspondingly gives rise to a surface tension gradient [115]. Whereby, Marangoni convection mechanism involves the molten liquid flow to migrate in the direction from a high temperature, low viscosity, and low surface tension region to a low temperature, high viscosity, and high surface tension region [115]. In other words, from the center region of the melt pool near the incident beam to the edge of the melt pool such as that closer to the previously deposited track, respectively [115]. This mechanism can help explain the height difference in the surface profile. For the low scan speed case, as line offset is reduced, the greater track overlap results in a given track area being remelted a greater number of times. This increase in accumulated heat would facilitate a greater temperature peak and more melt volume [106]. Consequently, the greater temperature peaks can reduce the viscosity of the melt liquid and lead to an increase amount of melt liquid that migrates towards the melt pool edge near the previously deposited tracks [115]. Thereby, the surface profile is elevated. As line offset is increased, the degree of track overlap, heat accumulation, peak temperature, and melt volume is reduced. Therefore, the increased viscous flow results in less material migration and a lower height difference in surface profile [115].

The employed model provides a limited exploration of height magnitude differences in a surface profile as a relatively low beam speed (400 mm/s) and power value (110W) was employed [115]. This is similar to the case of Group A. Breuning et al [116] provides further possible details of the height difference in the

surface profiles. The slow speed can facilitate a trailing melt pool condition, whereby the preceding track has already undergone solidification as a new track is being deposited [116]. For this condition, most of the material transport had been found towards to the tail end [116].

In contrast, as group B employs a higher power (660W) and beam speed (1200 mm/s), the previously deposited tracks may still be in a liquid phase state during the deposition of a new adjacent track. This persisting liquid phase condition due to a faster beam return time has been termed as a persistent melt pool [116]. Consequently, due to the fluid nature of the deposition, the extent that line offset can have an influence on the height difference for a given surface profile can be significantly more pronounce, depending on the stability of the molten liquid flow.

The persistent melt pool has been subdivided into a permanent and partially permanent classification [116]. For the former, the persisting liquid melt pool spans the entire scan length domain, and much of the material migration is in the opposite direction of the lateral progression[116]. This results in a relatively even and elevated melt surface for most of the surface body with the exception of a depression observed in the area of the final tracks [116]. For the partially permanent case, the persisting liquid melt pool spans most (e.g. ~3/4) of the scan length domain [116]. The material migration also occurs in the opposite direction of the lateral progression [116]. However, at the turning points of the snake scan strategy, the liquid pool will possess a temperature gradient and surface tension gradient vector directed towards the central melt area, and thereby, facilitates further material migration towards the central body [116]. This would further exacerbate the height difference as observed through S_z and Fig. 5-4 for the line offset case of 0.10 mm and Track# = 25, 50.

5.3.2 Microstructure: Melt pool geometry of EBM deposited CM247LC multi-tracks

An examination of the melt pool morphology can reveal the nature of the solidification conditions that consequently control the microstructure and properties of the final part. The use of Glyceregia can reveal the melt pool geometry under an optical microscope with a limited success, regardless of sample exposure time to the etchant. This can be observed in Fig. 5-5a. However, the Keyence VHX 7000 enables image enhancements, such as through contrast and brightness adjustments. As seen in Fig. 5-5b, the adjustments can better reveal the melt pool morphology and help in the clear identification of the melt pool shape.

Fig. 5-5a, b also exhibits the overall span and quality of the deposited multi-track corresponding to Group A with a line offset of 0.10 mm and a middle level track number. The cross-sectional view reveals a relatively uniform and organized stacking of melt pools. This highlights the stability of the melt pool during deposition. In contrast, Fig. 5-5c displays the overall multi-track span of Group B with the same line offset and track number. The irregular surface morphology and the cross section of the multi-track emphasizes

the fluid nature of the melt pool that compromises its stability during deposition. In addition, it also highlights the Marangoni convection in which drives the material migration and leads to the height difference within a surface profile. This is better highlighted by Fig. 5-5d where the individual overlapping melt pools are observed to be solidified at a slanted angle in contrast to the melt pools solidified in a neat alignment in Fig. 5-5b. This evidence supports previous discussion on the trailing and persistent melt pools. The difference in melt pool nature with Group B makes it difficult to distinguish the individual melt pools, particularly for the final deposited track. However, through the image enhancement tool, the melt pools in Group B (e.g. Fig. 5-5d) can be identified with the exception of line offset of 0.04 mm.

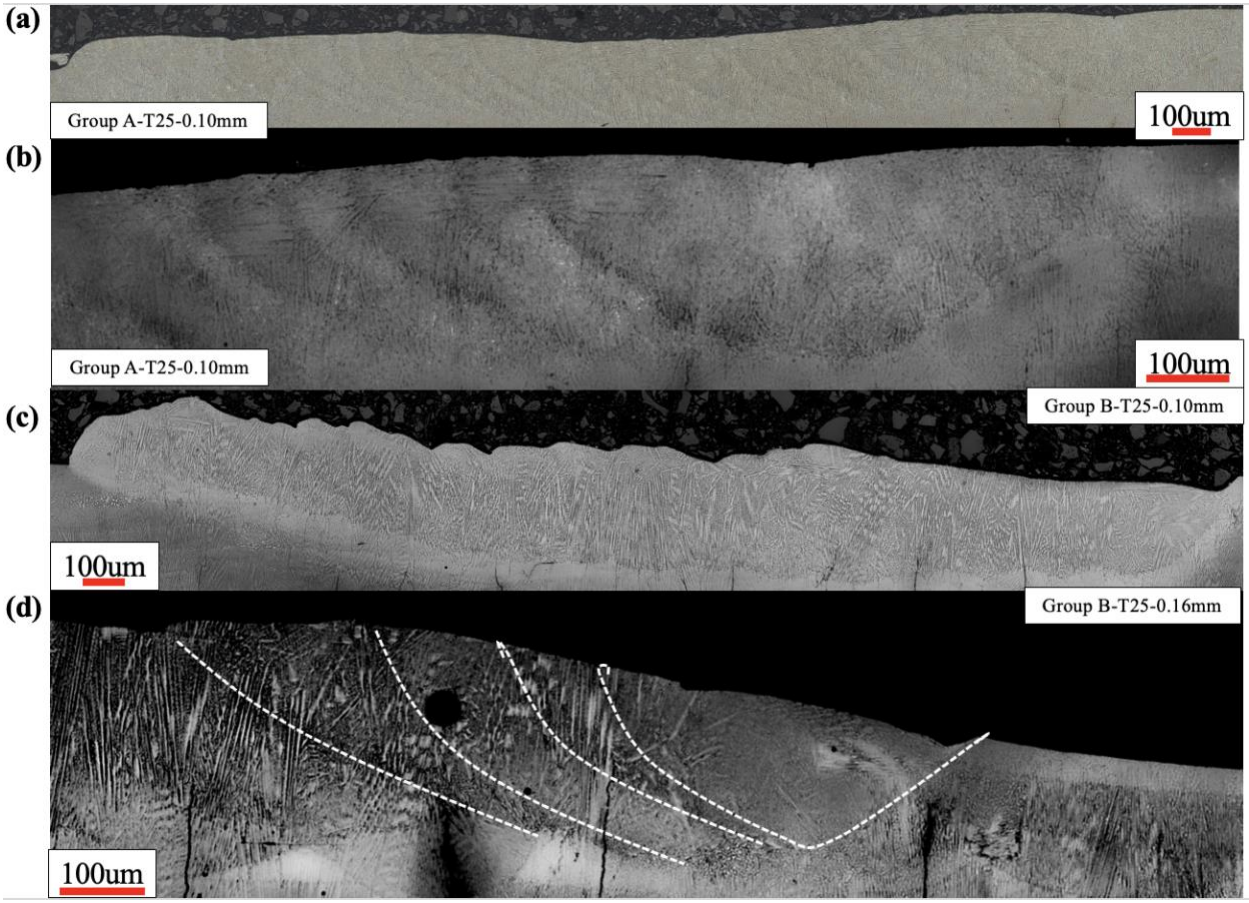


Figure 5-5. Melt pool morphology of CM247LC multi-track. (a) Etched multi-track melt pools without, and (b) with image enhancement for sample corresponding to Group A, track# = 25, line offset = 0.10 mm (c) overall multi-track appearance for Group B, Track#= 25, line offset 0.10 mm and (d) identification of individual overlapping melt pools in multitrack

Fig. 5-6 quantitatively describes the effects of line offset and the number of tracks on the melt pool morphology. The measured melt pool dimensions are associated with the last track to be deposited. Fig. 5-6a reveals melt pool depth (red) and width (black) decrease with increasing line offset. The extent of the effect highlights the melt pool dimensions of the multi-track can be lower than the dimensions corresponding to the single-track condition as marked by the dashed lines.

The deposition of preceding tracks will elevate the temperature of the surrounding powder that is to be melted in subsequent tracks [117], [118]. Due to the poor thermal conductivity of metal powder [4], as the separation distance between tracks is increased, the subsequent track would be deposited in a further region of lower temperature. Whereas, for a low line offset, the future subsequent track would be deposited in a higher temperature region because it is in a closer proximity to the previous track. Additionally, the tight track scans which leads to a high overlap would also enhance the consolidation of thermal energy per a given unit volume, e.g. a higher volumetric energy density. As a result, both pre-heat factor and thermal accumulation would help foster a deeper and wider melt pool [117], [118]. For the high line offset, the consolidation of thermal energy would be lower, and since the previously deposited tracks can also dissipate heat comparatively better than powder, the heat dissipation effect may be greater than the degree of heat accumulation, fostering melt pool dimensions that are possibly lower than the single track condition. On the separate note, the increase in the number of tracks (triangle < square < circle) also facilitates an increase in melt pool dimensions for the most part. This can be attributed to the increasing degree of thermal energy accumulation, stemming from the increase of heat input with each track.

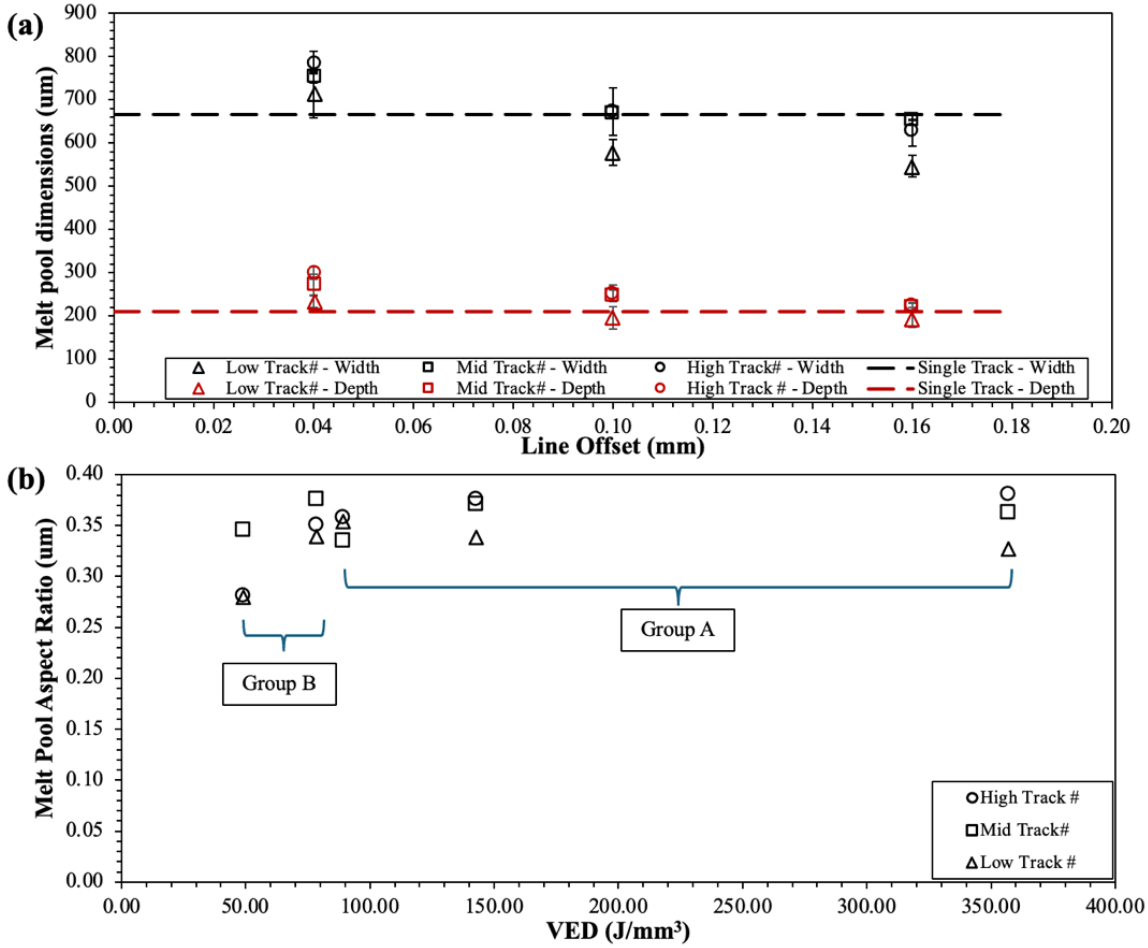


Figure 5-6. The influence of line offset and number of tracks on the melt pool (a) dimensions with regards to depth and width, and (b) aspect ratio.

Fig. 5-6b illustrates the influence of VED and number of tracks on the melt pool aspect ratio where aspect ratio is defined as the ratio of depth to width (D/W). For both groups, an increase in VED or lower line offset generally enables an increase in melt pool aspect ratio. However, for group A, the influence of VED transitioning from 142.86 J/mm^3 to 357.14 J/mm^3 appears to plateau or dip to a slight extent. No clear trend was observed for increasing the number of tracks on melt pool aspect ratio. Interestingly, for both groups and all multi-track variable permutations, the aspect ratio in the multi-track condition were greater than that of the single-track condition. For Group A, the single-track aspect ratio was 0.32 and the multi-track minimum and maximum aspect ratio were 0.32 and 0.38 respectively. For Group B, the single-track aspect ratio was 0.155 and the multi-track minimum and maximum aspect ratio were 0.28 and 0.38 respectively. The multi-track condition for Group B observed a more drastic increase in a melt pool aspect ratio. This can be attributed to the drastic increase in melt pool depth compared to its single-track depth whereby a minimum two-fold increase from 85.18μm to 169.91μm was observed.

5.3.3 Crack Behavior of EBM deposited CM247LC multi-tracks

In the pre-etch condition, the stitched images of the multi-track cross section enable the study of defect behavior for Group A and B experimental groups in response to varying line offset and number of tracks. First, a systematic qualitative assessment of the cross sections is performed to facilitate the discussion of the defect type based on their location. Following such, a quantitative evaluation of the crack susceptibility is conducted. Note the discussion of type of cracks and their formation mechanism has already been discussed in the previous single-track study, and as a result such will not be the focus in this section.

Fig. 5-7 are OM images of selected muti-track cross sections that pertain to Group A and serve as illustrative examples of the witnessed cracking behavior. For the line offset of 0.04 mm in Group A, the main defect consisted of shrinkage pores and liquation cracks along the melt pool boundary of the final few tracks that were deposited. These cracks and irregularly shaped micro-pores tend to be concentrated towards the bottom of the melt pool boundary as seen in Fig. 5-7a. Moreover, a minor degree of shrinkage pores is visible in the central multi-track melt body region. This could be aligned along the inter-track region delineated by the melt pool boundary; however, the pattern is not strongly evidenced. For the line offset of 0.10 mm in Group A, the chance of solidification cracking to be observed in the melt pool of the final track was fostered, particularly in the form of a distinct and prominent center-line crack with dendritic fracture appearance [13], [18], [50]. Similar to line offset case of 0.04 mm, a concentration of shrinkage pores and liquation cracks were observed along the melt pool boundary of the last few tracks. A number of shrinkage pores and liquation cracks was also found in the central multi-track melt body. This provided stronger pattern evidence of the defects being aligned along the inter-track regions marked by the melt pool boundary (e.g. the heat affected zone). The location pattern of the defects that were seen in the case of Group A for

line offset of 0.10 mm were also observed to persist for the line offset case of 0.16 mm. This is illustrated by Fig 5-7b and c. The chance of solidification cracking to occur in the form of a prominent centerline crack appeared to be higher for the line offset case of 0.16 mm. This is based on cross sectional samples showing more frequent occurrences of a centerline crack in the final melt pool track.

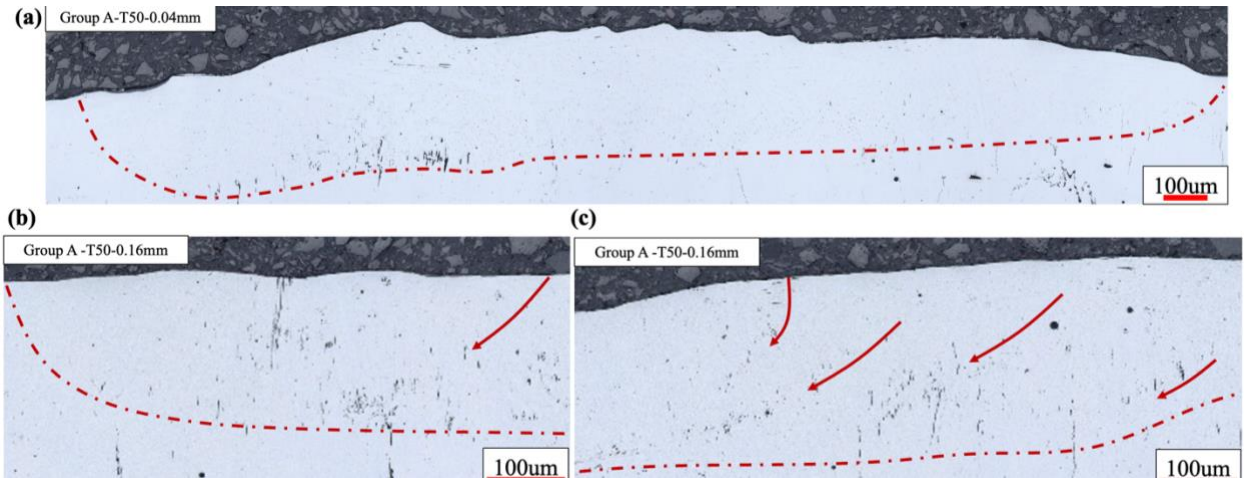


Figure 5-7. Qualitative assessment of crack behavior of Group A samples: (a) Track# = 50, line offset = 0.04 mm, (b) last few deposited tracks and (c) middle body region of Track#=50, line offset = 0.16mm

For all line offset cases, the experimental Group B similarly demonstrated a concentration of shrinkage pores and liquation cracks in the inter-track region closer to the last deposited track. However, based on qualitative observation, the extent of liquation crack and shrinkage pores to occur within this region appears to be slightly reduced with the other two line offset cases of 0.10 mm (Fig. 5-8a, c) and 0.16 mm. Nonetheless, this type and spatial location of defects are the main form of defects observed in the experimental Group B. In continuation, for Group B, the line offset case of 0.04 mm more frequently exhibited the possible occurrence of a prominent solidification crack in the last melt pool deposited, as characterized by its distinct dendritic like appearance [13], [18], [50]. This in contrast to Group A at the same line offset condition which rarely demonstrated any trace of such. Separately, the line offset case of 0.10 mm in Group B exhibited close to a defect free zone within the central melt body of the deposited multi-tracks. In other words, no evidence of liquation cracks and shrinkage pores were observed along the melt pool boundary of the inter-track regions. This is illustrated in Fig. 5-8b, c which displays a stark contrast to the equivalent line offset case of Group A. For the line offset case of 0.16 mm, the central melt body exhibited a minor degree of shrinkage pores and cracks presence, with weak pattern evidence of defect consolidation along the inter-track regions. Moreover, a greater propensity of solidification cracks to occur in the melt pool of the final track was also observed.

At this stage, the 0.10 mm line offset case of Group B is seen to be able to best facilitate solidification conditions that are less prone to defects in terms of pores and cracking. Additionally, the cross sections of Group B illustrated most of the defects were consolidated in the inter-track regions of the last few tracks to be deposited. On a separate note, it should be mentioned that a minor degree of gas induced porosity, as indicated by their perfect spherical morphology, was present in the cross section of the multi-track samples. This could be mainly attributed to the number of times the CM247LC powder has been reused since powder agglomeration and gas inclusion can increase with repeated exposure to a high heat source [119], [120].

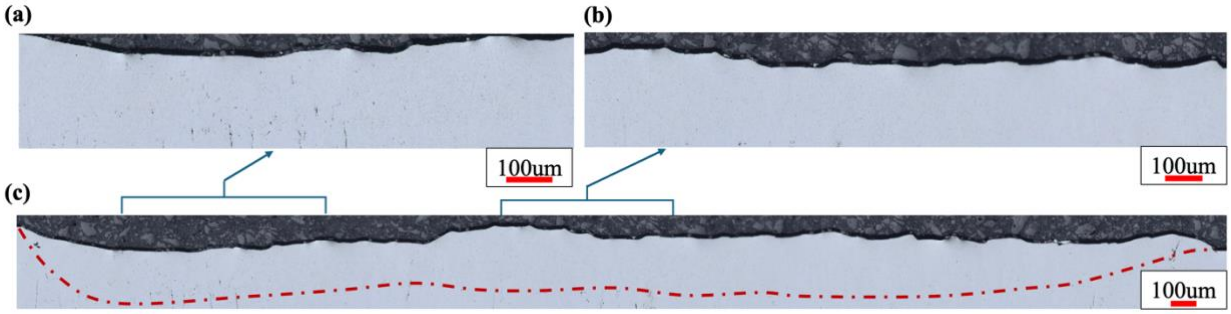


Figure 5-8. Qualitative assessment of crack behavior of Group B sample of Track# = 50, and line offset = 0.10 mm: (a) region of last few deposited tracks, (b) middle body region, (c) overall multi-track span

Fig. 5-9 provides a quantitative assessment of the crack and general defect severity with varying track number and line offset. The line offset variable is captured through the secondary parameter of VED while the crack and general defect severity are evaluated through the metric of crack length density (Fig. 5-9a) and areal defect density (Fig. 5-9b). The latter includes both pores and cracks whereas the former only includes the crack measurements that were manually performed through the ImageJ analysis software.

For a fixed number of tracks, it is for the most part observed that an increase VED leads to a further increase in crack length density (Fig. 5-9a) and areal defect density (Fig. 5-9b). For a fixed VED, the increase in number of tracks fosters a reduced average crack length density (Fig. 5-9a) and average areal defect density (Fig. 5-9b). The trends of both metrics as a function of VED and number of tracks corroborate with one another.

For a constant track number, a more focused observation of each group highlights a dip in the average crack length density and areal defect density that is associated with the middle line offset level of 0.10 mm. This corresponds to VED values of 142.86 J/mm^3 and 78.57 J/mm^3. For instance, in Group B, at a high track number level and with a reduction in line offset values, the VED levels of 49.11 J/mm^3, 78.57 J/mm^3, and 196.43 J/mm^3 resulted in an average crack length density measurement of 0.81 mm/mm^2, 0.71 mm/mm^2, and 1.872 mm/mm^2 respectively. Consequently, the shared downturn associated with the middle line offset level for both groups can serve as an indicator that the optimal line offset value lies in proximity to 0.10

mm. The multi-track cross-section associated with a VED level of 78.57 J/mm^3 had the minimum propensity towards cracking and general defect formation, with values of 0.71 mm/mm^2 and 0.27% respectively. The parameter combination of this VED level includes a beam current of 11 mA, beam speed of 1200 mm/s, focus offset of 10mA, and a line offset of 0.10 mm.

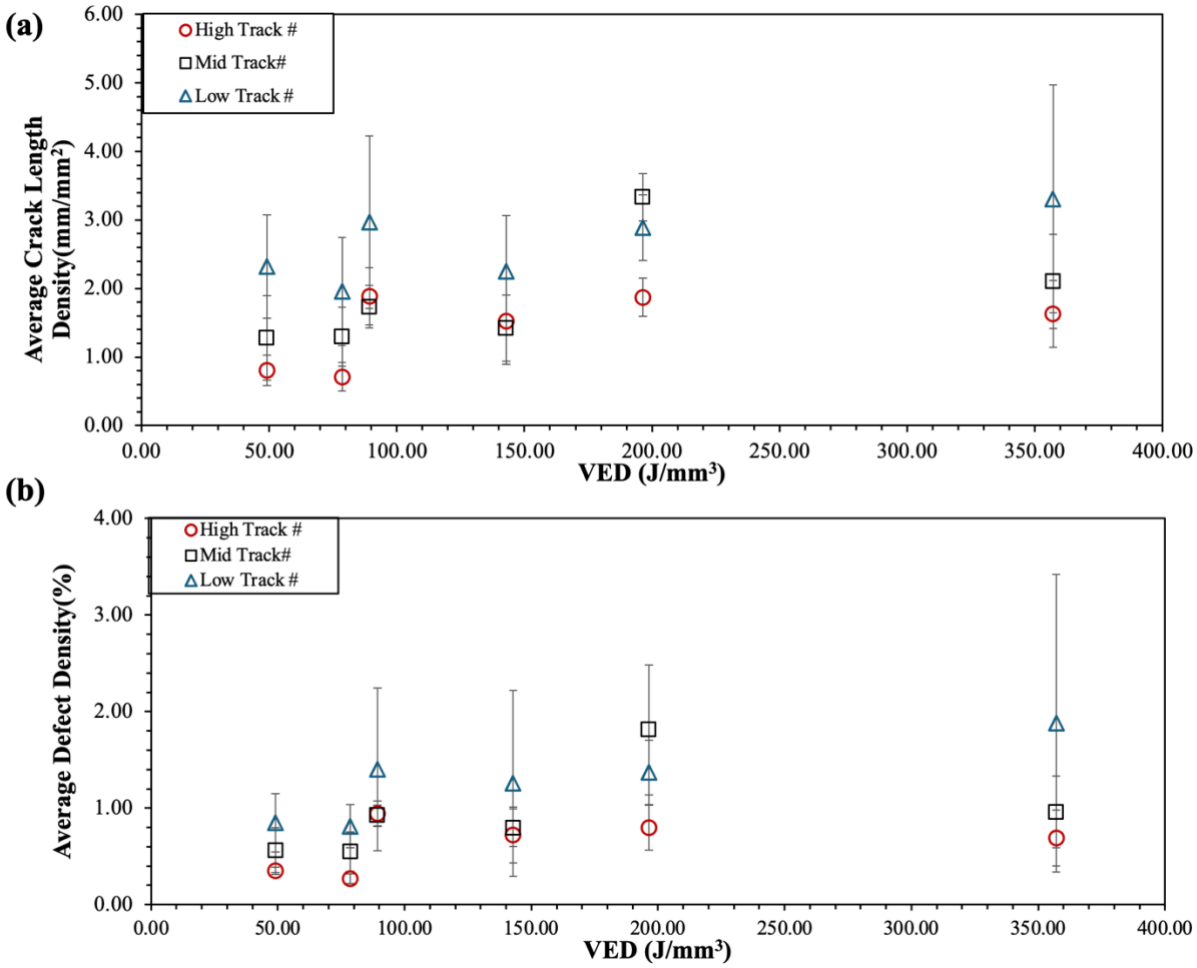


Figure 5-9. Quantitative assessment of the effect of number of tracks and line offset through VED on the (a) average crack length density and (b) average areal defect density of EBM deposited CM247LC multi-tracks

The classification of the observed porosity within the central melt body region and more prominently seen in Group A as lack of fusion porosity can be refuted. This is evidenced by the combined characteristic of its micro-size and morphology corresponding towards that of shrinkage porosity. Moreover, it can also be logically rationalized by a comparative assessment of the track overlap as dictated by line offset. This can be previously observed in Fig. 5-5 where the largest line offset still qualitatively exhibits a track overlap greater than 50%. As a more quantitative evidence, the theoretical track overlap can be evaluated by the following expression (Eqn. 5-2) [121]:

$$Overlap\ \% = \frac{w - l_o}{w} * 100 \quad (5\text{-}2)$$

where w is the melt pool width, and l_o is the line offset. For both groups, the overlap percentage results are listed in Table 5-2. For a given line offset, despite experimental Group B exhibiting a similar yet lower track overlap percentage than their Group A counterparts, the multi-track cross sections of Group B only began to show a potential weak pattern evidence of central melt body porosity along the inter-track regions at the higher line offset case of 0.16mm. In contrast, the mentioned porosity type was more consistently seen for all line offset cases in Group A despite the higher amount of overlap. Thereby, this challenges the origin of the porosity from lack of fusion due to poor melt pool overlap.

Table 5-2. Comparison of theoretical track overlap

Line Offset (μm)	Group A Track Overlap (%)	Group B Track Overlap (%)
40	93.98	92.75
100	84.96	81.89
160	75.94	71.02

A possible explanation for the absence of porosity in the central melt body of multi-tracks in Group B is described as follows. As previously discussed, a possible difference between Group A and Group B is the deposition nature of trailing versus persistent melt pool respectively. In the former case, the preceding track is already solidified while in the latter case, the preceding track persists as a liquid state during the deposition of a fresh track. In the former, the already solidified track would be at a lower temperature in contrast to the latter case since the liquid phase would indicate a higher temperature state. Evidently, during the deposition of a fresh track, the experienced temperature gradient at the inter-track region would be lower in the persistent melt pool case as opposed to the trailing melt pool condition due to the smaller temperature difference. Furthermore, as a fresh track is being deposited, while this can not only preheat the subsequent track as discussed before, it can also serve as a post heat for the previous track and lower both the local thermal gradient and cooling rate [117], [118], [122]. Furthermore, the solidification rate could also be consequently delayed. In Chapter 4, the previous modelling efforts demonstrated a low thermal gradient and cooling rate were associated with lower crack length density in the single-track condition. A similar phenomenon could be occurring for the case of the multi-track condition. The post heat process and persistent melt pool condition can sufficiently help lower the thermal gradient and cooling rate in the inter-track regions. Consequently, the thermal conditions may help sustain and enhance the liquid feeding towards the inter-dendritic zones, compensating the solidification shrinkage and the mentioned strains. Thus, shrinkage pores and cracking are prevented within the central melt body of the deposited multi-track.

Due to the lack of subsequent tracks after the final track deposition, the absence of residual heating to lower the thermal gradient and cooling rate could explain the observed surge occurrence of shrinkage pores and cracks towards the final few tracks deposited in all multi-track samples. This could possibly be compensated with a post heating contour strategy after the multi-track deposition. Meanwhile, as line offset is increased, the degree of residual post heating would be reduced [122]. As a result, this would facilitate an increase in the cooling rate and thermal gradient. Subsequently, an intensified number of shrinkage pores and cracks would be found in the inter-track melt pool boundaries of the central melt body region as witnessed for Group B at the higher line offset level of 0.16 mm.

5.3.4 Microstructure: Grain Structure

The use of EBSD analysis reveals the solidified grain maps and orientation of the EBM deposited CM247LC multi-tracks. Fig. 5-10 displays the former with the multi-track melt pool boundaries delineated by the white dashed line. Fig. 5-11 displays the IPF-Y grain orientation maps of EBM deposited CM247LC multi-tracks at varying line offset values at the constant middle track number level. For all cases, epitaxial growth phenomenon is observed whereby grains from preceding layers continually grow into the deposited multi-track region. In Fig. 5-10, for the most part, a great degree of columnar grains are observed in the multi-track region. However, some finer grains such as in the form of equiaxial grains are also present. The associated EBSD software, ESPRIT, was used for the rough measurement of grain sizes within the multi-track melt region. For all multi-track samples, the average grain sizes ranged from 56.1 μm to 96.9 um. When the Track# = 5, Group A samples showed the highest grain sizes of 94.3 um, 96.9 um, and 90.2 um with increasing line offset order, whereas Group B showed the smaller grain sizes of 64.8 um, 56.1 um, and 60.8 um. Interestingly, in comparison to the data group of track number of 5, the higher track numbers resulted in lower grain sizes for Group A, while the grain sizes were larger for Group B.

In Fig. 5-11, for all cross section of the multi-track samples, the preference for the <100> crystallographic orientation, parallel to the build direction, is observed. This texture anisotropy is as expected since nickel superalloys, such as CM247LC, are face centered cubic (FCC) metals with <100> as their most favorable orientation for grain growth [80], [84]. Interestingly, a general recurring pattern of grains with different crystallographic orientations is observed in regions corresponding to the few tracks that were deposited last. This misorientation of grains highlights HAGB and such features have been previously studied as susceptible sites for defect occurrence, such as crack initiation [17].

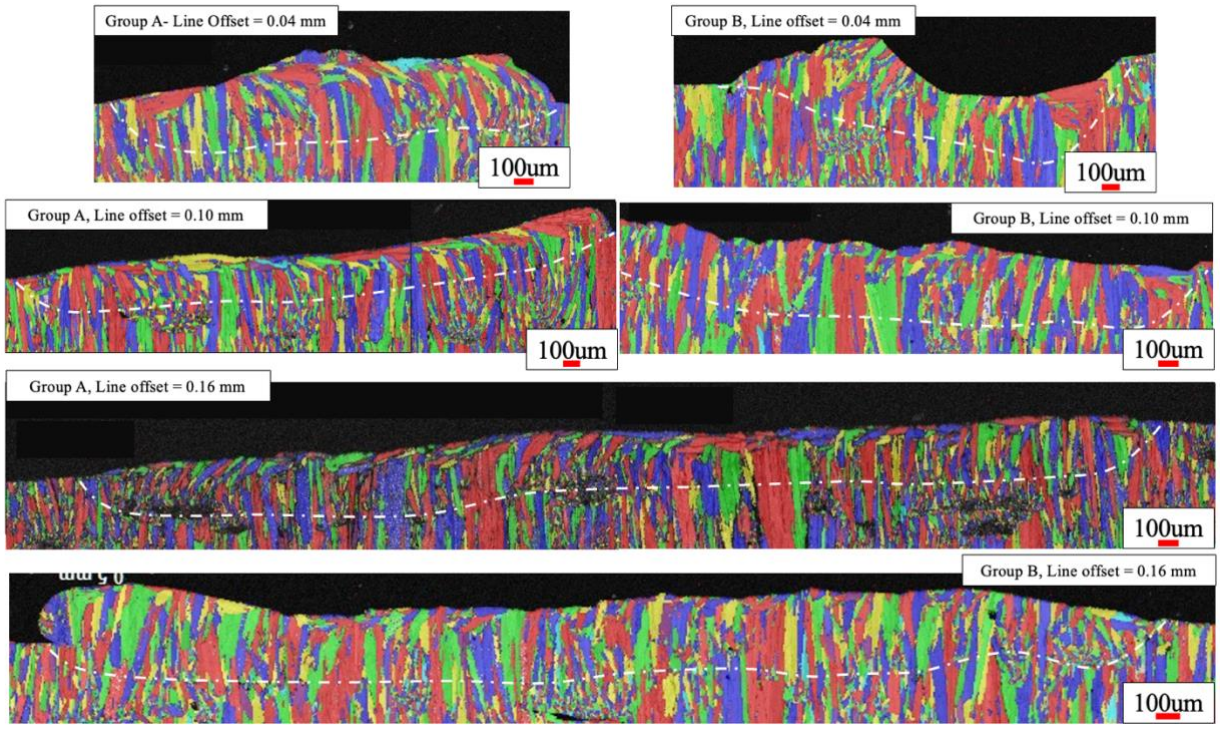


Figure 5-10. EBSD grain mapping of EBM deposited CM247LC multi-track samples at track# = 25 and with varying line offset

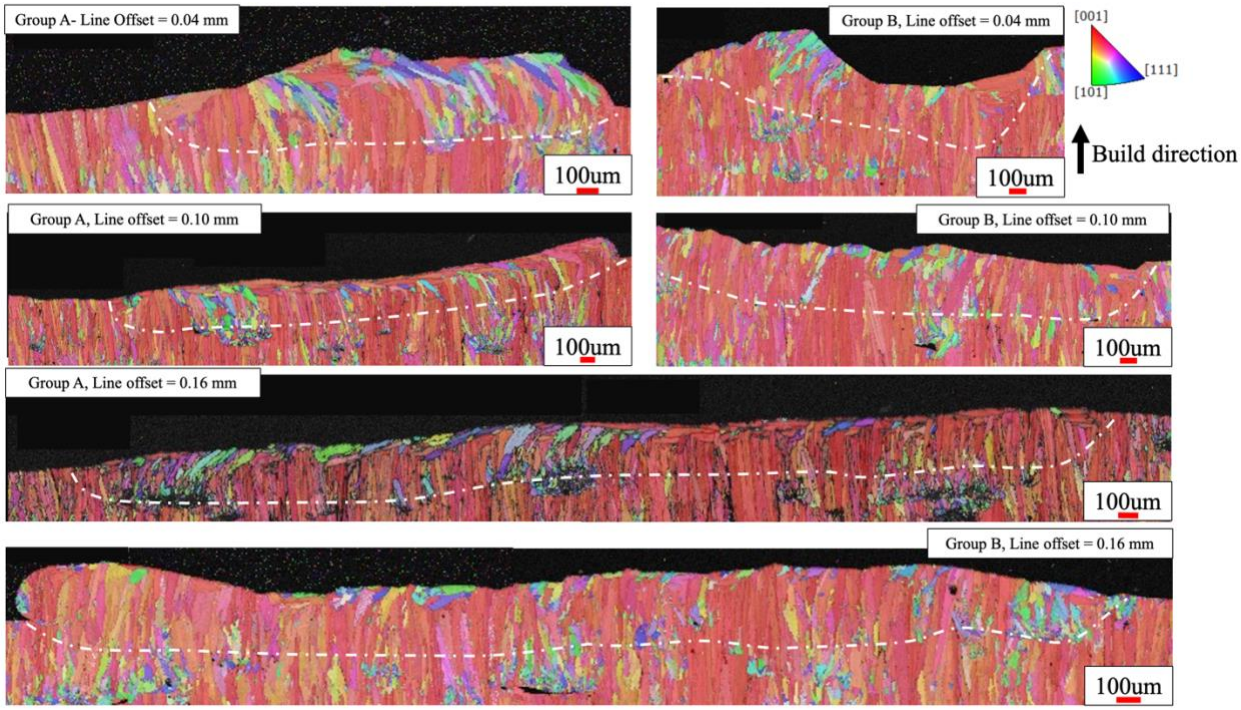


Figure 5-11. EBSD analysis of IPF-Y grain orientation map for EBM deposited CM247LC multi-track samples at a track# = 25 and varying line offset

5.4 Summary

This work builds on the previous single-track study by investigating heat accumulation effects in the lateral stacking of multiple EBM deposited CM247LC single-tracks within a single layer. The lateral arrangement of multiple tracks is controlled by line offset, with the number of tracks, with their subsequent effects on build quality, melt pool morphology, and cracking susceptibility analyzed. The results of this study are summarized as follows:

- **Surface Topography and Melt Pool Behavior**: The topographical surface and cross section of the experimental multi-track Group A and B (I = 5mA, v = 300 mm/s, and I = 11mA, v = 1200 mm/s respectively) supports the persistent and trailing melt pool nature. Group A facilitated a relatively uniform and flat surface with S_a ranging from 37-46 μm. Group B exhibited a wide variety of surface topography and was attributed possibly to the greater influence of Marangoni fluid flow. In this case, the line offset of 0.10 mm had the largest height difference in a given surface profile as evidenced by comparatively greater S_z.
- **Melt Pool Geometry**: The increase in melt pool width, depth, and aspect ratio was associated with a decrease in line offset. Significantly, the width and depth of melt pool in the multi-track condition could be observed to be lower than the single-track condition.
- **Defect Trends**: The average crack length density and areal defect density generally increased with VED (e.g. lower line offset) and lower track number. However, the individual focus on a both multi-track experimental group demonstrated a lowering of defect propensity at a line offset of 0.10 mm, possibly indicating an optimal line offset value close to 0.10mm.
- **Defect Distribution**: All cross section of multi-track samples displayed a concentration of shrinkage pores and cracks towards the last few deposited tracks, within the inter-track regions as delineated by the melt pool boundary. However, the parameter condition including a beam current of 11 mA, speed of 1200 mm/s, focus offset of 10mA, and line offset of 0.10 mm demonstrated a relatively limited or essentially defect free central melt body region. It was hypothesized that the persistent melt pool condition and post heating treatment from subsequent tracks fostered a sufficiently slow cooling rate and low thermal gradients in the inter-track regions, alleviating the strain and corresponding stress experienced.

Chapter 6. Conclusions and Future Works

6.1 Conclusions

The aim of this study was the process optimization of CM247LC parts as fabricated by electron beam melting with regards to mitigation of its crack susceptibility. In the pursuit of this endeavor, a simultaneous objective was developed to shed light on the relationship between process parameter, microstructure, and cracking behavior. This was carried out through a systematic bottom-up approach that started with the basic building block of single-tracks. Subsequently, the progression scaled to the next building block geometry which was the deposition of single layer of multi-tracks.

First, the experimental single-tracks were used to study the effect of primary process parameters on the track quality, melt pool geometry, microstructure, and crack behavior. This investigation utilized a 3^3 full factorial design of experiment with beam current, speed, and focus offset as the three defined factors. The single-tracks quality was characterized by optical microscopy and laser confocal microscopy. Meanwhile, the observations of single-track cross sections under optical microscopy, scanning electron microscopy and electron back scattered diffraction enabled the analysis of its microstructure and cracking tendencies.

Second, finite element method was used to create a thermal simulation of the CM247LC single-track deposition by EBM. The simple thermal model enabled the extraction of temperature profiles for all experimentally fabricated single-tracks in order to better grasp the spatial and temporal evolution of the thermal conditions. The thermal response of the material was described through thermal variables of thermal gradient, and cooling rate. Consequently, this fostered an apprehension of the influence by primary process parameters on the solidification conditions, and subsequently the inherent cracking behavior for a single-track.

Third, the accumulation of heat from the lateral stacking of consecutive single-tracks was studied through the EBM deposition of single layer of multi-tracks. The effect of the number of consecutive tracks and line offset on the resulting single layer quality, melt pool morphology, and crack susceptibility was studied. This was explored by leveraging on the results of the single-track study, utilizing two process parameter recipe that displayed an inherently lower propensity towards cracking. The first selected recipe was a focus offset of 10 mA, beam current of 5 mA, and speed of 300 mm/s while the second recipe was a focus offset of 10 mA, beam current of 11 mA, and speed of 1200 mm/s. In other words, the recipes were of a low current and speed extreme and a high current and speed extreme. Similar to the single-track exploration, surface confocal microscopy was used to evaluate the quality of the single layer deposited, while optical microscopy of the multi-track cross sections was used to investigate the melt pool geometry and the proneness of CM247LC towards defects such as cracking and porosity.

The findings of this study are listed as follows:

- **Single-Track Parameters**: High LED produced uniform, continuous tracks, while low LED (while having higher beam speeds), reduced track stability. Melt pool depth, width and aspect ratio increased with LED, with focus offset effectively widening pools and limiting depth. Statistical analysis showed beam speed as the dominant factor influencing melt pool geometry over interactive effects.
- **Crack Mechanisms**: Solidification and liquation cracks dominated, with severity rising with LED. A focus offset of 10mA, beam current of 5mA, and speed of 300mm/s yielded the lowest crack length density (0.25 mm/mm^2), linked to a melt pool aspect ratio of 0.32. Cracks occurred at high-angle grain boundaries, with liquation cracks transitioning to solidification cracks across melt pool boundaries, though finer equiaxed grains along boundaries reduced this propagation tendency.
- **Thermal Modeling**: A finite element thermal model predicted the melt pool width and depth with <16% error per focus offset group and ~10% overall. Higher focus offset and distance from melt pool surface lowered peak temperatures. Thermal gradients increased sharply with depth at low LED, while high LED slowed changes in cooling rates. The increase in beam speed was found to increase all solidification parameters (cooling rate and thermal gradient), while higher LED reduced them. A lower maximum cooling rate and thermal gradient demonstrated a reduced crack length density and thereby improved the susceptibility of CM247LC towards cracking.
- **Multi-track Analysis**: Low speed/low current conditions (v=300 mm/s, I=5 mA) produced stable, uniform multi-track layers (S_a = 37-46 μm), while high-speed/high-current conditions (v = 1200 mm/s, I = 11mA) showed varied topography, influenced by line offset and track number, likely due to persistent fluid states and Marangoni convection. Melt pool dimensions increased as line offset decreased. Although in some conditions, the multi-track pools were found to be narrower and shallower than single track ones.
- **Defect Trends**: Lower line offset (while having higher VED) and fewer tracks increased crack length density, and areal defect density. A line offset of 0.10 mm reduced defects in both multi-track groups, suggesting an optimal value nearby. Defects, including shrinkage pores and cracks, clustered in final tracks and inter-track regions. The recipe of focus offset = 10 mA, I = 11mA, v = 1200 mm/s, and line offset = 0.10 mm minimized defects in the central melt body.

The resulting research outcomes can empower both academic and industrial researchers with the fundamental knowledge of the interplay between print parameters, material behavior and the associated solidification conditions during the processing of CM247LC via EBM. This can help accelerate the developmental process of achieving a fully dense part. Alternatively, the basic understanding can also help

guide researchers in tailoring part deposition to achieve specific microstructures such as a highly valued single crystal microstructure. On the other hand, the preliminary examination of the different multi-track deposition nature and their potential linked benefits could inform future efforts to process other non-weldable nickel superalloys or crack susceptible materials. The acknowledgement of the different deposition nature could also be significant in the design considerations of complex part designs and the selection of appropriate print parameters. This is because the variation in the cross-sectional width of a given slice will lead to a significant non-uniform thermal conditions and Marangoni convection, ultimately impacting the single layer deposition quality and the dimensional accuracy of the final part.

6.2 Future Works

The conducted research meets its objective of process parameter optimization of CM247LC parts fabricated by EBM. Furthermore, a foundational understanding was amassed with regards to the influence of certain user-defined print parameters on the resulting printed part quality, microstructure, and its susceptibility towards cracking. Nonetheless, several aspects of this study warrant further extended study as well as provides future direction for subsequent research. A few recommendations are listed as follows:

- The multi-track study indicated a reduction in crack propensity around the line offset value of 0.10 mm. While the initial study utilized a wide range of line offset values, a second round of multi-track study could be used to further fine tune the line offset by exploring values near 0.10 mm.
- The multi-track study only involved a focus offset of 10mA. it would be interesting to observe the role of focus offset in the lateral stacking of single-tracks.
- During the multi-track study, the high current and speed extreme demonstrated features associated with a persistent melt pool character. This nature is seen to be a significant puzzle piece for the better control of the EBM deposition process and holds great promise in achieving a crack free part. As a result, it first merits a simple thermal model for confirmation of the persistent melt pool character. This thermal model can also confirm the qualitative discussion on the joint contributions of the persistent melt pool nature and post heating to lower the cooling rate, solidification rate, and thermal gradient of preceding tracks. After the confirmation, the further exploration of beam return time can enhance the control of surface quality and its relationship with crack susceptibility. This would be achieved by using a constant focus offset, a high constant current, and various beam speed values.
- All cross sections of the multi-track samples regularly displayed shrinkage pores and liquation cracks towards the end of the multi-track deposition, along the last few melt pool boundaries. A possible solution is to explore the application of a contour strategy with a defocused beam during

the post deposition. The purpose would be to lower the cooling rate and thermal gradient and thereby replicate the deposition conditions found in the central melt body of the multi-track layer.

- The use of multiple tracks in a single layer focuses on the accumulation of heat originating from the lateral stacking of individual single-tracks. The next logical progression in the study is to explore the accumulation of heat originating from vertical stacking of single layers, e.g. fabrication of cubic parts. This would involve a study on the effect of layer thickness and scan rotation on the part quality, microstructure, and crack susceptibility. In addition, another relevant vertical arrangement parameter of concern is the number of layers. This significantly fosters an understanding on part scalability along the vertical direction, away from the base build plate.

Letter of Copyright Permission

ELSEVIER LICENSE
TERMS AND CONDITIONS

Feb 26, 2025

This Agreement between Sebastian Soo ("You") and Elsevier ("Elsevier") consists of your license details and the terms and conditions provided by Elsevier and Copyright Clearance Center.

License Number	5976590126330
License date	Feb 26, 2025
Licensed Content Publisher	Elsevier
Licensed Content Publication	Additive Manufacturing
Licensed Content Title	A literature review of powder-based electron beam melting focusing on numerical simulations
Licensed Content Author	Manuela Galati,Luca Iuliano
Licensed Content Date	Jan 1, 2018
Licensed Content Volume	19
Licensed Content Issue	n/a
Licensed Content Pages	20
Start Page	1
End Page	20
Type of Use	reuse in a thesis/dissertation
Portion	figures/tables/illustrations
Number of figures/tables/illustrations	1
Format	electronic
Are you the author of this Elsevier article?	No
Will you be translating?	No
Title of new work	Process Parameter Optimization for Crack Mitigation in CM247LC processed by Electron Beam Melting
Institution name	University of Waterloo
Expected presentation date	Apr 2025

ELSEVIER LICENSE
TERMS AND CONDITIONS

Feb 26, 2025

This Agreement between Sebastian Soo ("You") and Elsevier ("Elsevier") consists of your license details and the terms and conditions provided by Elsevier and Copyright Clearance Center.

License Number	5976590979115
License date	Feb 26, 2025
Licensed Content Publisher	Elsevier
Licensed Content Publication	Additive Manufacturing
Licensed Content Title	Combining alloy and process modification for micro-crack mitigation in an additively manufactured Ni-base superalloy
Licensed Content Author	S. Griffiths,H. Ghasemi Tabasi,T. Ivas,X. Maeder,A. De Luca,K. Zweiacker,R. Wróbel,J. Jhabvala,R.E. Logé,C. Leinenbach
Licensed Content Date	Dec 1, 2020
Licensed Content Volume	36
Licensed Content Issue	n/a
Licensed Content Pages	1
Start Page	101443
End Page	0
Type of Use	reuse in a thesis/dissertation
Portion	figures/tables/illustrations
Number of figures/tables/illustrations	2
Format	electronic
Are you the author of this Elsevier article?	No
Will you be translating?	No
Title of new work	Process Parameter Optimization for Crack Mitigation in CM247LC processed by Electron Beam Melting
Institution name	University of Waterloo
Expected presentation date	Apr 2025

ELSEVIER LICENSE
TERMS AND CONDITIONS

Feb 26, 2025

This Agreement between Sebastian Soo ("You") and Elsevier ("Elsevier") consists of your license details and the terms and conditions provided by Elsevier and Copyright Clearance Center.

License Number	5976600062574
License date	Feb 26, 2025
Licensed Content Publisher	Elsevier
Licensed Content Publication	Additive Manufacturing
Licensed Content Title	Effect of process parameters on melt pool geometry and microstructure development for electron beam melting of IN718: A systematic single bead analysis study
Licensed Content Author	Xiao Ding,Yuichiro Koizumi,Daixiu Wei,Akihiko Chiba
Licensed Content Date	Mar 1, 2019
Licensed Content Volume	26
Licensed Content Issue	n/a
Licensed Content Pages	12
Start Page	215
End Page	226
Type of Use	reuse in a thesis/dissertation
Portion	figures/tables/illustrations
Number of figures/tables/illustrations	2
Format	electronic
Are you the author of this Elsevier article?	No
Will you be translating?	No
Title of new work	Process Parameter Optimization for Crack Mitigation in CM247LC processed by Electron Beam Melting
Institution name	University of Waterloo
Expected presentation date	Apr 2025

ELSEVIER LICENSE
TERMS AND CONDITIONS

Feb 26, 2025

This Agreement between Sebastian Soo ("You") and Elsevier ("Elsevier") consists of your license details and the terms and conditions provided by Elsevier and Copyright Clearance Center.

License Number	5976600490163
License date	Feb 26, 2025
Licensed Content Publisher	Elsevier
Licensed Content Publication	Materials Characterization
Licensed Content Title	Single and multiple track formation mechanism of laser powder bed fusion 316L/CuSn10 multi-material
Licensed Content Author	Jie Chen,Yongqiang Yang,Yuchao Bai,Di Wang,Cuiling Zhao,Jerry Ying Hsi Fuh
Licensed Content Date	Jan 1, 2022
Licensed Content Volume	183
Licensed Content Issue	n/a
Licensed Content Pages	1
Start Page	111654
End Page	0
Type of Use	reuse in a thesis/dissertation
Portion	figures/tables/illustrations
Number of figures/tables/illustrations	3
Format	electronic
Are you the author of this Elsevier article?	No
Will you be translating?	No
Title of new work	Process Parameter Optimization for Crack Mitigation in CM247LC processed by Electron Beam Melting
Institution name	University of Waterloo
Expected presentation date	Apr 2025

References

[1] S. L. N. Ford, “Additive Manufacturing Technology: Potential Implications for U.S. Manufacturing Competitiveness,” *J. Int. Commer. Econ.*, vol. 6, no. 1, pp. 40–74, 2014.

[2] I. Bahnini, M. Rivette, A. Rechia, A. Siadat, and A. Elmesbahi, “Additive manufacturing technology: the status, applications, and prospects | The International Journal of Advanced Manufacturing Technology,” *Int. J. Adv. Manuf. Technol.*, vol. 97, pp. 147–161, Mar. 2018, doi: https://doi.org/10.1007/s00170-018-1932-y.

[3] S. Sanchez *et al.*, “Powder Bed Fusion of nickel-based superalloys: A review,” *Int. J. Mach. Tools Manuf.*, vol. 165, p. 103729, Jun. 2021, doi: 10.1016/j.ijmachtools.2021.103729.

[4] E. Toyserkani, D. Sarker, O. O. Ibhadode, F. Liravi, P. Russo, and K. Taherkhani, *Metal Additive Manufacturing*, 1st ed. Hoboken: Wiley, 2021.

[5] L. Ladani and M. Sadeghilaridjani, “Review of Powder Bed Fusion Additive Manufacturing for Metals,” *Metals*, vol. 11, no. 9, p. 1391, Sep. 2021, doi: https://doi.org/10.3390/met11091391.

[6] P. Bajaj, F. Magni, and P. Flohr, “A Performance Upgrade of an Industrial Gas Turbine Based on Additive Manufactured Components,” in *Industrializing Additive Manufacturing*, Springer, CHam, Sep. 2020. doi: https://doi.org/10.1007/978-3-030-54334-1_35.

[7] M. Ramsperger and S. Eichler, “Electron Beam Based Additive Manufacturing of Alloy 247 for Turbine Engine Application: From Research towards Industrialization,” *Metall. Mater. Trans. A*, vol. 54, no. 5, pp. 1730–1743, May 2023, doi: 10.1007/s11661-022-06955-0.

[8] J. Wang, R. Zhu, Y. Liu, and L. Zhang, “Understanding melt pool characteristics in laser powder bed fusion: An overview of single- and multi-track melt pools for process optimization,” *Adv. Powder Mater.*, vol. 2, no. 4, p. 100137, Oct. 2023, doi: 10.1016/j.apmate.2023.100137.

[9] C. Körner, “Additive manufacturing of metallic components by selective electron beam melting — a review,” *Int. Mater. Rev.*, vol. 61, no. 5, pp. 361–377, Jul. 2016, doi: 10.1080/09506608.2016.1176289.

[10] D. Grange, J. D. Bartout, B. Macquaire, and C. Colin, “Processing a non-weldable nickel-base superalloy by Selective Laser Melting: role of the shape and size of the melt pools on solidification cracking,” *Materialia*, vol. 12, p. 100686, Aug. 2020, doi: 10.1016/j.mtla.2020.100686.

[11] C. Palanisamy, R. Raman, and P. A. Olubambi, “Microstructural Characteristics, Hardness and Tribological Behavior of Additive Manufactured CM247LC Nickel Super Alloy,” presented at the The International Conference on Applied Research and Engineering, Cape Town, South Africa, Mar. 2024, pp. 3–14. doi: 10.4028/p-yKGU2z.

[12] M. M. Attallah, R. Jennings, X. Wang, and L. N. Carter, “Additive manufacturing of Ni-based superalloys: The outstanding issues,” *MRS Bull.*, vol. 41, no. 10, pp. 758–764, Oct. 2016, doi: 10.1557/mrs.2016.211.

[13] E. Chauvet *et al.*, “Hot cracking mechanism affecting a non-weldable Ni-based superalloy produced by selective electron Beam Melting,” *Acta Mater.*, vol. 142, pp. 82–94, Jan. 2018, doi: 10.1016/j.actamat.2017.09.047.

[14] O. Adegoke, J. Andersson, H. Brodin, and R. Pederson, “Influence of Laser Powder Bed Fusion Process Parameters on Voids, Cracks, and Microhardness of Nickel-Based Superalloy Alloy 247LC,” *Materials*, vol. 13, no. 17, Art. no. 17, Jan. 2020, doi: 10.3390/ma13173770.

[15] D. Wang, S. Li, G. Deng, Y. Liu, and M. M. Attallah, “A Melt Pool Temperature Model in Laser Powder Bed Fabricated CM247LC Ni Superalloy to Rationalize Crack Formation and Microstructural Inhomogeneities,” *Metall. Mater. Trans. A*, vol. 52, no. 12, pp. 5221–5234, Dec. 2021, doi: 10.1007/s11661-021-06457-5.

[16] A. Fardan *et al.*, “Fine-Tuning Melt Pools and Microstructures: Taming Cracks in Powder Bed Fusion – Laser Beam of a non-weldable Ni-base Superalloy,” *Materialia*, p. 102059, Mar. 2024, doi: 10.1016/j.mtla.2024.102059.

[17] L. Liu *et al.*, “Crack inhibition to enhance strength-ductility of CM247LC alloy fabricated by laser powder bed fusion,” *Mater. Sci. Eng. A*, vol. 875, p. 145114, Jun. 2023, doi: 10.1016/j.msea.2023.145114.

[18] S. Griffiths *et al.*, “Combining alloy and process modification for micro-crack mitigation in an additively manufactured Ni-base superalloy,” *Addit. Manuf.*, vol. 36, p. 101443, Dec. 2020, doi: 10.1016/j.addma.2020.101443.

[19] J. F. S. Markanday *et al.*, “The Microstructural Evolution of CM247LC Manufactured Through Laser Powder Bed Fusion,” *Metall. Mater. Trans. A*, vol. 54, no. 5, pp. 1758–1775, May 2023, doi: 10.1007/s11661-022-06939-0.

[20] E. Bassini *et al.*, “Effects of the solution and first aging treatment applied to as-built and post-HIP CM247 produced via laser powder bed fusion (LPBF),” *J. Alloys Compd.*, vol. 905, p. 164213, Jun. 2022, doi: 10.1016/j.jallcom.2022.164213.

[21] S. Catchpole-Smith, N. Aboulkhair, L. Parry, C. Tuck, I. A. Ashcroft, and A. Clare, “Fractal scan strategies for selective laser melting of ‘unweldable’ nickel superalloys,” *Addit. Manuf.*, vol. 15, pp. 113–122, May 2017, doi: 10.1016/j.addma.2017.02.002.

[22] M. Gerstgrasser, M. Cloots, J. Stirnimann, and K. Wegener, “Focus shift analysis, to manufacture dense and crack-free SLM-processed CM247LC samples,” *J. Mater. Process. Technol.*, vol. 289, p. 116948, Mar. 2021, doi: 10.1016/j.jmatprotec.2020.116948.

[23] Y. Lv *et al.*, “Cracking inhibition behavior and the strengthening effect of TiC particles on the CM247LC superalloy prepared by selective laser melting,” *Mater. Sci. Eng. A*, vol. 858, p. 144119, Nov. 2022, doi: 10.1016/j.msea.2022.144119.

[24] X. Wang, L. N. Carter, B. Pang, M. M. Attallah, and M. H. Loretto, “Microstructure and yield strength of SLM-fabricated CM247LC Ni-Superalloy,” *Acta Mater.*, vol. 128, pp. 87–95, Apr. 2017, doi: 10.1016/j.actamat.2017.02.007.

[25] V. D. Divya *et al.*, “Microstructure of selective laser melted CM247LC nickel-based superalloy and its evolution through heat treatment,” *Mater. Charact.*, vol. 114, pp. 62–74, Apr. 2016, doi: 10.1016/j.matchar.2016.02.004.

[26] P. Karimi, “Electron beam-powder bed fusion of Alloy 718:,” University West, Department of Engineering Science, Division of Subtractive and Additive Manufacturing., Trollhättan, SE, 2020. [Online]. Available: http://www.diva-portal.org/smash/record.jsf?pid=diva2%3A1499956&dswid=1384

[27] M. Galati and L. Iuliano, “A literature review of powder-based electron beam melting focusing on numerical simulations,” *Addit. Manuf.*, vol. 19, pp. 1–20, Jan. 2018, doi: 10.1016/j.addma.2017.11.001.

[28] M. Q. Zafar, C. C. Wu, H. Zhao, J. Wang, and X. Hu, “Finite element framework for electron beam melting process simulation,” *Int. J. Adv. Manuf. Technol.*, vol. 109, no. 7, pp. 2095–2112, Aug. 2020, doi: 10.1007/s00170-020-05707-x.

[29] X. Ding, Y. Koizumi, D. Wei, and A. Chiba, “Effect of process parameters on melt pool geometry and microstructure development for electron beam melting of IN718: A systematic single bead analysis study,” *Addit. Manuf.*, vol. 26, pp. 215–226, Mar. 2019, doi: 10.1016/j.addma.2018.12.018.

[30] H.-J. Lee, H.-K. Kim, H.-U. Hong, and B.-S. Lee, “Influence of the focus offset on the defects, microstructure, and mechanical properties of an Inconel 718 superalloy fabricated by electron beam additive manufacturing,” *J. Alloys Compd.*, vol. 781, pp. 842–856, Apr. 2019, doi: 10.1016/j.jallcom.2018.12.070.

[31] C. Ghibaudo, R. Wartbichler, G. Marchese, H. Clemens, D. Ugues, and S. Biamino, “Influence of focus offset on the microstructure of an intermetallic γ-TiAl based alloy produced by electron beam powder bed fusion,” *J. Manuf. Process.*, vol. 89, pp. 132–141, Mar. 2023, doi: 10.1016/j.jmapro.2023.01.061.

[32] D. H. Abdeen and B. R. Palmer, “Effect of processing parameters of electron beam melting machine on properties of Ti-6Al-4V parts,” *Rapid Prototyp. J.*, vol. 22, no. 3, pp. 609–620, Apr. 2016, doi: 10.1108/RPJ-09-2014-0105.

[33] H. Yue, Y. Chen, X. Wang, and F. Kong, “Effect of beam current on microstructure, phase, grain characteristic and mechanical properties of Ti-47Al-2Cr-2Nb alloy fabricated by selective electron beam melting,” *J. Alloys Compd.*, vol. 750, pp. 617–625, Jun. 2018, doi: 10.1016/j.jallcom.2018.03.343.

[34] X. Wang, X. Gong, and K. Chou, “Scanning Speed Effect on Mechanical Properties of Ti-6Al-4V Alloy Processed by Electron Beam Additive Manufacturing,” *Procedia Manuf.*, vol. 1, pp. 287–295, Jan. 2015, doi: 10.1016/j.promfg.2015.09.026.

[35] K. Puebla, L. E. Murr, S. M. Gaytan, E. Martinez, F. Medina, and R. B. Wicker, “Effect of Melt Scan Rate on Microstructure and Macrostructure for Electron Beam Melting of Ti-6Al-4V,” vol. 2012, May 2012, doi: 10.4236/msa.2012.35038.

[36] W. Ameen, A. Al-Ahmari, N. Ahmed, W. Alshammary, S. Salunkhe, and Hussein. M. A. Hussein, “Investigation the effect of electron beam melting parameters on overhang structure deformation,” *Mater. Technol.*, vol. 37, no. 10, pp. 1586–1593, Aug. 2022, doi: 10.1080/10667857.2021.1994174.

[37] J. C. Diaz *et al.*, “Effect of Layer Thickness and Heat Treatment on Microstructure and Mechanical Properties of Alloy 625 Manufactured by Electron Beam Powder Bed Fusion,” *Materials*, vol. 15, no. 21, Art. no. 21, Jan. 2022, doi: 10.3390/ma15217767.

[38] H. E. Helmer, C. Körner, and R. F. Singer, “Additive manufacturing of nickel-based superalloy Inconel 718 by selective electron beam melting: Processing window and microstructure,” *J. Mater. Res.*, vol. 29, no. 17, pp. 1987–1996, Sep. 2014, doi: 10.1557/jmr.2014.192.

[39] A. T. Silvestri, S. Foglia, R. Borrelli, S. Franchitti, C. Pirozzi, and A. Astarita, “Electron beam melting of Ti6Al4V: Role of the process parameters under the same energy density,” *J. Manuf. Process.*, vol. 60, pp. 162–179, Dec. 2020, doi: 10.1016/j.jmapro.2020.10.065.

[40] T. Scharowsky, A. Bauereiß, and C. Körner, “Influence of the hatching strategy on consolidation during selective electron beam melting of Ti-6Al-4V,” *Int. J. Adv. Manuf. Technol.*, vol. 92, no. 5, pp. 2809–2818, Sep. 2017, doi: 10.1007/s00170-017-0375-1.

[41] H. Helmer, A. Bauereiß, R. F. Singer, and C. Körner, “Grain structure evolution in Inconel 718 during selective electron beam melting,” *Mater. Sci. Eng. A*, vol. 668, pp. 180–187, Jun. 2016, doi: 10.1016/j.msea.2016.05.046.

[42] X. Zhao, Y. Wei, R. Mansour, S. Dadbakhsh, and A. Rashid, “Effect of Scanning Strategy on Thermal Stresses and Strains during Electron Beam Melting of Inconel 625: Experiment and Simulation,” *Materials*, vol. 16, no. 1, p. 443, Mar. 2023, doi: https://doi.org/10.3390/ma16010443.

[43] T. Machirori, F. Q. Liu, Q. Y. Yin, and H. L. Wei, “Spatiotemporal variations of residual stresses during multi-track and multi-layer deposition for laser powder bed fusion of Ti-6Al-4V,” *Comput. Mater. Sci.*, vol. 195, p. 110462, Jul. 2021, doi: 10.1016/j.commatsci.2021.110462.

[44] R. Raghu, P. Chandramohan, D. P. Kumar, and A. Singh, “Structural Characterization and Strength Assessment of Laser Powder Bed Fusion Manufactured CM247LC Nickel Based Super Alloy,” *J. Mater. Eng. Perform.*, vol. 32, no. 24, pp. 11310–11325, Dec. 2023, doi: 10.1007/s11665-023-08550-9.

[45] L. E. Murr *et al.*, “Microstructures of Rene 142 nickel-based superalloy fabricated by electron beam melting,” *Acta Mater.*, vol. 61, no. 11, pp. 4289–4296, Jun. 2013, doi: 10.1016/j.actamat.2013.04.002.

[46] F. Schulz, K. Lindgren, J. Xu, and E. Hryha, “Gamma prime formation in nickel-based superalloy IN738LC manufactured by laser powder bed fusion,” *Mater. Today Commun.*, vol. 38, p. 107905, Mar. 2024, doi: 10.1016/j.mtcomm.2023.107905.

[47] M. Xia, D. Gu, G. Yu, D. Dai, H. Chen, and Q. Shi, “Influence of hatch spacing on heat and mass transfer, thermodynamics and laser processability during additive manufacturing of Inconel 718 alloy,” *Int. J. Mach. Tools Manuf.*, vol. 109, pp. 147–157, Oct. 2016, doi: https://doi.org/10.1016/j.ijmachtools.2016.07.010.

[48] K. Harris, “MAR M 247 DERIVATIONS - CM 247 LC DS ALLOY CMSX SINGLE CRYSTAL ALLOYS PROPERTIES & PERFORMANCE”.

[49] R. Muñoz-Moreno *et al.*, “Effect of heat treatment on the microstructure, texture and elastic anisotropy of the nickel-based superalloy CM247LC processed by selective laser melting,” *Mater. Sci. Eng. A*, vol. 674, pp. 529–539, 2016, doi: https://doi.org/10.1016/j.msea.2016.06.075.

[50] L. Liu *et al.*, “Crack inhibition and mechanical property enhancement of a CM247LC alloy fabricated by laser powder bed fusion through remelting strategy,” *Mater. Charact.*, vol. 214, p. 114073, Aug. 2024, doi: 10.1016/j.matchar.2024.114073.

[51] Z. Fu and C. Körner, “Actual state-of-the-art of electron beam powder bed fusion,” *Eur. J. Mater.*, vol. 2, no. 1, pp. 54–116, Dec. 2022, doi: 10.1080/26889277.2022.2040342.

[52] D. Deng, R. L. Peng, H. Söderberg, and J. Moverare, “On the formation of microstructural gradients in a nickel-base superalloy during electron beam melting,” *Mater. Des.*, vol. 160, pp. 251–261, Dec. 2018, doi: 10.1016/j.matdes.2018.09.006.

[53] W. Yan *et al.*, “Multi-physics modeling of single/multiple-track defect mechanisms in electron beam selective melting,” *Acta Mater.*, vol. 134, pp. 324–333, Aug. 2017, doi: 10.1016/j.actamat.2017.05.061.

[54] P. Karimi, E. Sadeghi, J. Ålgårdh, and J. Andersson, “EBM-manufactured single tracks of Alloy 718: Influence of energy input and focus offset on geometrical and microstructural characteristics,” *Mater. Charact.*, vol. 148, pp. 88–99, Feb. 2019, doi: 10.1016/j.matchar.2018.11.033.

[55]Z. Hu, B. Nagarajan, X. Song, R. Huang, W. Zhai, and J. Wei, "Formation of SS316L Single Tracks in Micro Selective Laser Melting: Surface, Geometry, and Defects," *Adv. Mater. Sci. Eng.*, vol. 2019, no. 1, p. 9451406, 2019, doi: https://doi.org/10.1155/2019/9451406.

[56]J. Chen *et al.*, "Cracking mechanisms in additively manufactured pure tungsten from printing single tracks, thin walls and cubes," *Mater. Des.*, vol. 234, p. 112363, 2023, doi: https://doi.org/10.1016/j.matdes.2023.112363.

[57]J. A. Koepf, D. Soldner, M. Ramsperger, J. Mergheim, M. Markl, and C. Körner, "Numerical microstructure prediction by a coupled finite element cellular automaton model for selective electron beam melting," *Comput. Mater. Sci.*, vol. 162, pp. 148–155, May 2019, doi: 10.1016/j.commatsci.2019.03.004.

[58]D. Riedlbauer, T. Scharowsky, R. F. Singer, P. Steinmann, C. Körner, and J. Mergheim, "Macroscopic simulation and experimental measurement of melt pool characteristics in selective electron beam melting of Ti-6Al-4V," *Int. J. Adv. Manuf. Technol.*, vol. 88, no. 5, pp. 1309–1317, Feb. 2017, doi: 10.1007/s00170-016-8819-6.

[59]N. Shen and K. Chou, "Thermal Modeling of Electron Beam Additive Manufacturing Process: Powder Sintering Effects," doi: 10.1115/MSEC2012-7253.

[60]B. Cheng, S. Price, J. Lydon, K. Cooper, and K. Chou, "On Process Temperature in Powder-Bed Electron Beam Additive Manufacturing: Model Development and Validation," *J. Manuf. Sci. Eng.*, vol. 136, no. 061018, Oct. 2014, doi: 10.1115/1.4028484.

[61]J. Romano, L. Ladani, J. Razmi, and M. Sadowski, "Temperature distribution and melt geometry in laser and electron-beam melting processes – A comparison among common materials," *Addit. Manuf.*, vol. 8, pp. 1–11, Oct. 2015, doi: 10.1016/j.addma.2015.07.003.

[62]N. An, G. Yang, K. Yang, J. Wang, M. Li, and J. Zhou, "Implementation of Abaqus user subroutines and plugin for thermal analysis of powder-bed electron-beam-melting additive manufacturing process," *Mater. Today Commun.*, vol. 27, p. 102307, Jun. 2021, doi: https://doi.org/10.1016/j.mtcomm.2021.102307.

[63]T.-N. Le, Y.-L. Lo, and H.-C. Tran, "Multi-scale modeling of selective electron beam melting of Ti6Al4V titanium alloy," *Int. J. Adv. Manuf. Technol.*, vol. 105, no. 1, pp. 545–563, Nov. 2019, doi: 10.1007/s00170-019-04188-x.

[64]W. Yan, J. Smith, W. Ge, F. Lin, and W. K. Liu, "Multiscale modeling of electron beam and substrate interaction: a new heat source model," *Comput. Mech.*, vol. 56, no. 2, pp. 265–276, Aug. 2015, doi: 10.1007/s00466-015-1170-1.

[65] M. Galati, L. Iuliano, A. Salmi, and E. Atzeni, “Modelling energy source and powder properties for the development of a thermal FE model of the EBM additive manufacturing process,” *Addit. Manuf.*, vol. 14, pp. 49–59, Mar. 2017, doi: 10.1016/j.addma.2017.01.001.

[66] P. W. Liu *et al.*, “Investigation on evolution mechanisms of site-specific grain structures during metal additive manufacturing,” *J. Mater. Process. Technol.*, vol. 257, pp. 191–202, Jul. 2018, doi: 10.1016/j.jmatprotec.2018.02.042.

[67] J. Chen, Y. Yang, Y. Bai, D. Wang, C. Zhao, and J. Ying Hsi Fuh, “Single and multiple track formation mechanism of laser powder bed fusion 316L/CuSn10 multi-material,” *Mater. Charact.*, vol. 183, p. 111654, Jan. 2022, doi: 10.1016/j.matchar.2021.111654.

[68] C. Wu, H. Zhao, H. Li, and F. Lin, “Track irregularity behaviours in electron beam selective melting,” *Sci. Technol. Weld. Join.*, vol. 28, no. 1, pp. 27–37, Jan. 2023, doi: 10.1080/13621718.2022.2111502.

[69] W. Zhang, W. Hou, L. Deike, and C. Arnold, “Understanding the Rayleigh instability in humping phenomenon during laser powder bed fusion process,” *Int. J. Extreme Manuf.*, vol. 4, no. 1, p. 015201, Jan. 2022, doi: 10.1088/2631-7990/ac466d.

[70] W. Ge, S. Han, Y. Fang, J. Cheon, and S. J. Na, “Mechanism of surface morphology in electron beam melting of Ti6Al4V based on computational flow patterns,” *Appl. Surf. Sci.*, vol. 419, pp. 150–158, Oct. 2017, doi: 10.1016/j.apsusc.2017.05.033.

[71] C. Wu, H. Zhao, Y. Li, P. Xie, and F. Lin, “Surface morphologies of intra-layer printing process in electron beam powder bed fusion: A high-fidelity modeling study with experimental validation,” *Addit. Manuf.*, vol. 72, p. 103614, Jun. 2023, doi: 10.1016/j.addma.2023.103614.

[72] P. Dong, Z. Li, D. Li, Y. Yu, and W. Zhang, “Track trajectory, molten pool and defect characterization in NiTi single-track selective laser melting (SLM) experiments,” *J. Mater. Res. Technol.*, vol. 33, pp. 5210–5222, Nov. 2024, doi: 10.1016/j.jmrt.2024.10.112.

[73] H. Wang and Y. Zou, “Microscale interaction between laser and metal powder in powder-bed additive manufacturing: Conduction mode versus keyhole mode,” *Int. J. Heat Mass Transf.*, vol. 142, p. 118473, Oct. 2019, doi: 10.1016/j.ijheatmasstransfer.2019.118473.

[74] X. Xiao, Y. Fu, X. Ye, M. Cheng, and L. Song, “Analysis of heat transfer and melt flow in conduction, transition, and keyhole modes for CW laser welding,” *Infrared Phys. Technol.*, vol. 120, p. 103996, Jan. 2022, doi: https://doi.org/10.1016/j.infrared.2021.103996.

[75] M. C. Brennan, J. S. Keist, and T. A. Palmer, “Defects in Metal Additive Manufacturing Processes,” *J. Mater. Eng. Perform.*, vol. 30, no. 7, pp. 4808–4818, Jul. 2021, doi: 10.1007/s11665-021-05919-6.

[76] S. Shrestha and K. Chou, “Formation of keyhole and lack of fusion pores during the laser powder bed fusion process,” *Manuf. Lett.*, vol. 32, pp. 19–23, Apr. 2022, doi: 10.1016/j.mfglet.2022.01.005.

[77] W. Frieden Templeton, S. Hinnebusch, S. T. Strayer, A. C. To, P. C. Pistorius, and S. P. Narra, "A mechanistic explanation of shrinkage porosity in laser powder bed fusion additive manufacturing," *Acta Mater.*, vol. 266, p. 119632, Mar. 2024, doi: 10.1016/j.actamat.2023.119632.

[78] O. Mehrabi, S. M. H. Seyedkashi, and M. Moradi, "Functionally Graded Additive Manufacturing of Thin-Walled 316L Stainless Steel-Inconel 625 by Direct Laser Metal Deposition Process: Characterization and Evaluation," *Metals*, vol. 13, no. 6, p. 1108, Apr. 2023, doi: https://doi.org/10.3390/met13061108.

[79] N. Coniglio and C. E. Cross, "Initiation and growth mechanisms for weld solidification cracking," *Int. Mater. Rev.*, vol. 58, no. 7, Jan. 2013, doi: https://doi.org/10.1179/1743280413Y.0000000020.

[80] J. N. DuPont, J. C. Lippold, and S. D. Kiser, *Welding Metallurgy and Weldability of Nickel-Base Alloys*. John Wiley & Sons, 2011.

[81] A. Wall and M. J. Benoit, "A review of existing solidification crack tests and analysis of their transferability to additive manufacturing," *J. Mater. Process. Technol.*, vol. 320, Nov. 2023, doi: https://doi.org/10.1016/j.jmatprotec.2023.118090.

[82] S. Singh, J. Andersson, and K. Kadoi, "Microstructure gradient formation in electron-beam melting powder-bed fusion of a gamma-prime Ni-based superalloy," *Mater. Charact.*, vol. 205, p. 113370, Nov. 2023, doi: 10.1016/j.matchar.2023.113370.

[83] P. Karimi *et al.*, "Tailored grain morphology via a unique melting strategy in electron beam-powder bed fusion," *Mater. Sci. Eng. A*, vol. 824, p. 141820, Sep. 2021, doi: https://doi.org/10.1016/j.msea.2021.141820.

[84] S. Kou, *Welding Metallurgy*, 1st ed. Haboken, New Jersey: John Wiley & Sons, Ltd, 2002. doi: 10.1002/0471434027.

[85] R. W. Fonda and D. J. Rowenhorst, "Crystallographic Variability in Additive Manufacturing," *IOP Conf. Ser. Mater. Sci. Eng.*, vol. 1249, no. 1, p. 012007, Jul. 2022, doi: 10.1088/1757-899X/1249/1/012007.

[86] D. M. Stefanescu and R. Ruxanda, "Fundamentals of Solidification," Dec. 2004, doi: 10.31399/asm.hb.v09.a0003724.

[87] A. R. A. Dezfoli, W.-S. Hwang, W.-C. Huang, and T.-W. Tsai, "Determination and controlling of grain structure of metals after laser incidence: Theoretical approach," *Sci. Rep.*, vol. 7, p. 41527, Jan. 2017, doi: https://doi.org/10.1038/srep41527 Share this article.

[88] M. Grasso and B. M. Colosimo, "A review of the current state-of-the-art on in situ monitoring in electron beam powder bed fusion," *Prog. Addit. Manuf.*, vol. 9, no. 5, pp. 1449–1466, Oct. 2024, doi: 10.1007/s40964-024-00576-2.

[89] B. Schoinochoritis, D. Chantzis, and K. Salonitis, "Simulation of metallic powder bed additive manufacturing processes with the finite element method: A critical review," *Proc. Inst. Mech. Eng. Part B J. Eng. Manuf.*, vol. 231, no. 1, pp. 96–117, Jan. 2017, doi: 10.1177/0954405414567522.

[90] M. F. Zäh and S. Lutzmann, "Modelling and simulation of electron beam melting," *Prod. Eng. Res. Dev.*, vol. 4, pp. 15–23, Feb. 2010, doi: https://doi.org/10.1007/s11740-009-0197-6.

[91] N. Raghavan *et al.*, "Numerical modeling of heat-transfer and the influence of process parameters on tailoring the grain morphology of IN718 in electron beam additive manufacturing," *Acta Mater.*, vol. 112, pp. 303–314, Jun. 2016, doi: 10.1016/j.actamat.2016.03.063.

[92] J. Goldak, A. Chakravarti, and M. Bibby, "A new finite element model for welding heat sources | Metallurgical and Materials Transactions B," *Springer Nat.*, vol. 15, pp. 299–305, Jun. 1984.

[93] P. Liu, X. Cui, J. Deng, S. Li, Z. Li, and L. Chen, "Investigation of thermal responses during metallic additive manufacturing using a 'Tri-Prism' finite element method," *Int. J. Therm. Sci.*, vol. 136, pp. 217–229, Feb. 2019, doi: https://doi.org/10.1016/j.ijthermalsci.2018.10.022.

[94] G. Fu, J. Gu, M. I. Lourenco, M. Duan, and S. F. Estefen, "Parameter determination of double-ellipsoidal heat source model and its application in the multi-pass welding process," *Ships Offshore Struct.*, vol. 10, no. 2, pp. 204–217, Mar. 2015, doi: 10.1080/17445302.2014.937059.

[95] M. Gerstgrasser, R. Jakob, K. S. Pandya, J. Stirnimann, and K. Wegener, "CA single track microstructure simulation of nickel base alloy CM247LC and stainless steel S316L, including experimental validation of S316L," *Mater. Des.*, vol. 199, p. 109395, Feb. 2021, doi: 10.1016/j.matdes.2020.109395.

[96] K. Mukai, Z. Li, and L. Fang, "Measurement of the Densities of Nickel-Based Ternary, Quaternary and Commercial Alloys," *Mater. Trans.*, vol. 45, no. 10, pp. 2987–2993, 2004, doi: 10.2320/matertrans.45.2987.

[97] Z. Zhang *et al.*, "3-Dimensional heat transfer modeling for laser powder-bed fusion additive manufacturing with volumetric heat sources based on varied thermal conductivity and absorptivity," *Opt. Laser Technol.*, vol. 109, pp. 297–312, Jan. 2019, doi: 10.1016/j.optlastec.2018.08.012.

[98] P. Foteinopoulos, A. Papacharalmpopoulos, and P. Stavropoulos, "On thermal modeling of Additive Manufacturing processes," *CIRP J. Manuf. Sci. Technol.*, vol. 20, pp. 66–83, Jan. 2018, doi: https://doi.org/10.1016/j.cirpj.2017.09.007.

[99] S. I. Shahabad *et al.*, "Heat source model calibration for thermal analysis of laser powder-bed fusion," *Int. J. Adv. Manuf. Technol.*, vol. 106, no. 7, pp. 3367–3379, Feb. 2020, doi: 10.1007/s00170-019-04908-3.

[100]H. C. Basoalto *et al.*, “A computational study on the three-dimensional printability of precipitate-strengthened nickel-based superalloys,” *Proc. Math. Phys. Eng. Sci.*, vol. 474, no. 2220, p. 20180295, Dec. 2018, doi: 10.1098/rspa.2018.0295.

[101]S. SUMIN SIH and J. W. BARLOW, “The Prediction of the Emissivity and Thermal Conductivity of Powder Beds,” *Part. Sci. Technol.*, vol. 22, no. 3, pp. 291–304, Jul. 2004, doi: 10.1080/02726350490501682a.

[102]F. Shen, Y. Wang, J. Yao, and J.-L. Yang, “Finite element simulation of thermal distribution in direct metal laser multi-track sintering,” *J. Sichuan Univ. Eng. Sci. Ed.*, vol. 37, no. 1, pp. 47–51, 2005.

[103]M. A. L. Phan, O. Dew, and I. Todd, “Predictive process diagram for parameters selection in laser powder bed fusion to achieve high-density and low-cracking built parts,” *Addit. Manuf.*, vol. 85, p. 104145, Apr. 2024, doi: 10.1016/j.addma.2024.104145.

[104]S. S. Sih and J. W. Barlow, “Emissivity of Powder Beds”.

[105]M. Jamshidinia, F. Kong, and R. Kovacevic, “The Coupled CFD-FEM Model of Electron Beam Melting® (EBM),” Nov. 2013. doi: 10.13140/2.1.4136.2245.

[106]A. Chouhan, L. Mädler, and N. Ellendt, “Modeling of rapid solidification in Laser Powder Bed Fusion processes,” *Comput. Mater. Sci.*, vol. 238, p. 112918, Apr. 2024, doi: https://doi.org/10.1016/j.commatsci.2024.112918.

[107]S. Guan *et al.*, “Revealing thermal behavior, cracking behavior, phase and microstructure formation of a ternary equiatomic alloy additively manufactured using directed energy deposition,” *Addit. Manuf.*, vol. 78, p. 103897, Sep. 2023, doi: https://doi.org/10.1016/j.addma.2023.103897.

[108]E. Mirkoohi, J. R. Dobbs, and S. Y. Liang, “Analytical mechanics modeling of in-process thermal stress distribution in metal additive manufacturing,” *J. Manuf. Process.*, vol. 58, pp. 41–54, Oct. 2020, doi: https://doi.org/10.1016/j.jmapro.2020.08.009.

[109]Y. Chen, K. Zhang, J. Huang, S. R. E. Hosseini, and Z. Li, “Characterization of heat affected zone liquation cracking in laser additive manufacturing of Inconel 718,” *Mater. Des.*, vol. 90, pp. 586–594, Jan. 2016, doi: https://doi.org/10.1016/j.matdes.2015.10.155.

[110]C. Barr, S. Da Sun, M. Easton, N. Orchowski, N. Matthews, and M. Brandt, “Influence of macrosegregation on solidification cracking in laser clad ultra-high strength steels,” *Surf. Coat. Technol.*, vol. 340, pp. 126–136, Apr. 2018, doi: 10.1016/j.surfcoat.2018.02.052.

[111]E. Chauvet, C. Tassin, J.-J. Blandin, R. Dendievel, and G. Martin, “Producing Ni-base superalloys single crystal by selective electron beam melting,” *Scr. Mater.*, vol. 152, pp. 15–19, Jul. 2018, doi: 10.1016/j.scriptamat.2018.03.041.

[112]H.-Y. Yue, H. Peng, Y.-J. Su, X.-P. Wang, and Y.-Y. Chen, “Microstructure and high-temperature tensile property of TiAl alloy produced by selective electron beam melting,” *Rare Met.*, vol. 40, pp. 3635–3644, Mar. 2021, doi: https://doi.org/10.1007/s12598-020-01683-z.

[113]H. Gong, K. Rafi, H. Gu, T. Starr, and B. Stucker, “Analysis of defect generation in Ti–6Al–4V parts made using powder bed fusion additive manufacturing processes,” *Addit. Manuf.*, vol. 1–4, pp. 87–98, Oct. 2014, doi: 10.1016/j.addma.2014.08.002.

[114]Z. Hu, X. Nie, Y. Qi, H. Zhang, and H. Zhu, “Cracking criterion for high strength Al–Cu alloys fabricated by selective laser melting,” *Addit. Manuf.*, vol. 37, p. 101709, Jan. 2021, doi: https://doi.org/10.1016/j.addma.2020.101709.

[115]M. Xia, D. Gu, G. Yu, D. Dai, H. Chen, and Q. Shi, “Influence of hatch spacing on heat and mass transfer, thermodynamics and laser processability during additive manufacturing of Inconel 718 alloy,” *Int. J. Mach. Tools Manuf.*, vol. 109, pp. 147–157, Oct. 2016, doi: 10.1016/j.ijmachtools.2016.07.010.

[116]C. Breuning, J. Pistor, M. Markl, and C. Körner, “Basic Mechanism of Surface Topography Evolution in Electron Beam Based Additive Manufacturing,” *Materials*, vol. 15, no. 14, Art. no. 14, Jan. 2022, doi: 10.3390/ma15144754.

[117]S. Liu, J. Zhu, H. Zhu, J. Yin, C. Chen, and X. Zeng, “Effect of the track length and track number on the evolution of the molten pool characteristics of SLMed Al alloy: Numerical and experimental study,” *Opt. Laser Technol.*, vol. 123, p. 105924, Mar. 2020, doi: 10.1016/j.optlastec.2019.105924.

[118]S. Waqar, Q. Sun, J. Liu, K. Guo, and J. Sun, “Numerical investigation of thermal behavior and melt pool morphology in multi-track multi-layer selective laser melting of the 316L steel,” *Int. J. Adv. Manuf. Technol.*, vol. 112, no. 3, pp. 879–895, Jan. 2021, doi: 10.1007/s00170-020-06360-0.

[119]N. E. Gorji *et al.*, “A new method for assessing the recyclability of powders within Powder Bed Fusion process,” *Mater. Charact.*, vol. 161, p. 110167, Mar. 2020, doi: 10.1016/j.matchar.2020.110167.

[120]K. L. Terrassa, J. C. Haley, B. E. MacDonald, and J. M. Schoenung, “Reuse of powder feedstock for directed energy deposition,” *Powder Technol.*, vol. 338, pp. 819–829, Oct. 2018, doi: 10.1016/j.powtec.2018.07.065.

[121]W. Di, Y. Yongqiang, S. Xubin, and C. Yonghua, “Study on energy input and its influences on single-track,multi-track, and multi-layer in SLM,” *Int. J. Adv. Manuf. Technol.*, vol. 58, no. 9, pp. 1189–1199, Feb. 2012, doi: 10.1007/s00170-011-3443-y.

[122]M. Higashi and K. Yoshimi, “Electron beam surface melting of MoSiBTiC alloys: Effect of preheating on cracking behavior and microstructure evolution,” *Mater. Des.*, vol. 209, p. 110010, Nov. 2021, doi: 10.1016/j.matdes.2021.110010.